



**OPTIMAL CONTROL PROBLEMS FOR SAFE AND EFFICIENT LANE
CHANGES OF SELF-DRIVING VEHICLES**

ARDM HASEEB MOHAMMED ALI

SEPTEMBER 2017

OPTIMAL CONTROL PROBLEMS FOR SAFE AND EFFICIENT LANE
CHANGES OF SELF-DRIVING VEHICLES

A THESIS SUBMITTED TO
THE GRADUATE SCHOOL OF NATURAL AND APPLIED
SCIENCES OF
ÇANKAYA UNIVERSITY

BY
ARDM HASEEB MOHAMMED ALI

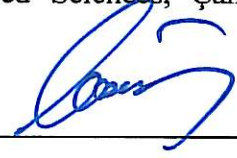
IN PARTIAL FULFILLMENT OF THE REQUIREMENTS FOR THE
DEGREE OF
DOCTOR OF PHILOSOPHY
IN
THE DEPARTMENT OF
ELECTRONIC AND COMMUNICATION ENGINEERING

SEPTEMBER 2017

Title of the Thesis: Optimal Control Problems for Safe and Efficient Lane Changes of Self-Driving Vehicles

Submitted by **Ardm Haseeb Mohammed Ali**

Approval of the Graduate School of Natural and Applied Sciences, Çankaya University.



Prof. Dr. Can ÇOĞUN
Director

I certify that this thesis satisfies all the requirements as a thesis for the degree of Doctor of Philosophy.



Prof. Dr. Sitki Kemal IDER
Head of Department

This is to certify that we have read this thesis and that in our opinion it is fully adequate, in scope and quality, as a thesis for the degree of Doctor of Philosophy.



Assoc. Prof. Dr. Klaus Werner SCHMIDT
Supervisor

Examination Date: 14.09.2017

Examining Committee Members

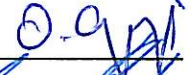
Assoc. Prof. Dr. Klaus Werner SCHMIDT (Çankaya Univ.)

Prof. Dr. Mehmet Kemal LEBLEBİCİOĞLU (METU)

Assoc. Prof. Dr. Orhan GAZİ (Çankaya Univ.)

Assist. Prof. Dr. Emre ÖZKAN (METU)

Assoc. Prof. Dr. Hüsnü Deniz BAŞDEMİR (Çankaya Univ.)



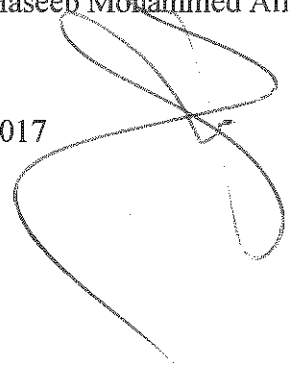
STATEMENT OF NON-PLAGIARISM PAGE

I hereby declare that all information in this document has been obtained and presented in accordance with academic rules and ethical conduct. I also declare that, as required by these rules and conduct, I have fully cited and referenced all material and results that are not original to this work.

Name, Last Name : Ardm Haseeb Mohammed Ali

Signature :

Date : 14.09.2017

A handwritten signature in black ink, consisting of several loops and a long horizontal stroke at the bottom, positioned to the right of the signature label.

ABSTRACT

OPTIMAL CONTROL PROBLEMS FOR SAFE AND EFFICIENT LANE CHANGES OF SELF-DRIVING VEHICLES

ALI, Ardm Haseeb Mohammed

Ph.D., Department of Electronic and Communication Engineering

Supervisor: Assoc. Prof. Dr. Klaus Werner SCHMIDT

September 2017, 148 pages

Intelligent Transportation Systems (ITS) aim at increasing the traffic throughput and safety, reducing the total travel time and traffic congestion using novel achievements of communication and control technologies. In particular, the development of self-driving vehicles is an important application of ITS that is expected to show a considerable impact in the near future.

When implementing self-driving vehicles, the realization of lane changes is a necessary task. Accordingly, this thesis focuses on the computation of longitudinal and lateral maneuvers during lane changes. The thesis first determines several models for the longitudinal and lateral vehicle dynamics that are deemed suitable for representing normal driving situations. In addition, a novel method for decoupling the longitudinal and lateral motion is proposed. Based on the vehicle models, an optimal control problem for lane change maneuvers is formulated and two methods for the solution of this optimal control problems are developed. The first method is a direct collocation method. Using a given number of collocation points, the optimal control problem is converted to a nonlinear programming problem that can be solved by standard nonlinear programming solvers. The second method is gradient-based.

Using a first-order approximation of the system model, a gradient-based search achieves an approximation of the optimal control solution.

It is observed during the thesis study that the optimal control solutions cannot be determined in real-time. In order to address this problem, the thesis further studies the approximation of the optimal control trajectories by curves that can be parametrized analytically and that can be computed in real-time. To this end, bi-elementary paths that are based on clothoid curves and their analytical approximation by bi-elementary arc-splines are found suitable. The thesis proposed computational methods for the fast computation of lane change trajectories using these curves.

As an application of the developed results, the thesis considers the recent technology of cooperative adaptive cruise control (CACC) for tight vehicle following. Existing CACC designs assume straight roads and hence only consider the longitudinal vehicle dynamics. The thesis extends the existing results to the case of CACC on curved roads.

Keywords: Lane change, longitudinal motion, lateral motion, nonlinear vehicle model, optimal control, clothoid curve.

ÖZ

OTONOM ARAÇLARIN EMNİYETLİ VE VERİMLİ ŞERİT DEĞİŞİKLİKLERİNE YÖNELİK OPTİMAL KONTROL PROBLEMLERİ

ALI, Ardm Haseeb Mohammed

Doktora., Elektronik ve Haberleşme Mühendisliği Anabilim Dalı

Tez Yöneticisi: Doç. Dr. Klaus Werner SCHMIDT

Eylül 2017, 148 sayfa

Akıllı Ulaşım Sistemleri (ITS) yeni iletişim ve kontrol teknoloji gelişmelerini kullanarak trafik akışı ve güvenliğini artırmak, toplam seyahat süresini ve trafik tıkanıklığını azaltmayı amaçlamaktadır. Özellikle kendi kendine giden araçlar yakın gelecekte kayda değer bir etki göstermesi beklenen ITS'nin önemli bir uygulamasıdır.

Kendi kendine giden araçları uygularken şerit değişimlerini fark etmek gerekli bir görevdir. Buna göre, bu tez şerit değişimleri sırasında boylamsal ve lateral manevraların hesaplanmasına odaklanmaktadır. Tez ilk olarak normal sürüş koşullarını temsil etmeye uygun boylamsal ve lateral araç dinamikleri için birkaç model belirlemektedir. Ek olarak boylamsal ve lateral hareketi ayrıştıran yeni bir yöntem sunulmaktadır. Araç modellerine bağlı olarak, şerit değiştirme manevraları için optimal bir kontrol problemi formüle edilip bu optimal kontrol problemlerinin çözümü için iki yöntem geliştirilmektedir. İlk yöntem doğrudan düzenleme yöntemidir. Belirli sayıda düzenleme noktası kullanan optimal kontrol problemi standart lineer-olmayan programlama çözümler ile çözülebilen lineer-olmayan bir programlama problemine dönüştürülmektedir. İkinci yöntem ise gradyan tabanlıdır.

Sistem modelinin birinci derece tahminini kullanan bir gradyan tabanlı araştırma, optimal kontrol çözümünün tahminini elde etmektedir.

Tez çalışması sırasında optimal kontrol çözümlerinin gerçek zamanlı olarak belirlenemeyeceği gözlemlenmiştir. Bu probleme hitap edebilmek için bu tez analitik olarak parametre ile ifade edilebilen ve gerçek zamanlı olarak hesaplanabilen eğriler ile optimal kontrol gezingelerin tahminini çalışmaktadır. Bu amaçla, klotoid eğrilerine dayalı çift-başlangıç yolları ve bunların çift başlangıç kavis kaması ile analitik tahmini uygun bulunmuştur. Tez, bu eğrileri kullanarak şerit değişimi gezingelerinin hızlı hesaplaması için hesaplama yöntemleri önermiştir.

Gelişmiş sonuçların bir uygulaması olarak, bu tez sıkı cihaz takibi için yakın zamanlı kooperatif adaptif seyir sistemleri (CACC) teknolojisini değerlendirmektedir. Mevcut CACC tasarımları düzgün yolları ele aldığından yalnızca boylamsal araç dinamiklerini değerlendirmektedir. Tez CACC vakasının eğimli yollardaki mevcut sonuçlarına da değinmektedir.

Anahtar Kelimeler: Şerit değişimi, boylamsal hareket, lateral hareket, lineer olmayan araç modeli, optimal kontrol, klotoid eğri.

ACKNOWLEDGEMENTS

I would like to express my profound gratitude to my supervisor, Assoc. Prof. Dr. Klaus Werner SCHMIDT, who has supported me throughout my thesis with his patience and knowledge.

I would also like to thank the Scientific and Technological Research Council of Turkey (TUBITAK) for supporting part of the thesis study as part of the project with the award number (115E372).

Special thank my deepest gratitude goes to my beloved parents and my fabulous wife for their endless support.

TABLE OF CONTENTS

STATEMENT OF NON PLAGIARISM.....	iii
ABSTRACT.....	iv
ÖZ.....	vi
ACKNOWLEDGEMENTS.....	viii
TABLE OF CONTENTS.....	ix
LIST OF FIGURES.....	xii
LIST OF TABLES.....	xvii
LIST OF ABBREVIATIONS	xix

CHAPTERS:

1. INTRODUCTION.....	1
2. BACKGROUND.....	5
2.1. Vehicle Models	5
2.1.1 Kinematic Bicycle Model.....	5
2.1.2 Dynamic Vehicle Model in Global Coordinates.....	6
2.1.3 Dynamic Vehicle Model in Local coordinates.....	8
2.1.4 Tire Force.....	9
2.1.5 Simulation.....	13
2.2 Clothoids Curves and Approximations.....	17
2.2.1 Clothoid Definition.....	17
2.2.2 Clothoid Approximation using Arc Splines.....	22

3.	OPTIMAL CONTROL COMPUTATIONS FOR LANE CHANGES.....	28
3.1	Basic Setting and Related Work.....	28
3.2	Lane Change Formulation.....	32
3.2.1	Decoupling The Longitudinal and Lateral Motion.....	32
3.2.2	Transformation of the Decoupled Model to Arc-length Coordinates.....	45
3.2.3	Optimal Control Problem Formulation.....	36
3.3	Collocation Method.....	38
3.3.1	Parameters of Our Collocation Method.....	38
3.3.2	Example Solution.....	42
3.4	Gradient-based Method.....	48
3.4.1	Formulation of Our Method.....	48
3.4.2	Example Solution.....	52
3.5	Comparison And Discussion.....	57
4.	APPROXIMATION OF OPTIMAL CONTROL SOLUTION.....	66
4.1	Control Architecture.....	66
4.2	Elementary Paths and Bi-elementary Paths.....	68
4.2.1	Elementary Path.....	68
4.2.2	Bi-elementary Path.....	69
4.2.3	Parameter Computations.....	73
4.2.4	Newton Method.....	75
4.3	Approximations of Elementary and Bi-elementary Paths.....	83
4.3.1	Approximation of Elementary Paths.....	83
4.3.2	Approximation of Bi-elementary Paths.....	83
4.3.3	Distance Computation.....	84
4.3.4	Trajectory Prediction.....	86
4.4	Approximations of Optimal Control Trajectories.....	87
4.4.1	Explanation of the Method.....	87

4.4.2	Comparison for Low Speeds.....	88
4.4.3	Comparison for High Speeds	97
5.	USAGE OF APPROXIMATED TRAJECTORIES.....	104
5.1	Parameter Selection for Bi-elementary Paths.....	104
5.1.1	Computational Method.....	104
5.1.2	Trajectory Examples	110
5.1.3	Realization and Evaluation	113
5.2	Trajectory Following using Lane Keeping Control.....	118
5.2.1	Road Representation.....	118
5.2.2	Verification of Velocity Profiles.....	119
5.2.3	Evaluation.....	121
5.3	Cooperative Adaptive Cruise Control on Curved Roads.....	128
5.3.1	CACC	128
5.3.2	Decoupling and Practical Implications	131
6.	CONCLUSION AND FUTURE WORK.....	138
	REFERENCES.....	141
	CURRICULUM VITAE	148

LIST OF FIGURES

FIGURES

Figure 2.1	Kinematic Bicycle Model.....	6
Figure 2.2	Dynamic Bicycle Model.....	6
Figure 2.3	Magic formula: dependency on the parameter D	10
Figure 2.4	Magic formula: dependency on the parameter C	11
Figure 2.5	Magic formula: dependency on the parameter B	11
Figure 2.6	Magic formula: dependency on the parameter E	12
Figure 2.7	Vehicle simulation: $v_0 = 20$, $F_{lf} = 0$, $\delta = 1^\circ$	13
Figure 2.8	Vehicle simulation: $v_0 = 20$, $F_{lf} = 500$, $\delta = 1^\circ$	14
Figure 2.9	Vehicle simulation: $v_0 = 20$, $F_{lf} = 0$, $\delta = 0.3^\circ t$	15
Figure 2.10	Vehicle simulation: $v_0 = 20$, $F_{lf} = 0$, $\delta = 1^\circ \sin(2\pi t)$	15
Figure 2.11	Vehicle simulation: $v_0 = 20$, $F_{lf} = -500$, $\delta = 1^\circ \sin(2\pi t)$	16
Figure 2.12	Vehicle simulation: $v_0 = 30$, $F_{lf} = 0$, $\delta = 0.01-0.05 \sigma(t-3)$	16
Figure 2.13	Illustration of a clothoid curve.....	17
Figure 2.14	Clothoid curve $\mathcal{Q}(0,0,0, .015,100)$	18
Figure 2.15	Clothoid curve $\mathcal{Q}(0,0,0, .015,50)$	19
Figure 2.16	Clothoid curve $\mathcal{Q}(0,0.2,0, .015,100)$	19
Figure 2.17	Clothoid curve $\mathcal{Q}(0,0, .005, .015,100)$	20
Figure 2.18	Clothoid curve $\mathcal{Q}(0,0,0, - .015,100)$	20
Figure 2.19	Clothoid curve $\mathcal{Q}(0,0,0.015,0,100)$	21
Figure 2.20	Arc spline $\mathcal{Q}^\wedge(0,0,0,1.2,5,5)$	25
Figure 2.21	Clothoid curve $\mathcal{Q}^\wedge(0,0,0.3,1.2,5,5)$	26
Figure 2.22	Comparison of $\mathcal{Q}(0,0,0,0.015,100)$ and $\mathcal{Q}^\wedge(0,0,0,0.015,100,5)$	27
Figure 2.23	Comparison of $\mathcal{Q}(0,0,0,0.015,100)$ and $\mathcal{Q}^\wedge(0,0,0,0.015,100,10)$	27
Figure 3.1	Basic lane change maneuver.....	28
Figure 3.2	Optimal trajectory for $S = 50$, $a_r = -2$ and $a_r = -1$	43
Figure 3.3	Optimal trajectory for $S = 60$; $a_r \in \{-2, -1, 0, 1, 2\}$	44
Figure 3.4	Optimal trajectory for $S = 70$; $a_r \in \{-2, -1, 0, 1, 2\}$	44
Figure 3.5	Optimal trajectory for $S = 80$; $a_r \in \{-2, -1, 0, 1, 2\}$	45
Figure 3.6	Optimal trajectory for $S = 90$; $a_r \in \{-2, -1, 0, 1, 2\}$	45

Figure 3.7	Optimal trajectory for $S = 100$; $a_r \in \{-2, -1, 0, 1, 2\}$	46
Figure 3.8	Optimal trajectory for $S = 110$; $a_r \in \{-2, -1, 0, 1, 2\}$	46
Figure 3.9	Optimal trajectory for $S = 120$; $a_r \in \{-2, -1, 0, 1, 2\}$	47
Figure 3.10	Gradient method: $S = 40, \Delta Y = 3.7, a \in \{-2, -1, 0, 1, 2\}$	52
Figure 3.11	Gradient method: $S = 50, \Delta Y = 3.7, a \in \{-2, -1, 0, 1, 2\}$	53
Figure 3.12	Gradient method: $S = 60, \Delta Y = 3.7, a \in \{-2, -1, 0, 1, 2\}$	53
Figure 3.13	Gradient method: $S = 70, \Delta Y = 3.7, a \in \{-2, -1, 0, 1, 2\}$	54
Figure 3.14	Gradient method: $S = 80, \Delta Y = 3.7, a \in \{-2, -1, 0, 1, 2\}$	54
Figure 3.15	Gradient method: $S = 90, \Delta Y = 3.7, a \in \{-2, -1, 0, 1, 2\}$	55
Figure 3.16	Gradient method: $S = 100, \Delta Y = 3.7, a \in \{-2, -1, 0, 1, 2\}$	55
Figure 3.17	Gradient method: $S = 110, \Delta Y = 3.7, a \in \{-2, -1, 0, 1, 2\}$	56
Figure 3.18	Gradient method: $S = 120, \Delta Y = 3.7, a \in \{-2, -1, 0, 1, 2\}$	56
Figure 3.19	Comparison of optimal trajectories for $S=50, v=20$ and $a \in \{-2, -1, 0, 1, 2\}$.	57
Figure 3.20	Comparison of optimal trajectories for $S=60, v=20$ and $a \in \{-2, -1, 0, 1, 2\}$.	58
Figure 3.21	Comparison of optimal trajectories for $S=70, v=20$ and $a \in \{-2, -1, 0, 1, 2\}$.	59
Figure 3.22	Comparison of optimal trajectories for $S=70, v=30$ and $a \in \{-2, -1, 0, 1, 2\}$.	59
Figure 3.23	Comparison of optimal trajectories for $S=80, v=30$ and $a \in \{-2, -1, 0, 1, 2\}$.	60
Figure 3.24	Comparison of optimal trajectories for $S=90, v=30$ and $a \in \{-2, -1, 0, 1, 2\}$.	60
Figure 3.25	Comparison of optimal trajectories for $S=90, v=40$ and $a \in \{-2, -1, 0, 1, 2\}$.	61
Figure 3.26	Comparison of optimal trajectories for $S=100, v=40$ and $a \in \{-2, -1, 0, 1, 2\}$.	61
Figure 3.27	Comparison of optimal trajectories for $S=100, v=40$ and $a \in \{-2, -1, 0, 1, 2\}$.	62
Figure 3.28	Comparison of optimal trajectories for $S=100, v=50$ and $a \in \{-2, -1, 0, 1, 2\}$.	62
Figure 3.29	Comparison of optimal trajectories for $S=110, v=50$ and $a \in \{-2, -1, 0, 1, 2\}$.	63
Figure 3.30	Comparison of optimal trajectories for $S=120, v=50$ and $a \in \{-2, -1, 0, 1, 2\}$.	63
Figure 3.31	Comparison of optimal trajectories for $S=50, v=20$ and $a \in \{-2, -1, 0, 1, 2\}$.	64
Figure 3.32	Comparison of optimal trajectories for $S=70, v=30$ and $a \in \{-2, -1, 0, 1, 2\}$.	65
Figure 4.1	Control architecture for trajectory following during lane changes.....	67
Figure 4.2	Elementary path $\mathcal{E} (0,0,0,0.015,100)$	68

Figure 4.3	Approximation of $D(\alpha)$	70
Figure 4.4	Components of a bi-elementary path.....	70
Figure 4.5	$\beta(S, k_1, \lambda, \gamma)$ for $S = 100, k_1 = 0.005, \gamma = 1$ and different λ	73
Figure 4.6	$\beta(S, k_1, \lambda, \gamma)$ for $S = 100, k_1 = 0.005, \lambda = 0.5$ and different γ	74
Figure 4.7	$g_1(\alpha, \gamma)$ and $g_1(\alpha, \gamma)$ for $\gamma \in (0, 1]$ and $\alpha \in [0, \pi/4]$	77
Figure 4.8	$\beta(S, k_1, \lambda, \gamma)$ for $\Delta Y = 3.7, \lambda = 0.5, \gamma = 1$ and different k_1	79
Figure 4.9	$\beta(S, k_1, \lambda, \gamma)$ for $\Delta Y = 3.7, k_1 = 0.01, \gamma = 1$ and different λ	80
Figure 4.10	$\beta(S, k_1, \lambda, \gamma)$ for $\Delta Y = 3.7, k_1 = 0.01, \lambda = 0.5$ and different γ	80
Figure 4.11	$g_2(\alpha, \gamma)$ for $\gamma \in (0, 1]$ and $\alpha \in [0, \pi/4]$	81
Figure 4.12	$\beta(S, k_1, \lambda, \gamma)$ for $\Delta Y = 3.7, \lambda = 0.5, \gamma = 1$ and different S	82
Figure 4.13	$\beta(S, k_1, \lambda, \gamma)$ for $\Delta Y = 3.7, S = 80, \gamma = 1$ and different λ	82
Figure 4.14	$\beta(S, k_1, \lambda, \gamma)$ for $\Delta Y = 3.7, S = 80, \lambda = 0.5$ and different γ	83
Figure 4.15	Elementary path $\varepsilon(0, 0, 0, 0.015, 100)$ and approximation $\hat{\varepsilon}(0, 0, 0, 0.015, 100, 5)$	84
Figure 4.16	Distance error for a line segment: (a) positive error; (b) negative error.....	85
Figure 4.17	Distance error for an arc segment: (a) positive radius; (b) negative radius.....	86
Figure 4.18	Computation of the predicted vehicle trajectory \tilde{Y}	88
Figure 4.19	Optimal control approximation for $S = 50, \nu = 20$ and different values of a	90
Figure 4.20	Optimal control approximation for $S = 60, \nu = 20$ and different values of a	91
Figure 4.21	Optimal control approximation for $S = 70, \nu = 20$ and different values of a	91
Figure 4.22	Optimal control approximation for $S = 80, \nu = 20$ and different values of a	92
Figure 4.23	Optimal control approximation for $S = 90, \nu = 20$ and different values of a	92
Figure 4.24	Optimal control approximation for $S = 100, \nu = 20$ and different values of a	93
Figure 4.25	Optimal control approximation for $S = 110, \nu = 20$ and different values of a	93
Figure 4.26	Optimal control approximation for $S = 120, \nu = 20$ and different values of a	94

Figure 4.27	Trajectory following for $v = 20$ and $a_r = -2$	95
Figure 4.28	Trajectory following for $v = 20$ and $a_r = -1$	95
Figure 4.29	Trajectory following for $v = 20$ and $a_r = 0$	96
Figure 4.30	Trajectory following for $v = 20$ and $a_r = 1$	96
Figure 4.31	Trajectory following for $v = 20$ and $a_r = 2$	97
Figure 4.32	Optimal control approximation for $S = 70$, $v = 40$ and different values of a	98
Figure 4.33	Optimal control approximation for $S = 80$, $v = 40$ and different values of a	99
Figure 4.34	Optimal control approximation for $S = 90$, $v = 40$ and different values of a	99
Figure 4.35	Optimal control approximation for $S = 100$, $v = 40$ and different values of a	100
Figure 4.36	Optimal control approximation for $S = 110$, $v = 40$ and different values of a	100
Figure 4.37	Optimal control approximation for $S = 120$, $v = 40$ and different values of a	101
Figure 4.38	Trajectory following for $v = 40$ and $a_r = -2$	102
Figure 4.39	Trajectory following for $v = 40$ and $a_r = -1$	102
Figure 4.40	Trajectory following for $v = 40$ and $a_r = 0$	103
Figure 4.41	Trajectory following for $v = 40$ and $a_r = 1$	103
Figure 4.42	Trajectory following for $v = 40$ and $a_r = 2$	104
Figure 5.1	Evaluation of f_s in (5.14) for different values of γ	109
Figure 5.2	Trajectory computation for $v_0 = 20\text{m/sec}$, $\gamma = 1$, $\mu = 0.82$ and $a_{\max} = 1\text{m/sec}^2$ (left), $a_{\max} = 2\text{m/sec}^2$ (middle) and $a_{\max} = 5\text{m/sec}^2$ (right).....	111
Figure 5.3	Trajectory computation for $v_0 = 40\text{m/sec}$, $\gamma = 1$, $\mu = 0.82$ and $a_{\max} = 1\text{m/sec}^2$ (left), $a_{\max} = 2\text{m/sec}^2$ (middle) and $a_{\max} = 5\text{m/sec}^2$ (right).....	112
Figure 5.4	Trajectory computation for $v_0 = 20\text{m/sec}$, $\gamma = 1$, $\mu = 0.5$ and $a_{\max} = 1\text{m/sec}^2$ (left), $a_{\max} = 2\text{m/sec}^2$ (middle) and $a_{\max} = 4\text{m/sec}^2$ (right).....	112
Figure 5.5	Trajectory computation for $v_0 = 20\text{m/sec}$, $\mu = 0.82$ and $a_{\max} = 2\text{m/sec}^2$ and different values of γ	113
Figure 5.6	Trajectory following for $v_0 = 20\text{m/sec}$, $a_{\max} = 2\text{m/sec}^2$, $\mu = 0.82$ and $\Delta Y = 3.7\text{m}$	115
Figure 5.7	Trajectory following for $v_0 = 20\text{m/sec}$, $a_{\max} = 4\text{m/sec}^2$, $\mu = 0.82$ and $\Delta Y = 3.7\text{m}$	116

Figure 5.8	Trajectory following for $v_0 = 40\text{m/sec}$, $a_{\text{max}} = 2\text{m/sec}^2$, $\mu = 0.82$ and $\Delta Y = 3.7\text{m}$	116
Figure 5.9	Trajectory following for $v_0 = 20\text{m/sec}$, $a_{\text{max}} = 2\text{m/sec}^2$, $\mu = 0.82$ and $\Delta Y = 7.4\text{m}$	117
Figure 5.10	Trajectory following for $v_0 = 20\text{m/sec}$, $a_{\text{max}} = 2\text{m/sec}^2$, $\mu = 0.5$ and $\Delta Y = 3.7\text{m}$	117
Figure 5.11	Trajectory following for $v_0 = 40\text{m/sec}$, $a_{\text{max}} = 2\text{m/sec}^2$, $\mu = 0.5$ and $\Delta Y = 3.7\text{m}$	118
Figure 5.12	Example road trajectory \mathcal{J}	120
Figure 5.13	Road curvature (upper) and velocity comparison (lower) for $v_{0.82}$	123
Figure 5.14	Acceleration comparison for $v_{0.82}$	123
Figure 5.15	Tracking error for $v_{0.82}$	124
Figure 5.16	Road curvature (upper) and velocity comparison (lower) for $v_{0.5}$	125
Figure 5.17	Acceleration comparison for $v_{0.5}$	126
Figure 5.18	Tracking error for $v_{0.5}$	126
Figure 5.19	Road curvature (upper) and velocity comparison (lower) for $v_{0.5}$	127
Figure 5.20	Acceleration comparison for $v_{0.5}$	128
Figure 5.21	Tracking error for $v_{0.5}$	128
Figure 5.22	Vehicle following scenario.....	129
Figure 5.23	CACC realization for a generic vehicle i	130
Figure 5.24	Control architecture for a generic vehicle i	133
Figure 5.25	Created road profile (upper); road curvature ρ (lower).....	134
Figure 5.26	Simulation results for a curved road with zero acceleration.....	135
Figure 5.27	Simulation results for a curved road with a given acceleration profile.....	136
Figure 5.28	Simulation results for a curved road with two lane changes.....	136

LIST OF TABLES

Table 2.1:	Vehicle parameters.....	13
Table 3.1:	Comparison of optimal cost ($\cdot 10^{-3}$) for collocation and gradient-based method.....	67
Table 4.1	Maximum distance for the optimal control approximations in cm.....	92
Table 4.2	Parameters (k_1, λ, γ) for the optimal control approximations.....	96
Table 4.3	Comparison of the optimal cost for the gradient method and the cost of trajectory following ($\cdot 10^{-3}$).....	97
Table 4.4	Maximum distance for the optimal control approximations in cm.....	100
Table 4.5	Parameters (k_1, λ, γ) for the optimal control approximations.....	103
Table 4.6	Comparison of the optimal cost for the gradient method and the cost of trajectory following for $v = 40$	103
Table 5.1	Parameters of the example road trajectory.....	123
Table 5.2	Vehicle and CACC controller parameters.....	136

LIST OF ABBREVIATIONS

ITS	Intelligent Transportation Systems.
CACC	Cooperative Adaptive Cruise Control.
ACC	Adaptive Cruise Control.
V2V	Vehicle to Vehicle.
X	Longitudinal Position.
Y	Lateral Position.
δ	Steering Angle.
Φ	Yaw Angle.
CG	Center of Gravity.
m	Vehicle Mass.
I_{zz}	Moment of Inertia.
β	Slip Angle.
μ	Road friction Coefficient.
V_i	Velocity of Vehicle i .
a_r	Acceleration.
a_{long}	Longitudinal acceleration ,
a_{lat}	Lateral acceleration.
S	Arc-length.
k_s	Initial Curvature.
k_f	Final Curvature.
P_s	Starting Point.
Ψ_s	Orientation Angle.
RA	Radius.
d_i	Actual Inter-Vehicle Distance of Vehicle i .

$d_{r,i}$	Desired Inter-Vehicle Distance of Vehicle i.
r_i	Standstill Distance of Vehicle i.
h	Time Headway.
e_i	Spacing Error of Vehicle i.
q_i	Rear Bumper Position of Vehicle i.
L_i	Length of Vehicle i.
G	Plant of Vehicle.
θ	Communication Delay.
ϕ	Possible Plant Delay.
Γ_i	Complementary Sensitivity of Vehicle i.
τ	Time Constant.
$H(s)$	Spacing Policy.
K_{fb}	Feedback Controller.
K_{ff}	Feedforward Controller.
K_{fbo}	Main feedback Controller.
K_{ffo}	Main feedforward Controller.
F_{lf}	(Attraction force) longitudinal force at the front wheel in the wheel direction.
F_{lr}	Longitudinal force at the rear wheel in wheel direction is zero if rolling is assumed.
F_{cr}	Lateral force at the rear wheel perpendicular to the wheel direction.
F_{cf}	Lateral (cornering) force at the front wheel perpendicular to the wheel direction.
α_f	Tire Slip (front wheel).
α_r	Tire Slip(rear wheel).
F_{xf}	Longitudinal Forces (front wheel).
F_{xr}	Longitudinal Forces (rear wheel).

F_{yf} Lateral Force(front wheel).

F_{yr} Lateral Force(rear wheel).



CHAPTER 1

Introduction

Rapid technology development and improvement of human life quality led to a considerable increase in traffic. It also becomes a reason for increasing the demand for a more efficient and smarter usage of the currently available transportation infrastructure. The natural consequence of these requirements is the emergence of *Intelligent Transportation Systems* (ITS). ITS deployments aim at increasing the traffic throughput and safety, reducing the total travel time and traffic congestion using novel achievements of communication and control technologies [1, 2, 3, 4]. Integration of communication technologies such as vehicle-to-vehicle (V2V) and vehicle-to-infrastructure (V2I) communication in ITS give an opportunity for vehicle cooperation, management and coordination of vehicle maneuvers, provisioning of critical information to road users.

Among the most significant goals of ITS are traffic throughput increase, traffic safety and reduction of traveling delays. They are targeted implicitly or explicitly in any ITS application. Different requirements are associated with the stated goals on different levels of a traffic network. On the overall network level, the route of each vehicle from its starting position to its destination has to be decided. This issue is addressed by dynamic route guidance methods that for example suggest the avoidance of congested areas [5][6][7]. Nevertheless, such methods neglect how vehicles move on the selected route. This task is handled on the next level of the traffic network that is concerned with the traffic flow on highways or urban networks. Finally, methods for the longitudinal and lateral control of vehicles such as cooperative adaptive cruise control (CACC) and lane changing control allow the control of individual vehicle maneuvers while ensuring traffic safety

[8, 9, 10, 11, 12, 13, 26, 14].

The topic of this thesis is the longitudinal and lateral control of self-driving vehicles (SVDs) in the scope of ITSs. Such SVDs will be available in the near future [15] and it is predicted by IEEE that SVDs will constitute 75 % of cars by 2040 [16]. In this context, the main task of this thesis is the design of suitable vehicle trajectories that support vehicle maneuvers such as lane changes in dense vehicle traffic. Hereby, trajectories are considered suitable if they can be easily applied in real-time vehicle applications and if they can be used as building blocks for higher-level planning tasks such as traffic flow control and traffic routing.

The suggested solution is based on a combined optimization of the lateral and longitudinal movement in the framework of *optimal control* [17]. In addition, the thesis investigates the convenient approximation of the optimal control by bi-elementary paths that are formed as a concatenation of clothoid curves. Based on this approximation, the thesis develops methods for the real-time computation of suitable lane change trajectories. Finally, the thesis presents several applications that can be designed based on the developed results. The main contributions of the thesis are listed as follows.

- A new nonlinear vehicle model for the longitudinal and lateral motion is proposed based on a dynamic bicycle model. Using the idea of feedback linearization, the traction force of the vehicle is computed so as to decouple the longitudinal motion from the lateral motion. This is essential when maintaining a desired vehicle speed or acceleration while simultaneously performing lateral maneuvers.
- Instead of working with a time-based vehicle model, the vehicle model is converted to a representation that depends on the arc-length. Such representation is beneficial when comparing the resulting vehicle trajectories on the road, when determining approximations and when following the computed trajectories.
- An optimal control problem for lane changes is formulated based on the developed vehicle model. The formulation is general and can be used for

representations of the vehicle model in different coordinates.

- A collocation method for the solution of the optimal control problem is developed. Using a given number of collocation points and third-order polynomials for approximating the relevant state variables, the optimal control problem is converted to a nonlinear programming problem. A reliable solver is used to compute direct solutions of the optimal control problem for lane changes.
- A gradient-based method for solving the optimal control problem for lane changes is developed. Using a finite difference approximation of the system model, a gradient-based search allows computing the optimal control solution.
- Optimal control solutions are computed for a wide range of maneuvers, involving different velocities, accelerations and lane change distances. It is shown that the gradient-based method determines better solutions regarding the steering angle for performing optimal lane change maneuvers.
- The main disadvantage of applying optimal control is the fact that optimal control trajectories cannot be computed in real-time. Analyzing the resulting optimal control trajectories, it is determined that they can be tightly approximated by bi-elementary paths. Such paths are formed by concatenating clothoid curves and an analytical approximation of such paths by arc-spline trajectories is proposed.
- The thesis determines an analytical bound on the path curvature depending on the maximum velocity profile of a vehicle during a lane change. Using this bound, the thesis proposes a computational procedure for selecting the parameters of bi-elementary paths that are suitable for lane change trajectories. This parameter selection can be efficiently carried out in real-time based on the current vehicle velocity and a bound on the admissible acceleration.

- The thesis further shows that the developed methods can be used to improve the technology of cooperative adaptive cruise control (CACC) that realizes tight vehicle following based on distance measurements and communicated state information among vehicles [18, 19, 20, 21, 22, 23]. Noting that the existing CACC methods such as [19, 20, 21] are developed under the assumption of straight roads, the case of CACC on curved roads is solved in the thesis based on decoupling the longitudinal vehicle motion from the lateral dynamics.

The remainder of the thesis is organized as follows. Chapter 2 gives the background information about nonlinear vehicle models and clothoid curves that are used for approximating lane change trajectories. In Chapter 3, the optimal control problem for lane changes is formulated and solved using collocation and a gradient-based method. The approximation of optimal control trajectories by bi-elementary paths is investigated in Chapter 4 and the usage of the approximated trajectories in different applications for self-driving vehicle is studied in Chapter 5. Chapter 6 gives conclusions and discusses future work.

CHAPTER 2

Background

This chapter provides the background information for this thesis. The vehicle models used in the scope of the thesis are introduced and illustrated in Section 2.1. In addition, Section 2.2 provides the basic information about a certain type of clothoid curves that are used for representing lane change trajectories in this thesis.

2.1 Vehicle Models

2.1.1 Kinematic Bicycle Model

The most simple model is a purely kinematic bicycle model [24] with three degrees of freedom as shown in (Fig. 2.1). The three degrees of freedom are represented by the vehicle longitudinal position (X), lateral position (Y) and the vehicle yaw angle (Φ). The vehicle position is measured along the coordinate axes to the position of the rear wheel of the vehicle. The vehicle yaw angle (Φ) is measured with respect to the global (X) axis. The longitudinal velocity of the vehicle at the center of gravity is denoted as v .

It has to be noted that this model only captures kinematics of the vehicle and does not consider any dynamics. In particular, the vehicle speed is assumed to be a constant v . The model equations are

$$\dot{X} = v \cos(\Psi) \tag{2.1}$$

$$\dot{Y} = v \sin(\Phi) \tag{2.2}$$

$$\dot{\Psi} = \frac{v}{a+b} \tan(\delta) \tag{2.3}$$

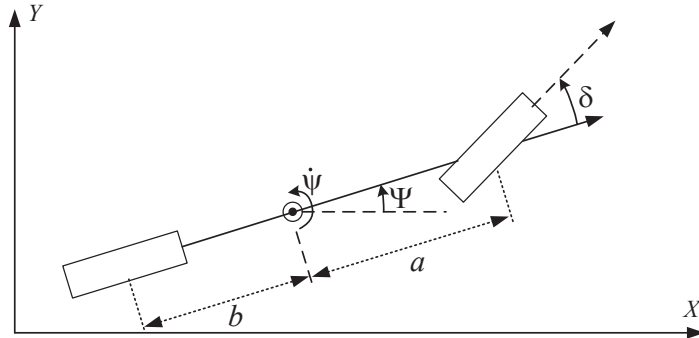


Figure 2.1: Kinematic Bicycle Model

2.1.2 Dynamic Vehicle Model in Global Coordinates

Since the kinematic model in the previous section does not correctly represent the vehicle motion in realistic driving scenarios, the study in this thesis is based on the dynamic bicycle model as shown in Fig. 2.2. The global coordinates are X, Y and Ψ and a body coordinate frame with the coordinates x, y, ψ is attached to the vehicle center of gravity (CG).

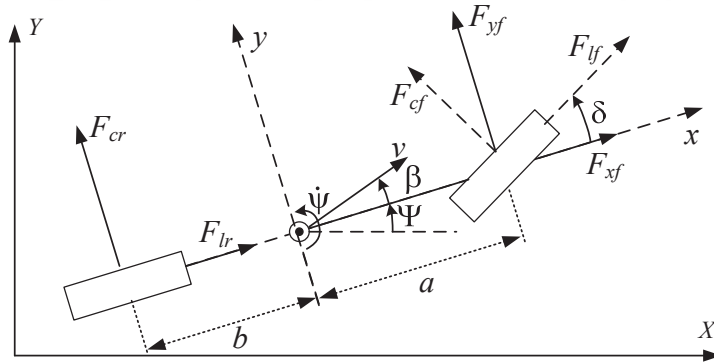


Figure 2.2: Dynamic Bicycle Model

The relation between the inertial and body coordinates is

$$\dot{X} = \dot{x} \cos(\Psi) - \dot{y} \sin(\Psi) \quad (2.4)$$

$$\dot{Y} = \dot{x} \sin(\Psi) + \dot{y} \cos(\Psi) \quad (2.5)$$

$$\dot{\Psi} = \dot{\psi}. \quad (2.6)$$

The dynamic equations in the body frame are given as

$$\ddot{x} = \dot{y}\dot{\psi} + \frac{F_{xf} + F_{xr}}{m} \quad (2.7)$$

$$\ddot{y} = -\dot{x}\dot{\psi} + \frac{F_{yf} + F_{yr}}{m} \quad (2.8)$$

$$\ddot{\psi} = \frac{aF_{yf} - bF_{yr}}{I_{zz}} \quad (2.9)$$

Hereby, m is the vehicle mass, I_{zz} is the moment of inertia and a , b are the distances between the wheels and the CG. The longitudinal forces F_{xf} , F_{xr} and the lateral forces F_{yf} , F_{yr} at the front and rear tires are computed using (2.10) to (2.13) depending on the respective forces in the wheel direction F_{lf} , F_{cf} , F_{lr} and F_{cr} .

$$F_{xf} = F_{lf} \cos(\delta) - F_{cf} \sin(\delta) \text{ (front wheel, x-direction)} \quad (2.10)$$

$$F_{yf} = F_{lf} \sin(\delta) + F_{cf} \cos(\delta) \text{ (front wheel, y-direction)} \quad (2.11)$$

$$F_{xr} = F_{lr} = 0 \text{ (rear wheel, x-direction)} \quad (2.12)$$

$$F_{yr} = F_{cr} \text{ (rear wheel, y-direction)} \quad (2.13)$$

F_{lf} is the traction force provided by the engine and $F_{lr} = 0$ when using actuation at the front tires. The forces F_{cf} and F_{cr} depend on the lateral tire slip angles α_f (front) and α_r (rear) of the respective tire:

$$\alpha_f = \tan^{-1}\left(\frac{\dot{y} + a\dot{\psi}}{\dot{x}}\right) - \delta \quad (2.14)$$

$$\alpha_r = \tan^{-1}\left(\frac{\dot{y} - b\dot{\psi}}{\dot{x}}\right) \quad (2.15)$$

Then, the tire forces can be computed using the magic formula [25] that is frequently used in the literature [26, 11, 27]. A detailed description of the tire forces is given in Section 2.1.4.

For further use in the thesis, we finally transform the model in (2.7) to (2.9) to

the global coordinates X, Y, Ψ . Using (2.4) to (2.6), it holds that

$$\begin{aligned}\dot{X} &= \dot{x} \cos(\Psi) - \dot{x} \sin(\Psi) \dot{\Psi} - \dot{y} \sin(\Psi) - \dot{y} \cos(\Psi) \dot{\Psi} \\ \dot{Y} &= \dot{x} \sin(\Psi) + \dot{x} \cos(\Psi) \dot{\Psi} + \dot{y} \cos(\Psi) - \dot{y} \sin(\Psi) \dot{\Psi} \\ \dot{\Psi} &= \dot{\psi}.\end{aligned}$$

Substituting (2.7) to (2.8) into these equations leads to

$$\dot{X} = F_{lf} \frac{(\cos(\delta) \cos(\Psi) - \sin(\delta) \sin(\Psi))}{m} - F_{cf} \frac{\sin(\delta) \cos(\Psi) + \cos(\delta) \sin(\Psi)}{m} - F_{cr} \frac{\sin(\Psi)}{m}, \quad (2.16)$$

$$\dot{Y} = F_{lf} \frac{\cos(\delta) \sin(\Psi) + \sin(\delta) \cos(\Psi)}{m} + F_{cf} \frac{\cos(\delta) \cos(\Psi) - \sin(\delta) \sin(\Psi)}{m} + F_{cr} \frac{\cos(\Psi)}{m}, \quad (2.17)$$

$$\dot{\Psi} = \frac{a(F_{lf} \sin(\delta) + F_{cf} \cos(\delta)) - b F_{cr}}{I_{zz}}. \quad (2.18)$$

In addition, the slip angles in (2.14) and (2.15) can be formulated using the global coordinates as

$$\alpha_f = \tan^{-1} \left(\frac{\dot{Y} \cos(\Psi) - \dot{X} \sin(\Psi) + a \dot{\Psi}}{\dot{X} \cos(\Psi) + \dot{Y} \sin(\Psi)} \right) - \delta \quad (2.19)$$

$$\alpha_r = \tan^{-1} \left(\frac{\dot{Y} \cos(\Psi) - \dot{X} \sin(\Psi) - b \dot{\Psi}}{\dot{X} \cos(\Psi) + \dot{Y} \sin(\Psi)} \right) \quad (2.20)$$

2.1.3 Dynamic Vehicle Model in Local coordinates

The model in the global coordinates in Section 2.1.2 is formulated using the second time-derivatives of the global position X, Y . In this section, an alternative model that only requires the first time-derivatives of the position coordinates is derived based on the side-slip angle β similar to [28, 26]. To this end, we first write the vehicle model in (2.7) to (2.9) in terms of the velocity $v = \sqrt{\dot{x}^2 + \dot{y}^2}$ of the CG and the slip angle $\beta = \tan^{-1}(\dot{y}/\dot{x})$. We compute

$$\dot{\beta} = \frac{1}{1 + \left(\frac{\dot{y}}{\dot{x}}\right)^2} \left(\frac{\dot{x}\ddot{y} - \dot{y}\ddot{x}}{\dot{x}^2} \right) = \frac{1}{\dot{x}^2 + \dot{y}^2} (\dot{x}\ddot{y} - \dot{y}\ddot{x}) = \frac{1}{v^2} (\dot{x}\ddot{y} - \dot{y}\ddot{x}).$$

Substituting (2.7) and (2.8), we obtain

$$\dot{\beta} = \frac{(F_{lf} \sin(\delta) + F_{cf} \cos(\delta) + F_{cr}) \cos(\beta)}{mv} - \dot{\Psi} \cos^2(\beta) \quad (2.21)$$

$$\ddot{\Psi} = \frac{(F_{lf} \sin(\delta) + F_{cf} \cos(\delta)) a - F_{cr} b}{I_{zz}} \quad (2.22)$$

$$\dot{X} = v \cos(\Psi + \beta) \quad (2.23)$$

$$\dot{Y} = v \sin(\Psi + \beta). \quad (2.24)$$

2.1.4 Tire Force

In order to study the dynamic behavior of vehicles for designing control systems, a tire model is needed. The magic formula model of Pacejka is a popular model for this purpose. It is a semi-empirical tire model that determines the tire force depending on the respective tire slip. Its basic form is given by the following equations [29, 25]:

$$F_{cf} = D_{cf} \sin(C_{cf} \tan^{-1}(B_{cf} \alpha_f - E_{cf}(B_{cf} \alpha_f - \tan^{-1}(B_{cf} \alpha_f)))) \quad (2.25)$$

$$F_{cr} = D_{cr} \sin(C_{cr} \tan^{-1}(B_{cr} \alpha_r - E_{cr}(B_{cr} \alpha_r - \tan^{-1}(B_{cr} \alpha_r)))). \quad (2.26)$$

In this thesis, we make the common assumption that the parameters for the rear and front tires are equal. That is, we use B , C , D and E . Here, D determines the maximum possible lateral tire force, which depends on the normal force of the vehicle. Using the vehicle mass m and a road friction coefficient μ , the maximum lateral force is given by

$$D = \mu m g. \quad (2.27)$$

The remaining parameters are shape parameters that determine the dependency of the tire force on the slip angle. The magic formula is illustrated by several parameter choices in the following figures. Fig. 2.3 shows that the maximum/minimum force is adjusted by the parameter D . The final force for large values of the slip angle α_f depends on the parameter C as can be seen in Fig. 2.4. The location of

the maximum/minimum force changes with the choice of B (see Fig. 2.5) and the sharpness of the maximum of the curve depends on E (see Fig. 2.6).

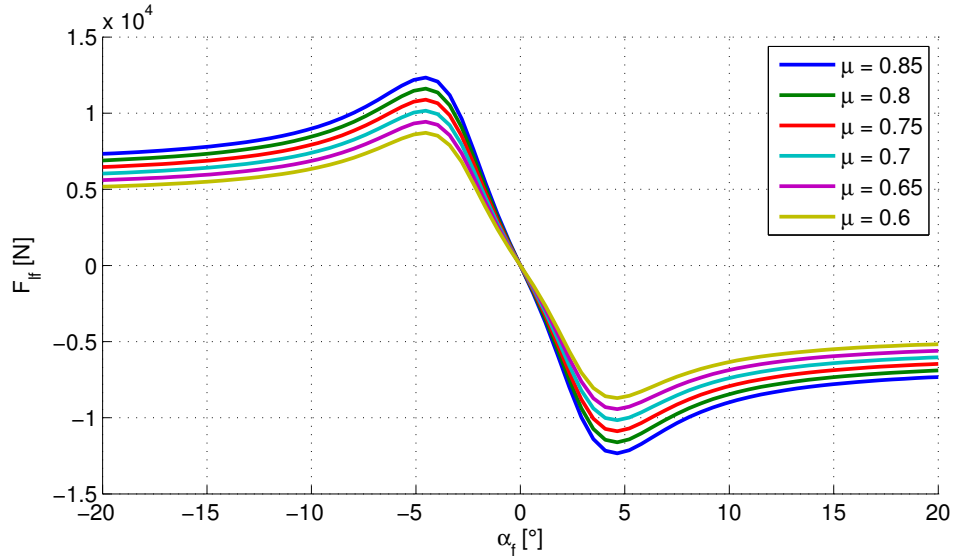


Figure 2.3: Magic formula: dependency on the parameter D .

In general, the parameter choice for each application depends on the vehicle and the specific tires used. In this thesis, we use the parameters from [30] as summarized in Table 2.1.

Table 2.1: Vehicle parameters.

m	I_{zz}	B	C	D	E	a	b
1480	1950	8.22	1.65	$-1.7 \cdot 10^4$	-10	1.421	1.029

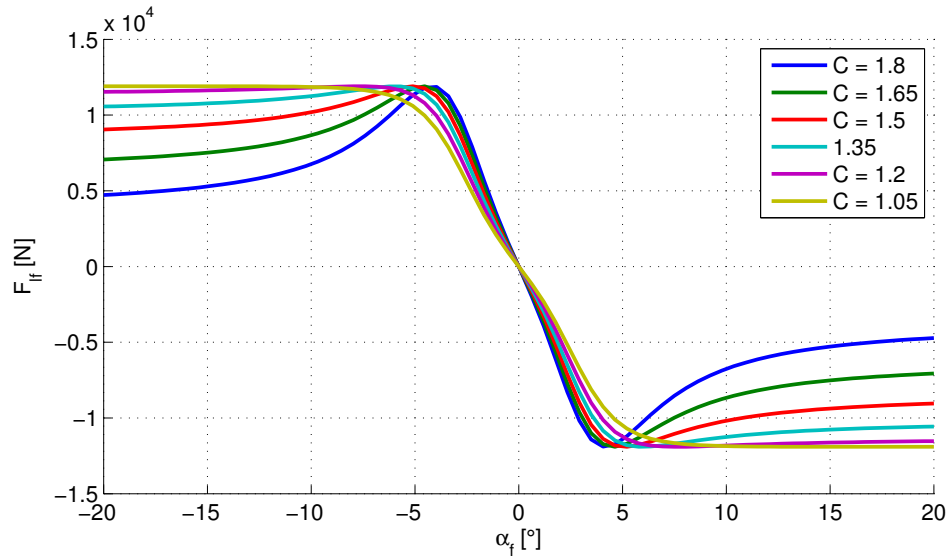


Figure 2.4: Magic formula: dependency on the parameter C .

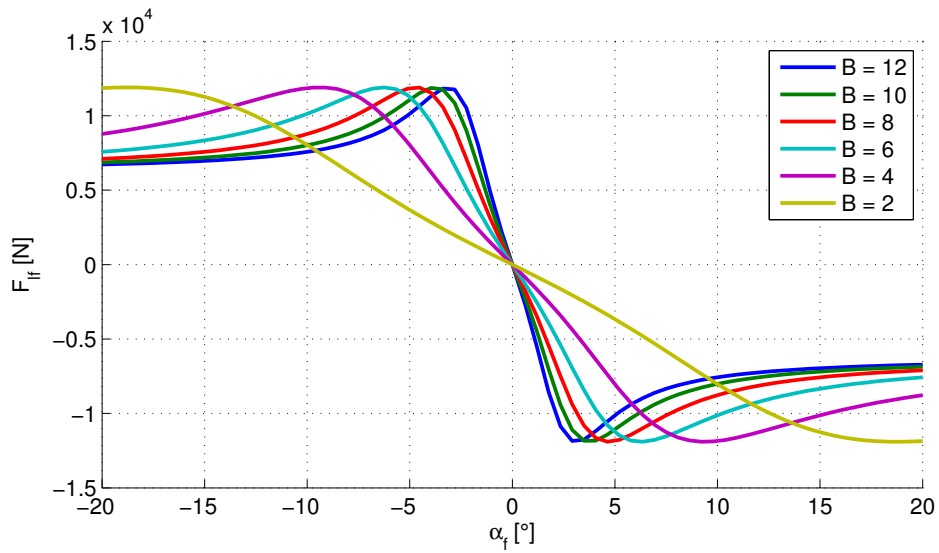


Figure 2.5: Magic formula: dependency on the parameter B .

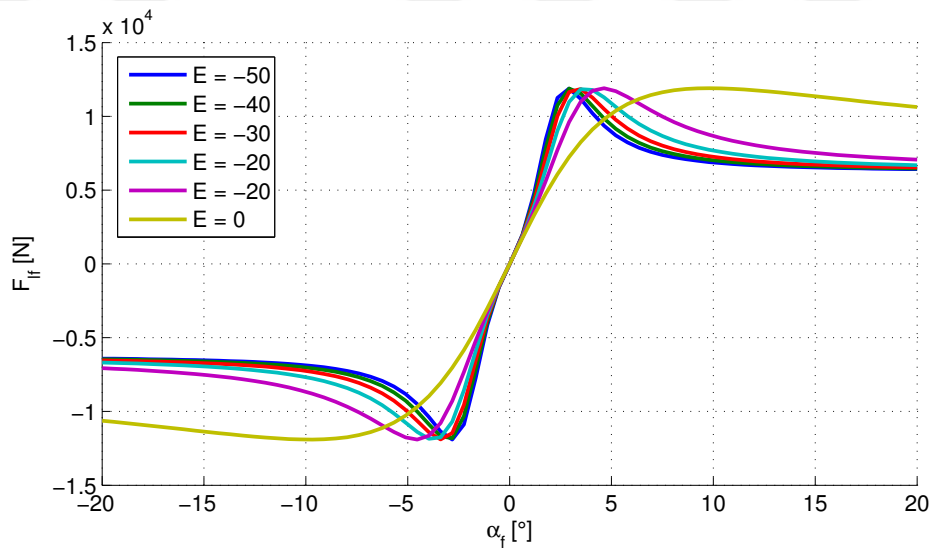


Figure 2.6: Magic formula: dependency on the parameter E .

2.1.5 Simulation

In order to validate the vehicle model, we present several simulation examples of vehicle maneuvers. Fig. 2.7 to 2.12 show simulations with an initial velocity of $v_0 = 20$ m/sec and different steering angles δ and traction forces F_{lf} .

Fig. 2.7 shows a left turn with a steering angle of $\delta = 1^\circ$.

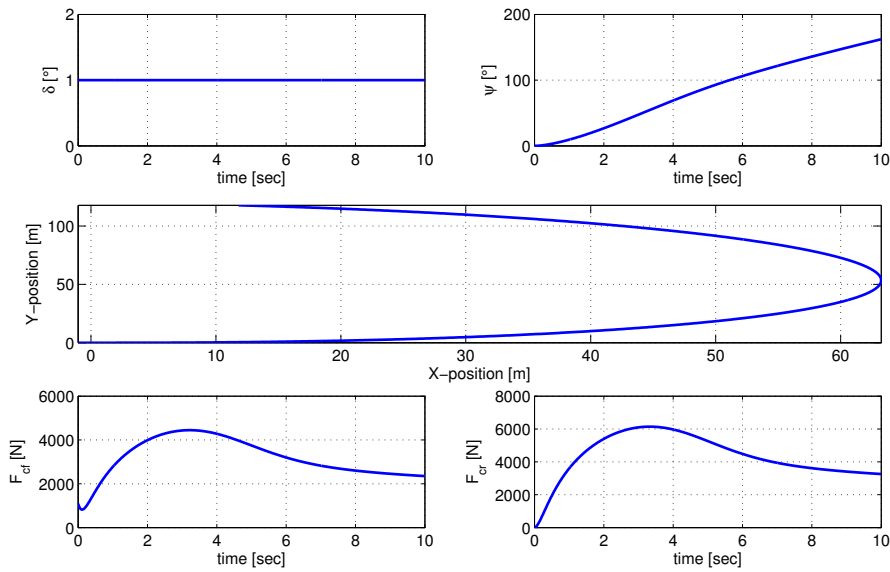


Figure 2.7: Vehicle simulation: $v_0 = 20$, $F_{lf} = 0$, $\delta = 1^\circ$.

The same left turn with an additional traction force of $F_{lf} = 500$ is shown in Fig. 2.8. It can be seen in comparison to Fig. 2.7 that the lateral forces are increased due to the increase in velocity.

The experiment in Fig. 2.9 again considers a left turn with an increase in the steering angle from 0° to 3° within 10 sec.

Fig. 2.10 considers the case of a sinusoidal steering angle signal $\delta = 1^\circ \sin(2\pi t)$.

Fig. 2.11 as well applies a sinusoidal input signal but at a negative traction force $F_{lf} = -500$ (braking). Here, the lateral forces are decreased compared to Fig. 2.10 due to the decreased velocity.

Finally, Fig. 2.12 performs a left/right turn by a change in the steering angle

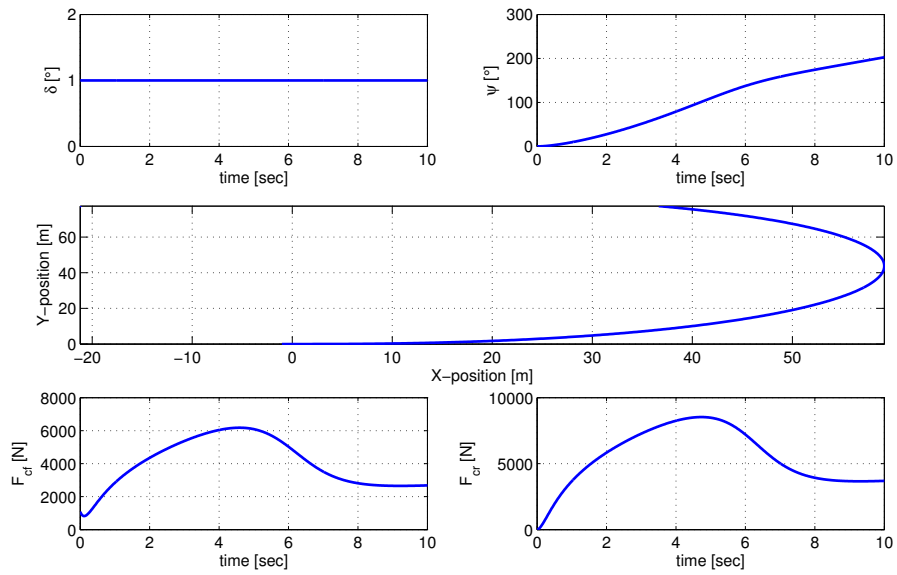


Figure 2.8: Vehicle simulation: $v_0 = 20$, $F_{lf} = 500$, $\delta = 1^\circ$.

at a higher velocity of $v_0 = 30$ m/sec.

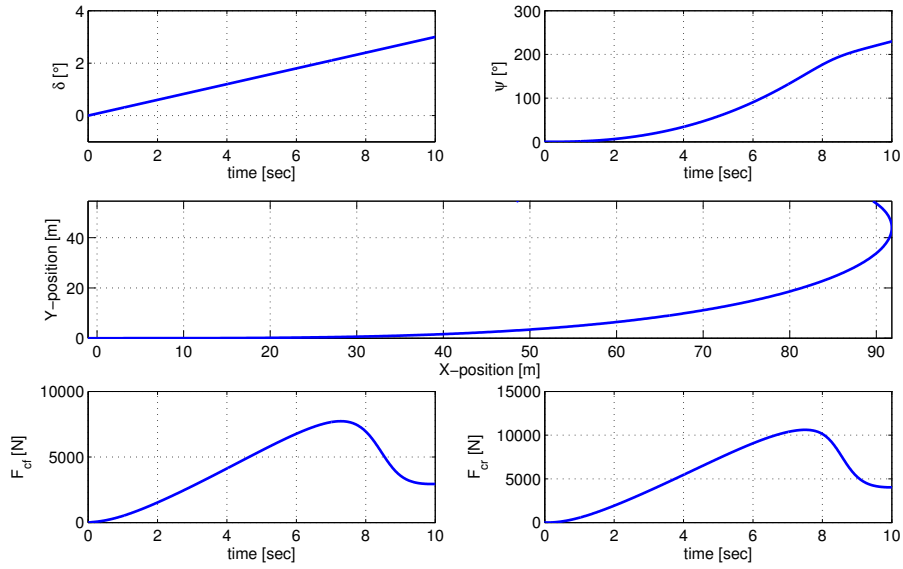


Figure 2.9: Vehicle simulation: $v_0 = 20$, $F_{lf} = 0$, $\delta = 0.3^\circ t$.

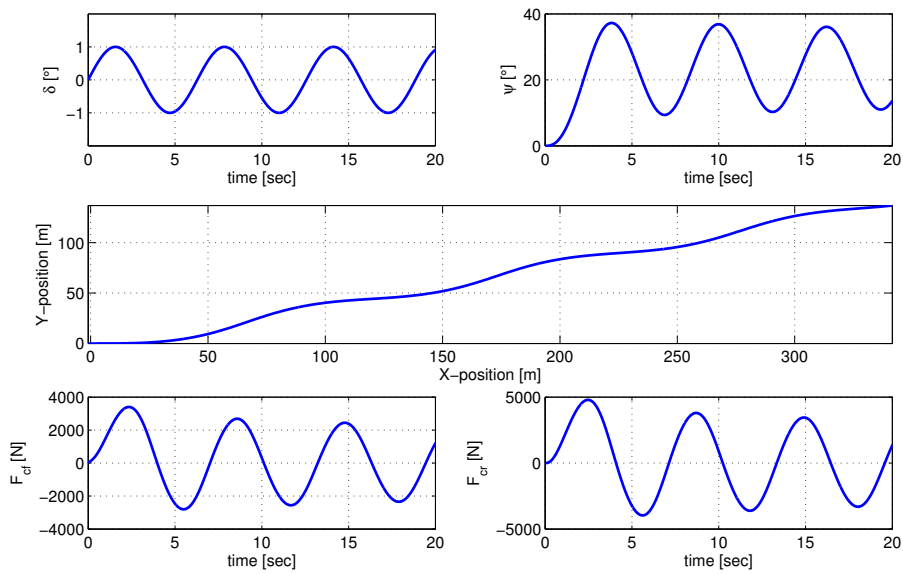


Figure 2.10: Vehicle simulation: $v_0 = 20$, $F_{lf} = 0$, $\delta = 1^\circ \sin(2\pi t)$.

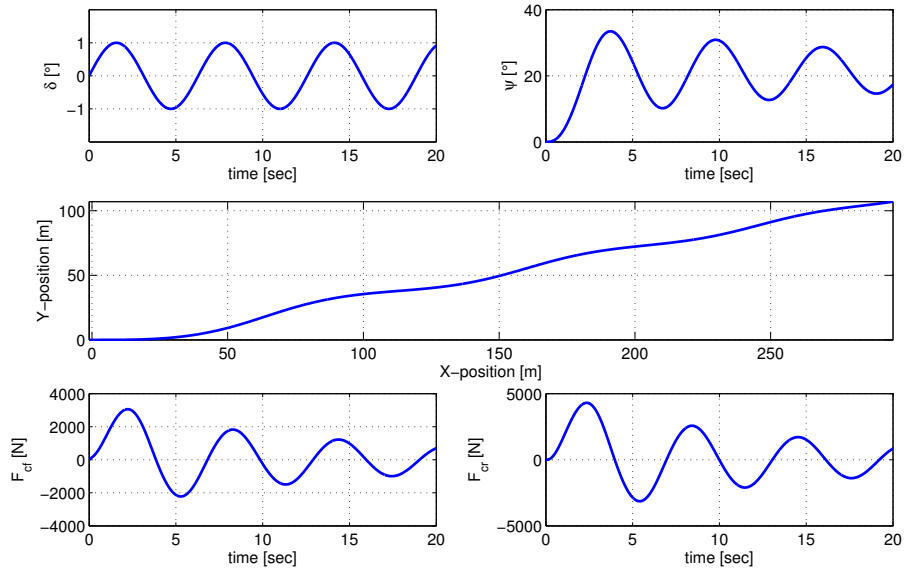


Figure 2.11: Vehicle simulation: $v_0 = 20$, $F_{lf} = -500$, $\delta = 1^\circ \sin(2\pi t)$.

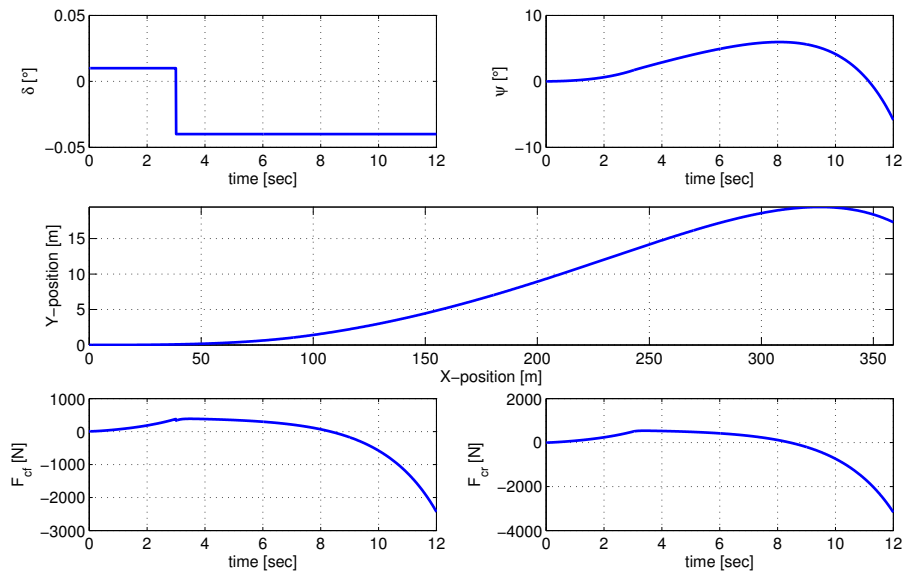


Figure 2.12: Vehicle simulation: $v_0 = 30$, $F_{lf} = 0$, $\delta = 0.01^\circ - 0.05^\circ \sigma(t - 3)$.

2.2 Clothoids Curves and Approximations

This thesis is concerned with the computation and representation of lane change trajectories for self-driving vehicles. A trajectory type that is frequently used in road construction is the clothoid curve, whose curvature changes linearly with the arc-length [31]. Since clothoid curves are also employed in this thesis, Section 2.2.1 provides a brief explanation of clothoid curves. A disadvantage of clothoid curves is the lack of an analytical representation. A possible approximation of clothoid curves in the form of arc-splines is described in Section 2.2.2.

2.2.1 Clothoid Definition

Clothoids are spiral curves as in Fig. 2.13, whose curvature $k(s)$ changes linearly with their arc-length [32, 33, 34, 35, 36].

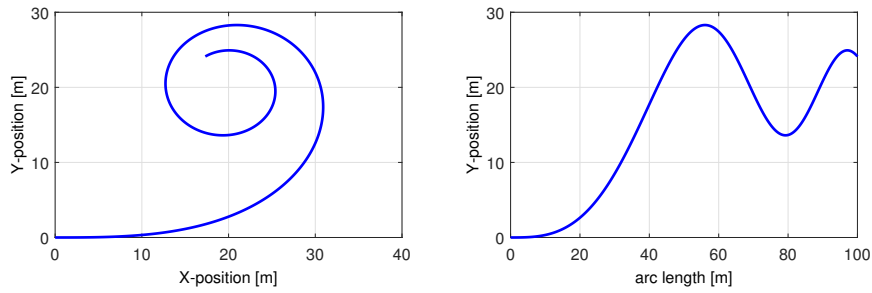


Figure 2.13: Illustration of a clothoid curve

The evolution of a clothoid in the coordinates X , Y , Ψ is evaluated depending on the arc-length parameter s :

$$\begin{aligned}\Psi(s) &= \int_0^s k(z) dz + \Psi_s \\ X(s) &= \int_0^s \cos(\Psi(z)) dz + X_s \\ Y(s) &= \int_0^s \sin(\Psi(z)) dz + Y_s\end{aligned}$$

Here, Ψ_s , X_s and Y_s represent the initial values for the tangent angle, X -position

and Y -position, respectively.

In the sequel, we employ the following notation for clothoids with arc-length S . The starting point is written as $P_s = \begin{bmatrix} X_s \\ Y_s \end{bmatrix}$, the initial curvature is $k_s = k(0)$ and the final curvature is $k_f = k(S)$. We write

$$C = \mathcal{C}(P_s, \Psi_s, k_s, k_f, S) \quad (2.28)$$

for a clothoid with starting point P_s , initial tangent angle Ψ_s , initial curvature k_s , final curvature k_f and arc-length S . We note that a clothoid is uniquely characterized by these parameters since the curvature is directly given by $k(s) = k_s + \frac{(k_f - k_s)s}{S}$. For a given clothoid $C = \mathcal{C}(P_s, \Psi_s, k_s, k_f, S)$, we introduce the notation $P_s(C) = P_s$, $\Psi_s(C) = \Psi_s$, $k_s(C) = k_s$, $k_f(C) = k_f$ and $S(C) = S$. In addition, the change in tangent angle is computed as $\Delta\Psi(C) = \frac{(k_f + k_s)S}{2}$ and the final tangent angle is $\Psi_e(C) = \Psi_s + \Delta\Psi$. We further write $Y_f(C)$ for the final y -position, whereby it has to be pointed out that there is no analytical expression for $Y_f(C)$.

In order to illustrate the properties of clothoid curves, we consider several example curves in Fig. 2.14 to 2.19. Fig. 2.14 shows a curve with $P_s = 0$, $\Psi_s = 0$, $k_s = 0$, $k_f = 0.015$ and $S = 100$. That is, the curvature increases from $k(0) = 0$ to $k(S) = 0.015$ within an arc-length of $S = 100$. The final tangent angle is $\Psi_f(C) = 0.75$ and the final y -position is $Y_f(C) = 23.99$.

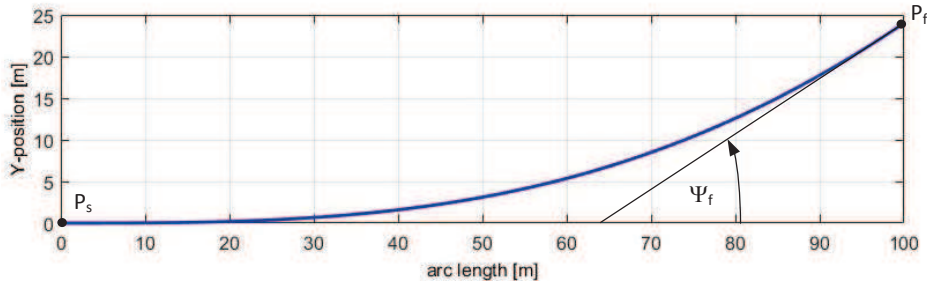


Figure 2.14: Clothoid curve $\mathcal{C}(0, 0, 0, .015, 100)$.

Fig. 2.15 shows an example $\mathcal{C}(0, 0, 0, .015, 50)$ with the same parameters except for a different arc-length of $S = 50$. It can be seen that the final tangent angle

$\Psi_f(C) = 0.375$ and the final y-position $Y_f(C) = 23.99$ are both smaller than in Fig. 2.14.

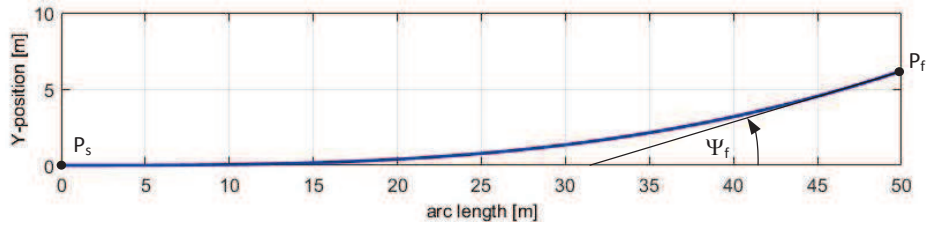


Figure 2.15: Clothoid curve $\mathcal{C}(0,0,0,.015,50)$.

The next example $\mathcal{C}(0,0.2,0,.015,100)$ considers the case where the initial tangent angle is non-zero as shown in Fig. 2.16. Since the remaining parameters are identical to the first example, it can be seen that the resulting clothoid is only rotated by Ψ_s compared to the clothoid in Fig. 2.14. The final tangent angle is $\Psi_f = 0.95$.

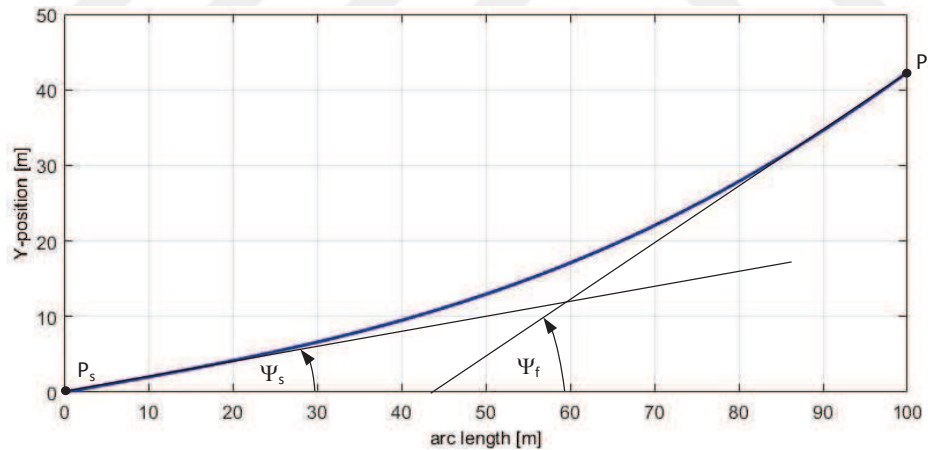


Figure 2.16: Clothoid curve $\mathcal{C}(0,0.2,0,.015,100)$.

The next example $\mathcal{C}(0,0,.005,.015,100)$ considers the case where the initial curvature is non-zero different from the first example. Fig. 2.17 shows that the resulting clothoid has a larger final tangent angle $\Psi_f = 1.0$ and a larger final y-position $Y_f = 39.1$ compared to the clothoid in Fig. 2.14.

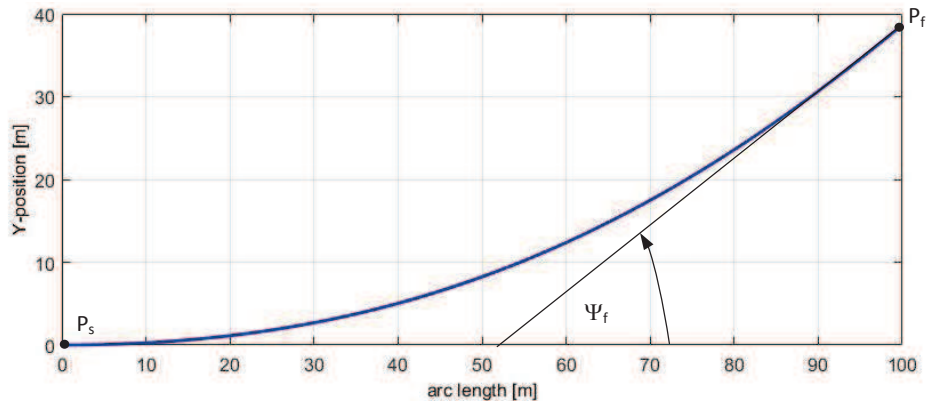


Figure 2.17: Clothoid curve $\mathcal{C}(0,0,.005,.015,100)$.

Fig. 2.18 demonstrates a clothoid $\mathcal{C}(0,0,0,-.015,100)$ with a negative final curvature $k_f = -0.015$. Since the remaining parameters are identical to the first example, it holds that this curve is symmetrical to the clothoid in Fig. 2.14 with respect to the x-axis and the final angle is $\Psi_f = -0.75$.

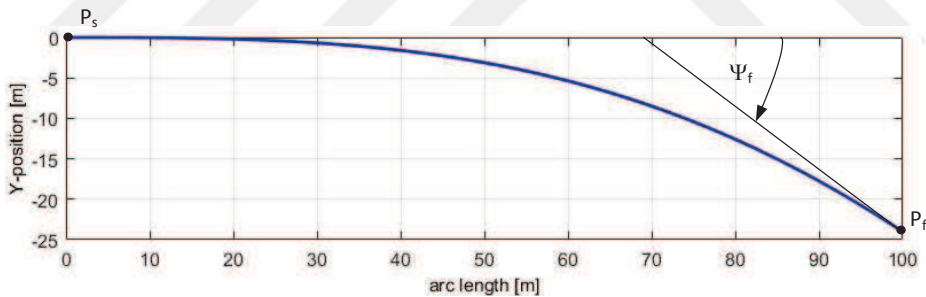


Figure 2.18: Clothoid curve $\mathcal{C}(0,0,0,-.015,100)$.

In the final example, we consider a clothoid $\mathcal{C}(0,0,0.015,0,100)$, whose curvature decreases along the arc-length. That is, the initial and final curvature values are swapped compared to the clothoid in the first example. In this case, it turns out that the final angle $\Psi_f = 0.75$ is identical, whereas the final y-position $Y_f = 47.9$ is larger compared to Fig. 2.14.

We note that all the previous clothoid examples were chosen such that the sign of the initial curvature k_s and the final curvature k_f are the same since such curves

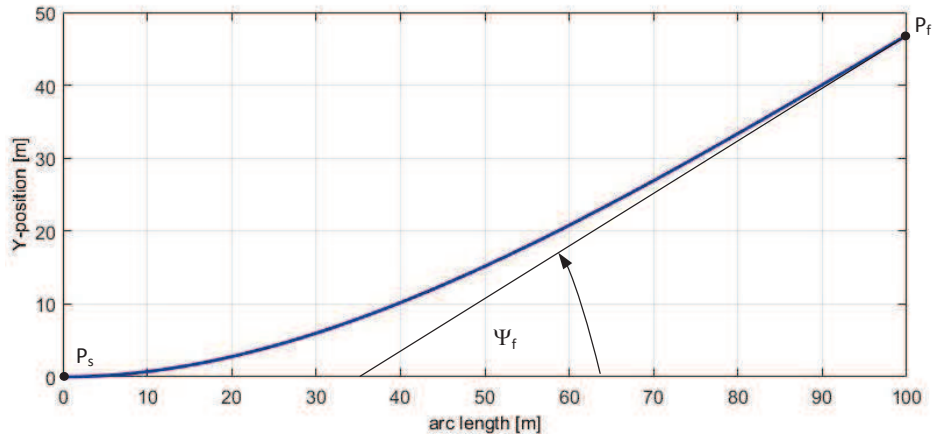


Figure 2.19: Clothoid curve $\mathcal{C}(0,0,0.015,0,100)$.

are employed in this thesis.

Clothoids are considered as suitable curves for vehicle trajectories since they enable a smooth change of the trajectory curvature [31, 37, 38]. Although clothoid trajectories generally do not fulfill the dynamic constraints of the vehicle motion as described in Section 2.1, it holds that they can be closely followed by vehicles. On the downside, clothoid curves have several disadvantages in practical applications. First, it is the case that there is no analytical representation of the X -position and Y -position of a clothoid trajectory. That is, in order to obtain all points on a clothoid, the integral equations in (2.28) have to be solved. Accordingly, it is difficult to directly compute and parametrize clothoid trajectories. It is as well not possible to characterize offset curves of a clothoid as clothoids, which is for example needed when representing parallel lanes of a road [34]. In addition, it is not straightforward to compute the distance of a point to a clothoid curve, which is highly relevant when performing trajectory tracking of vehicles.

2.2.2 Clothoid Approximation using Arc Splines

This section presents arc-splines [34] as an approximation of clothoid curves that addresses the issues expressed in the previous section. An arc-spline approximates a clothoid by concatenated arc segments. The resulting curve can be parametrized analytically and it is straightforward to determine an offset curve for each arc, which is again represented by an arc. In addition, the minimum distance of any point to an arc can be evaluated analytically.

We consider the approximation of a clothoid curve $C = \mathcal{C}(P_s, \Psi_s, k_s, k_f, S)$ as in (2.28), whereby it is assumed that the initial curvature k_s and final curvature k_f have the same sign. Then, an arc-spline with approximation order n is determined by $n + 1$ arc segments. The relevant parameters of an arc-spline are defined as follows:

- Curvature increment: $h = \frac{k_f - k_s}{n}$
- Curvature of arc j , $j = 0, \dots, n$: $k_j = k_s + jh = k_s + j \frac{k_f - k_s}{n}$
- Angle spanned by the first arc ($j = 0$): $w_0 = \frac{S k_s}{2n}$
- Angle spanned by arcs with $j = 1, \dots, n - 1$: $w_j = \frac{S k_j}{n} = \frac{k_s S}{n} + \frac{j(k_f - k_s) S}{n^2}$
- Angle spanned by the last arc ($j = n$): $w_n = \frac{S k_n}{2n} = \frac{S k_f}{2n}$
- Length of the first and last arc ($j = 0, n$): $S_0 = S_n = \frac{S}{2n}$
- Length of the remaining arcs with $j = 1, \dots, n - 1$: $S_j = \frac{S}{n}$
- Angle at the end of each arc for $j = 0, \dots, n - 1$:

$$\Psi_j = \Psi_s + \sum_{i=0}^j w_i. \quad (2.29)$$

Using the defined parameters, the arc-spline for the clothoid curve in (2.28) is parametrized as follows.

First segment ($j = 0$)

If $k_s = 0$, the first segment is a line segment from the start point P_s with the parametrization

$$P_s + s \begin{bmatrix} \cos(\Psi_s) \\ \sin(\Psi_s) \end{bmatrix}, \quad s \in [0, \frac{S}{2n}]. \quad (2.30)$$

and the end point

$$P_0 = P_s + \frac{S}{2n} \begin{bmatrix} \cos(\Psi_s) \\ \sin(\Psi_s) \end{bmatrix}. \quad (2.31)$$

We write $L = \mathcal{L}(P_s, \Psi_s, S_L)$ for a line segment with starting point P_s , initial orientation Ψ_s and length S_L . That is, the line segment described by (2.30) and (2.31) is written as $\mathcal{L}(P_s, \Psi_s, \frac{S}{2n})$.

If $k_s \neq 0$, the first segment is an arc segment with radius $R_0 = 1/k_s$ and center $C_0 = P_s + R_0 \begin{bmatrix} -\sin(\Psi_s) \\ \cos(\Psi_s) \end{bmatrix}$ from the tangent angle Ψ_s to the tangent angle $\Psi_0 = \Psi_s + w_0 = \Psi_s + \frac{Sk_s}{2n}$. The parametrization is

$$P_s + R_0 \begin{bmatrix} \sin(\theta) - \sin(\Psi_s) \\ \cos(\Psi_s) - \cos(\theta) \end{bmatrix}, \quad \theta \in [\Psi_s, \Psi_0] \quad (2.32)$$

and the end point is

$$P_0 = P_s + R_0 \begin{bmatrix} \sin(\Psi_0) - \sin(\Psi_s) \\ \cos(\Psi_s) - \cos(\Psi_0) \end{bmatrix}. \quad (2.33)$$

Considering that an arc segment is uniquely determined by the starting point P_s , the initial orientation angle Ψ_s , the radius R_A and the arc-length S_A , we write $A = \mathcal{A}(P_s, \Psi_s, R_A, S_A)$ for a general arc segment. The arc segment represented by (2.32) and (2.33) is hence written as $\mathcal{A}(P_s, \Psi_s, R_0, R_0(\Psi_0 - \Psi_s))$.

Segment 1 to $n - 1$

These segments are always represented by arc segments with the respective radius $R_j = 1/k_j$, $j = 1, \dots, n-1$. The center point is $C_j = P_{j-1} + R_j \begin{bmatrix} -\sin(\Psi_{j-1}) \\ \cos(\Psi_{j-1}) \end{bmatrix}$, the parametrization is

$$C_j + R_j \begin{bmatrix} \sin(\theta) \\ -\cos(\theta) \end{bmatrix} = P_{j-1} + R_j \begin{bmatrix} \sin(\theta) - \sin(\Psi_{j-1}) \\ \cos(\Psi_{j-1}) - \cos(\theta) \end{bmatrix}, \quad \theta \in [\Psi_{j-1}, \Psi_j]. \quad (2.34)$$

and the end point evaluates as

$$P_j = C_j + R_j \begin{bmatrix} \sin(\Psi_j) \\ -\cos(\Psi_j) \end{bmatrix} = P_{j-1} + R_j \begin{bmatrix} \sin(\Psi_j) - \sin(\Psi_{j-1}) \\ \cos(\Psi_{j-1}) - \cos(\Psi_j) \end{bmatrix}. \quad (2.35)$$

These arc segments are written as $A_j = \mathcal{A}(P_{j-1}, \Psi_{j-1}, R_j, \frac{S}{n})$.

Last segment ($j = n$)

The type of the last segment depends on the final curvature k_f . If $k_f = 0$, the last segment is a line segment $L_n = \mathcal{L}(P_{n-1}, \Psi_{n-1}, \frac{S}{2n})$ from point P_{n-1} with the parametrization

$$P_{n-1} + s \begin{bmatrix} \cos(\Psi_{n-1}) \\ \sin(\Psi_{n-1}) \end{bmatrix}, \quad s \in [0, \frac{S}{2n}]. \quad (2.36)$$

and the end point

$$P_n = P_{n-1} + \frac{S}{2n} \begin{bmatrix} \cos(\Psi_{n-1}) \\ \sin(\Psi_{n-1}) \end{bmatrix}. \quad (2.37)$$

If $k_f \neq 0$, the last segment is an arc segment with radius $R_n = 1/k_f$ and center $C_{n-1} = P_{n-1} + R_n \begin{bmatrix} -\sin(\Psi_{n-1}) \\ \cos(\Psi_{n-1}) \end{bmatrix}$ from angle Ψ_{n-1} to angle Ψ_n . The resulting

parametrization is

$$C_n + R_n \begin{bmatrix} \sin(\theta) \\ -\cos(\theta) \end{bmatrix} = P_{n-1} + R_n \begin{bmatrix} \sin(\theta) - \sin(\Psi_{n-1}) \\ \cos(\Psi_{n-1}) - \cos(\theta) \end{bmatrix}, \quad \theta \in [\Psi_{n-1}, \Psi_n]. \quad (2.38)$$

and the end point is

$$P_n = C_n + R_n \begin{bmatrix} \sin(\Psi_n) \\ -\cos(\Psi_n) \end{bmatrix} = P_{n-1} + R_n \begin{bmatrix} \sin(\Psi_n) - \sin(\Psi_{n-1}) \\ \cos(\Psi_{n-1}) - \cos(\Psi_n) \end{bmatrix}. \quad (2.39)$$

This arc segment is written as $A_n = \mathcal{A}(P_{n-1}, \Psi_{n-1}, R_n, \frac{S}{2n})$.

It is interesting to note that the change of tangent angle $\Delta\theta = \frac{(k_f + k_s)S}{2}$ is identical to that of the corresponding clothoid curve. We write $\hat{\mathcal{C}}(P_s, \Psi_s, k_s, k_f, S, n)$ for the approximation of the clothoid curve $\mathcal{C}(P_s, \Psi_s, k_s, k_f, S)$ with approximation order n .

Examples for arc-splines with $n = 5$ are given in Fig. 2.20 and 2.21. $\hat{\mathcal{C}}(0, 0, 0, 1.2, 5, 5)$ in Fig. 2.20 has $k_s = 0$ such that the first segment is a line segment. The remaining segments are arc segments with linearly increasing curvature. Accordingly, the radius of successive arc segments is decreasing.

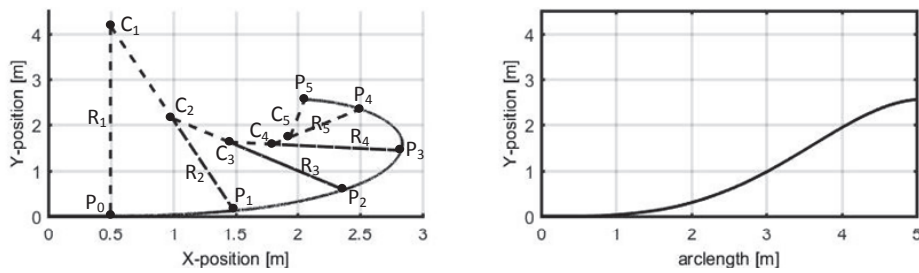


Figure 2.20: Arc spline $\hat{\mathcal{C}}(0, 0, 0, 1.2, 5, 5)$.

$\hat{\mathcal{C}}(0, 0, 0.3, 1.2, 5, 5)$ in Fig. 2.21 has $k_s > 0$ and $k_f > 0$ such that all segments are arc segments.

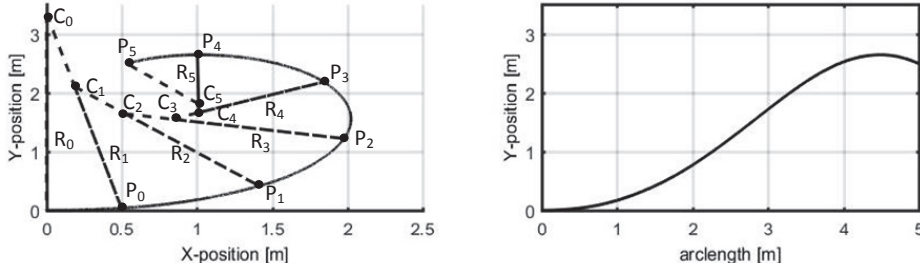


Figure 2.21: Clothoid curve $\mathcal{C}(0, 0, 0.3, 1.2, 5, 5)$.

In the scope of this thesis, it is important to note that the approximation accuracy of arc-splines can be adjusted by the approximation order n . In particular, the following result from [34] ensures that the approximation accuracy increases quadratically with the approximation order.

Proposition 1. $\mathcal{C}(P_s, \Psi_s, k_s, k_f, S, n)$. Consider a clothoid curve $C = \mathcal{C}(P_s, \Psi_s, k_s, k_f, S)$ and its arc-spline approximation $\hat{C} = \mathcal{C}(P_s, \Psi_s, k_s, k_f, S, n)$ with approximation order n . Write $P(s)$ for the point of C at arc-length s and $\hat{P}(s, n)$ for the point of \hat{C} at arc-length s for approximation order n . Then, it holds that

$$\max_{0 \leq s \leq S} \|P(s) - \hat{P}(s, n)\| = \mathcal{O}(1/n^2). \quad (2.40)$$

The increased approximation accuracy is illustrated in the following figures. the clothoid curve $\mathcal{C}(0, 0, 0, 0.015, 100)$ and its arc-spline approximation $\mathcal{C}(0, 0, 0, 0.015, 100, 5)$ is shown in Fig. 2.22, whereas Fig. 2.23 shows the same clothoid curve and its arc-spline approximation $\mathcal{C}(0, 0, 0, 0.015, 100, 10)$. It can be readily seen that the approximation error is significantly reduced when choosing a higher approximation order.

In summary, this section considers clothoid curves that are suitable for representing road segments and their arc-spline approximations. Clothoids are curves, whose curvature changes linearly with the arc-length, whereas arc-splines consist of circular segments, whose curvature changes linearly along the arc segments. The advantage of arc-splines is that they can be parametrized analytically, which is not possible for clothoids. In addition, it holds that the approximation accuracy

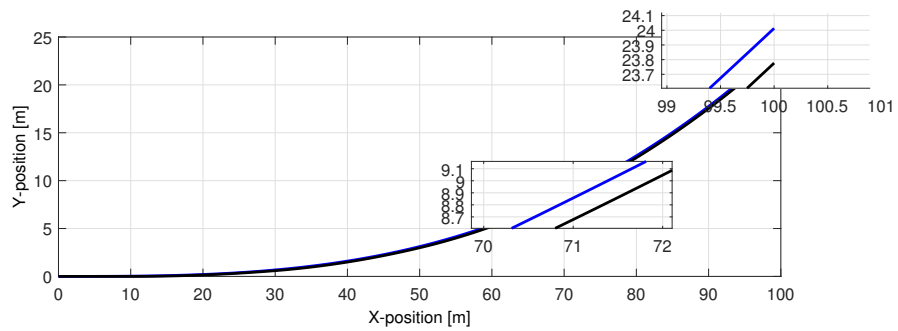


Figure 2.22: Comparison of $\mathcal{C}(0,0,0,0.015,100)$ and $\hat{\mathcal{C}}(0,0,0,0.015,100,5)$.

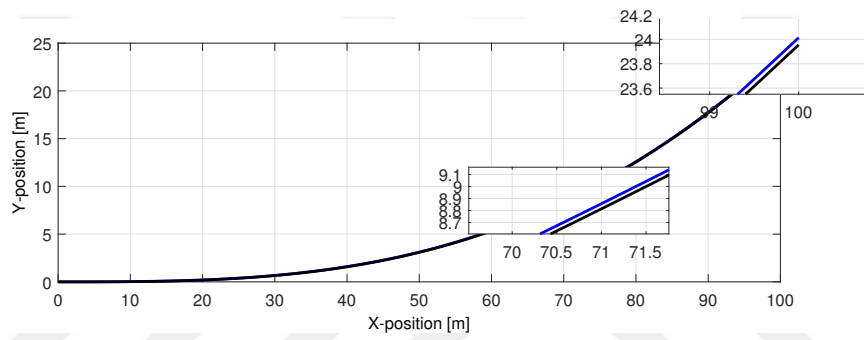


Figure 2.23: Comparison of $\mathcal{C}(0,0,0,0.015,100)$ and $\hat{\mathcal{C}}(0,0,0,0.015,100,10)$.

of arc-splines can be increased by choosing a sufficient number of arc segments (approximation order). When using arc-splines for vehicle trajectories, it has to be taken into account that there are small jumps in the curvature that cannot be perfectly followed by vehicles.

CHAPTER 3

Optimal Control Computations for Lane Changes

As the first main contribution of this thesis, this chapter is concerned with the the computation of lane change trajectories for self-driving vehicles. To this end, Section 3.1 summarizes some related work on this subject. Section 3.2 develops the problem formulation in the form of an optimal control problem. Section 3.3 and 3.4 present solutions of this optimal control problem using collocation and a gradient-based method, respectively. A discussion and comparison of the obtained results is given in Section 3.5.

3.1 Basic Setting and Related Work

Lane changing is the process, where a vehicle moves from its current lane to an adjacent lane as depicted in Fig. 3.1.

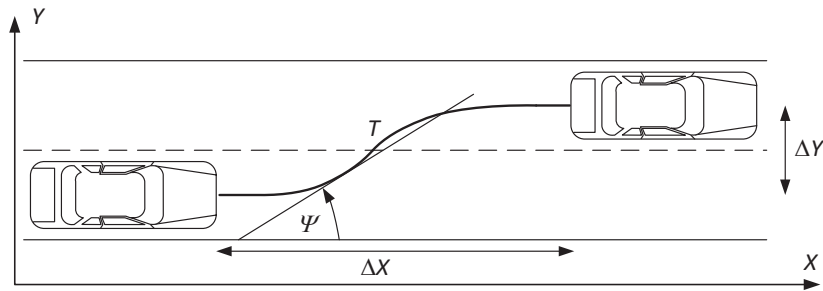


Figure 3.1: Basic lane change maneuver.

A lane change is carried out following a certain trajectory T in the coordinate plane (X - Y -plane). Hereby, the change in the Y -position is given by the lane width ΔY , whereas the change in the X -position and the orientation angle Ψ during

the lane change determine the particular shape of T . In principle, a trajectory T with a small value of ΔX requires a fast change of the orientation angle Ψ and is hence difficult to follow when vehicles travel at high velocities or perform acceleration maneuvers. In turn, trajectories T with large values of ΔX permit small variations of Ψ and are suitable for fast vehicles. The disadvantage of such trajectories is given by the fact that vehicles simultaneously occupy two lanes of a larger segment of the road, leading to an inefficient use of the road infrastructure. Accordingly, it is highly relevant to adjust lane change trajectories T depending on the velocity/acceleration profile of vehicles.

Lane changing maneuvers influence the safety and throughput of a transportation system. A single lane changing vehicle affects the behavior of all the surrounding vehicles in its current and target lanes [9][39]. It was shown in the literature that lane-changing maneuver due to lane drop generates congestion [40]. Furthermore, one tenth of accidents are caused by lane changes [41]. Hence, a lane change should be performed in a safe and efficient way avoiding extreme maneuvers which can impair safety and traffic throughput.

When investigating lane changes, two basic problems are studied in the literature.

1. From the traffic control perspective, it is necessary to analyze the decision process of when to perform a lane change and its effect on the traffic flow.
2. From the automatic control perspective, it is important to plan suitable trajectories for lane changes depending on the driving situation and to precisely follow these trajectories by generating input signals for the vehicle in order to ensure driving safety and comfort.

Regarding item 1. the survey article [10] gives a detailed review of existing lane changing models for the traffic flow analysis, indicating their advantages and disadvantages. The authors classify the lane changing models as models based on search algorithms (search algorithms from computer science are utilized for finding future positions of vehicles) and models based on traffic characteristics.

Examples of lane changing models based on search algorithms are [42, 43].

PRediction In Dynamic Environment (PRIDE) [42] uses short term and long term prediction algorithms in order to determine the actual vehicle behavior. A cost is assigned to each of future action (acceleration/deceleration, lane changing) and the total cost is used for determining the set of possible future positions and corresponding probability that a vehicle is going to be in that position. The next position of a vehicle is chosen according to calculated probabilities and computed distances between positions. A lane changing model based on a forward search algorithm is given in [43]. Here, a branching tree of sequential actions for each modeled vehicle is constructed when a sufficient gap between vehicles is available in the target adjacent lane. The sequence of actions requiring minimum travel time is selected and applied by the driver.

Examples of lane changing models based on traffic characteristics are given in [44, 45, 46, 47, 8, 48]. Gipps's model in [44] is based on the physical possibility, safety, necessity and desirability of lane change. Another factor affecting the drivers decision to change a lane is the distance between the current position and the intended exit point. Lane changing is possible if there is sufficient gap and the maneuver is guaranteed to be safe. Wiedemann and Reiter proposed a lane changing model based on the desire to drive faster or slower. In this model, some lanes are for fast drivers, some of them are for slow ones. The lane changing depends on the difference between the front vehicle speed and subject vehicle's desired speed [45]. Hidas' model suggests to classify lane changes as free, forced, and cooperative. In a free lane change, the distance between leader and following vehicles in the target lane does not change. In a forced lane change, it first decreases before the maneuver and increases after the maneuver is completed. In a cooperative lane change, it increases before the maneuver and then decreases [46, 47]. Recently the Lane Change Model with Relaxation and Synchronization (LMRS) was introduced in [8]. Here, relaxation is a phenomenon of driver's application of small deceleration and acceptance of different time headways. Synchronization means alignment with a gap prepared by vehicles in an adjacent lane. Free, synchronized, and cooperative lane changes are realized. Another lane change model considering the car-following behavior is presented in [48]. This model mainly

focuses on an accelerated lane change with regard to the kinematic behavior of the subject vehicle.

It has to be noted that the vehicle models used in the described studies are abstracted from the actual vehicle dynamics and rather optimized for the simulation/analysis of the traffic flow. That is, the problem of trajectory generation and trajectory following is not considered in these studies.

There are several research works regarding item 2. A lane change model for self-driving vehicles was presented in [49]. In this study the emphasis was made on generating a safe path (based on piecewise Bezier curve). The resulting work was tested on a real self-driving vehicle. Model predictive control (MPC) is used in lane change steering maneuver in [50]. Constraints are formulated for finding a trajectory and suitable input signals, while avoiding collisions. The paper also contains a study on lane changing maneuvers for collision avoidance. [51] presents and utilizes an optimal-control based method for quantifying the maneuverability of actively controlled passenger vehicles during emergency highway-speed situations. The research is motivated by the desire to better understand the performance benefits of additional actuated degrees of freedom such as rear steering when compared to a typical vehicle. The emergency maneuvers considered are obstacle avoidance, barrier avoidance and lane changes. Necessary conditions for optimality and optimal control laws are found for each case. Solutions are found using a lumped-parameter planar single-track vehicle model and nonlinear tire dynamics are assumed. [11] provide optimal control-based strategies to explore the dynamic capabilities of a single-track car model that includes tire models and longitudinal load transfer. The paper explores the system dynamics by the use of nonlinear optimal control techniques to compute aggressive car trajectories. An optimal path-planning method is proposed for self-driving ground vehicles in case of overtaking a moving obstacle in [52]. The path for the overtaking maneuver is generated by a two-phase optimal path-planning problem. On the one hand, the vehicle approaches the obstacle as close as possible. On the other hand, tight following of a reference path and constraints on the lateral acceleration of the vehicle are imposed. The trajectory generation problem faced by an self-driving

vehicle in moving traffic is investigated in [14]. A semi-reactive planning strategy is proposed. It realizes long-term maneuvers and ensures short-term collision avoidance.

The problem in item 2. is the main subject of this thesis. That is, we focus on the generation of suitable lane change trajectories T_d depending on the driving situation which is described by the velocity/acceleration profile of vehicles. In the following, we develop optimal control formulations in order to compute trajectories and input signals for lane changes. Different from the previous studies, the formulation in this thesis includes variations in the longitudinal vehicle motion and uses a specific model for decoupling the longitudinal motion from the lateral vehicle motion as described in the sequel.

3.2 Lane Change Formulation

Our study is based on the dynamic vehicle models in Section 2.1. In the sequel, we develop optimal control formulations based on these models.

3.2.1 Decoupling The Longitudinal and Lateral Motion

As the first contribution of the thesis, we note that the longitudinal and lateral dynamics are coupled when using the models in Section 2.1. That is, a change in the lateral motion via the longitudinal input force F_{lf} has an effect on the lateral motion and a change in the steering angle δ also has an effect on the longitudinal motion.

We next propose a modification of F_{lf} in order to decouple the longitudinal motion from lateral maneuvers. To this end, we define the arc-length q as the

traveled distance of the CG and the acceleration a of the CG as

$$\dot{q} = v \quad (3.1)$$

$$\begin{aligned} a = \dot{v} &= \frac{d}{dt} \sqrt{\dot{x}^2 + \dot{y}^2} = \frac{1}{2\sqrt{\dot{x}^2 + \dot{y}^2}} (2\dot{x}\ddot{x} + 2\dot{y}\ddot{y}) = \frac{\dot{x}}{v}\ddot{x} + \frac{\dot{y}}{v}\ddot{y} = \cos(\beta)\ddot{x} + \sin(\beta)\ddot{y} \\ &= \cos(\beta) \frac{F_{lf}\cos(\delta) - F_{cf}\sin(\delta)}{m} + \sin(\beta) \frac{F_{lf}\sin(\delta) + F_{cf}\cos(\delta) + F_{cr}}{m}. \end{aligned} \quad (3.2)$$

Solving for F_{lf} and writing a_r for the reference value of the acceleration, we obtain

$$F_{lf} = \frac{ma_r - F_{cf}(\cos(\delta)\sin(\beta) - \sin(\delta)\cos(\beta)) - F_{cr}\sin(\beta)}{\cos(\delta)\cos(\beta) + \sin(\delta)\sin(\beta)}. \quad (3.3)$$

That is, F_{lf} represents the required traction force to achieve a desired acceleration a_r of the CG even during turning maneuvers ($\delta \neq 0$). Using (3.3), the longitudinal motion in terms of the motion of the CG is decoupled from the lateral vehicle dynamics. In particular, the longitudinal vehicle model is now given by

$$\ddot{q} = a_r, \quad (3.4)$$

We next discuss several requirements when realizing the traction force according to (3.3). First, we note that measurements or estimates of the signals δ , β and F_{cf} are available in advanced vehicle applications. The steering angle δ can be directly measured. Furthermore, the sideslip angle $\beta = \tan^{-1}(\dot{y}/\dot{x})$ can either be estimated directly using recent methods such as [53, 54] or computed using estimations or measurements of the velocities \dot{x} and \dot{y} from inertial measurement units and differential GPS [55, 56]. Similar, existing estimation methods such as [57, 58] can be used for estimating the lateral tire forces F_{cf} and F_{cr} .

Second, we consider that the computed traction force F_{lf} in (3.3) has to be realized by applying torque to the actuated wheels of the vehicle. This task is achieved by recent methods for traction force tracking [56].

Decoupled Model in Global Coordinates

Substituting (3.4) in the model in Section 2.1.2, we obtain the following model including feedback of the force F_{lf} .

$$\ddot{X} = \frac{ma_r v \cos(\Psi + \delta) - F_{cf} \dot{Y} - F_{cr} \dot{Y} \cos(\delta)}{m(\dot{X} \cos(\Psi + \delta) + \dot{Y} \sin(\Psi + \delta))} \quad (3.5)$$

$$\ddot{Y} = \frac{ma_r v \sin(\Psi + \delta) + F_{cf} \dot{X} + F_{cr} \dot{X} \cos(\delta)}{m(\dot{X} \cos(\Psi + \delta) + \dot{Y} \sin(\Psi + \delta))} \quad (3.6)$$

$$\ddot{\Psi} = -\frac{F_{cr} b}{I_{zz}} + \frac{a(ma_r v \sin(\delta) + F_{cf}(\dot{X} \cos(\Psi) + \dot{Y} \sin(\Psi)))}{I_{zz}(\dot{X} \cos(\Psi + \delta) + \dot{Y} \sin(\Psi + \delta))} \quad (3.7)$$

$$+ \frac{aF_{cr}(\dot{X} \sin(\Psi) \sin(\delta) - \dot{Y} \cos(\Psi) \sin(\delta))}{I_{zz}(\dot{X} \cos(\Psi + \delta) + \dot{Y} \sin(\Psi + \delta))}. \quad (3.8)$$

Decoupled Model using the Slip Angle

Substituting (3.3) into the model in Section 2.1.3, the model based on the slip angle is

$$\dot{\beta} = \frac{\cos(\beta)}{mv} (F_{cr} + F_{cf} \cos(\delta) + \frac{ma_r - F_{cf} \sin(\beta - \delta)}{\cos(\beta - \delta)}) - \dot{\Psi} \cos^2(\beta), \quad (3.9)$$

$$\ddot{\Psi} = \frac{a(ma_r + F_{cf} \cos(\beta) - F_{cr} \sin(\beta) \sin(\delta)) - bF_{cr} \cos(\beta - \delta)}{I_{zz} \cos(\beta - \delta)}, \quad (3.10)$$

$$\dot{X} = v \cos(\Psi + \beta) \quad (3.11)$$

$$\dot{Y} = v \sin(\Psi + \beta). \quad (3.12)$$

3.2.2 Transformation of the Decoupled Model to Arc-length Coordinates

The models established previously are formulated using differential equations in time. Nevertheless, when using lane change trajectories, it proves useful to represent these trajectories depending on the traveled distance on the road, denoted as arc-length s . We next transform the previous models to a representation in the arc-length coordinate s . To this end, we first provide several basic substitutions. In addition, we denote the derivative with respect to the arc-length by \bullet' .

$$\dot{X} = \frac{dX}{dt} = \frac{dX}{ds} \cdot \frac{ds}{dt} = X' \cdot \dot{s} \quad (3.13)$$

$$\dot{Y} = \frac{dY}{dt} = \frac{dY}{ds} \cdot \frac{ds}{dt} = Y' \cdot \dot{s} \quad (3.14)$$

$$\dot{\Psi} = \frac{d\Psi}{dt} = \frac{d\Psi}{ds} \cdot \frac{ds}{dt} = \Psi' \cdot \dot{s} \quad (3.15)$$

$$\ddot{X} = \frac{d}{dt}\dot{X} = \frac{d}{dt}X' \cdot \dot{s} = X'' \cdot \dot{s}^2 + X' \cdot \ddot{s} \quad (3.16)$$

$$\ddot{Y} = Y'' \cdot \dot{s}^2 + Y' \cdot \ddot{s} \quad (3.17)$$

$$\ddot{\Psi} = \Psi'' \cdot \dot{s}^2 + \Psi' \cdot \ddot{s} \quad (3.18)$$

$$\dot{\beta} = \frac{d\beta}{dt} = \frac{d\beta}{ds} \cdot \frac{ds}{dt} = \beta' \cdot \dot{s}. \quad (3.19)$$

Decoupled Model in Global Arc-length Coordinates

Using the above relations, the model in the global coordinates can be transformed to the arc-length representation. Note that $\dot{s} = v$ and $\ddot{s} = a_r$ are used.

$$X'' \cdot v^2 + X' \cdot a_r = \frac{ma_r v \cos(\Psi + \delta) - F_{cf} Y' v - F_{cr} Y' v \cos(\delta)}{m(X' v \cos(\Psi + \delta) + Y' v \sin(\Psi + \delta))} \quad (3.20)$$

$$Y'' \cdot v^2 + Y' \cdot a_r = \frac{ma_r v \sin(\Psi + \delta) + F_{cf} X' v + F_{cr} X' v \cos(\delta)}{m(X' v \cos(\Psi + \delta) + Y' v \sin(\Psi + \delta))} \quad (3.21)$$

$$\Psi'' \cdot v^2 + \Psi' \cdot a_r = -\frac{F_{cr} b}{I_{zz}} + \frac{a(ma_r v \sin(\delta) + F_{cf}(X' v \cos(\Psi) + Y' v \sin(\Psi)))}{I_{zz}(X' v \cos(\Psi + \delta) + Y' v \sin(\Psi + \delta))} \quad (3.22)$$

$$+ \frac{aF_{cr}(X' v \sin(\Psi) \sin(\delta) - Y' v \cos(\Psi) \sin(\delta))}{I_{zz}(X' v \cos(\Psi + \delta) + Y' v \sin(\Psi + \delta))}. \quad (3.23)$$

Decoupled Model in Slip Angle Arc-length Coordinates

Similarly, the model based on the slip angle is formulated in the arc-length coordinates on (3.24) to (3.27).

$$\beta' \cdot v = \frac{\cos(\beta)}{mv} (F_{cr} + F_{cf} \cos(\delta) + \frac{ma_r - F_{cf} \sin(\beta - \delta)}{\cos(\beta - \delta)}) - \Psi' v \cos^2(\beta), \quad (3.24)$$

$$\Psi'' \cdot v^2 + \Psi' \cdot a_r = \frac{a(ma_r + F_{cf} \cos(\beta) - F_{cr} \sin(\beta) \sin(\delta)) - b F_{cr} \cos(\beta - \delta)}{I_{zz} \cos(\beta - \delta)}, \quad (3.25)$$

$$X' = \cos(\Psi + \beta) \quad (3.26)$$

$$Y' = \sin(\Psi + \beta). \quad (3.27)$$

3.2.3 Optimal Control Problem Formulation

The main task of this chapter is the formulation and solution of optimal control problems for lane changes based on the models in the previous section. The optimal control problem to be solved is written as

$$\min_{\delta(s)} \left\{ \int_0^S \delta^2(s) ds \right\} \quad (3.28)$$

subject to the dynamic equations of the respective model in Section 3.2.2 and the constraints

$$(3.29)$$

$$Y_{\min} \leq Y(s) \leq Y_{\max}, \quad ppY_{\min} \leq Y''(s) \leq ppY_{\max}, \quad (3.30)$$

$$\Psi_{\min} \leq \Psi(s) \leq \Psi_{\max}, \quad pp\Psi_{\min} \leq \Psi''(s) \leq pp\Psi_{\max}, \quad (3.31)$$

$$\delta_{\min} \leq \delta(s) \leq \delta_{\max}, \quad p\delta_{\min} \leq \delta'(s) \leq p\delta_{\max}, \quad (3.32)$$

$$\dot{s}(0) = v, \quad \ddot{s}(0) = 0 \quad (3.33)$$

$$X(0) = 0, \quad X'(0) = 1, \quad X''(0) = 0, \quad Y(0) = 0, \quad Y'(0) = 0, \quad Y''(0) = 0, \quad (3.34)$$

$$\beta(0) = 0, \quad \beta'(0) = 0, \quad \beta''(0) = 0, \quad \Psi(0) = 0, \quad \Psi'(0) = 0, \quad \Psi''(0) = 0, \quad (3.35)$$

$$X'(S) = 1, \quad X''(S) = 0, \quad Y(S) = \Delta Y, \quad Y'(S) = 0, \quad Y''(S) = 0, \quad (3.36)$$

$$\beta(S) = 0, \quad \beta'(S) = 0, \quad \beta''(S) = 0, \quad \Psi(S) = 0, \quad \Psi'(S) = 0, \quad \Psi''(S) = 0, \quad (3.37)$$

That is, the objective is to minimize the accumulated steering angle. In addition, constraints on Y , Ψ , δ are given by (3.30) to (3.32) and initial and final conditions are formulated in (3.33) to (3.37). The conditions in (3.30) state that the lateral (Y -)position and lateral acceleration should remain between the given bounds. This is necessary in order to ensure that the computed lane change trajectory as in Fig. 3.1 is computed between the respective lanes and without entering other lanes. In addition, it is preferred to avoid large lateral accelerations. A similar constraint is given for the orientation angle Ψ and the corresponding rotational acceleration in (3.31). The steering angle and its derivative are bounded in 3.32, which captures physical limitations of the steering system. Initially ($s = 0$), it is assumed that the vehicle moves along the X -axis with a constant velocity v as specified in 3.33 to 3.35. At the end of the maneuver ($s = S$ in (3.36) and (3.37)), the driving direction is again the X -axis. Nevertheless, the Y -position is now ΔY ,

which describes the lane change width.

3.3 Collocation Method

3.3.1 Parameters of Our Collocation Method

In order to realize an optimal control solver with direct collocation, we use the model in the global coordinates X, Y, Ψ in Section 3.2.2. We recall that the slip angles formulated in the global coordinates are

$$\alpha_f = \tan^{-1}\left(\frac{-X' \sin(\Psi) + Y' \cos(\Psi) + a \Psi'}{X' \cos(\Psi) + Y' \sin(\Psi)}\right) - \delta \quad (3.38)$$

$$\alpha_r = \tan^{-1}\left(\frac{-X' \sin(\Psi) + Y' \cos(\Psi) - b \dot{\Psi}}{X' \cos(\Psi) + Y' \sin(\Psi)}\right) \quad (3.39)$$

In order to apply direct collocation, the arc-length is divided into N collocation intervals with $N + 1$ equidistant collocation points: $s_k = k \cdot h$ with the step size h and $k = 0, \dots, N$.

We use cubic interpolation polynomials for representing the Y -position, the orientation angle Ψ and the steering angle δ . We further assume that the longitudinal speed v and acceleration a_t are known. Hence, it holds for $k = 0, \dots, N$ and for $s_k \leq t < t_{k+1}$

$$Y^k(s) = a_0^k + a_1^k(s - s_k) + a_2^k(s - s_k)^2 + a_3^k(s - s_k)^3$$

$$\Psi^k(s) = b_0^k + b_1^k(s - s_k) + b_2^k(s - s_k)^2 + b_3^k(s - s_k)^3$$

$$\delta^k(s) = c_0^k + c_1^k(s - s_k) + c_2^k(s - s_k)^2 + c_3^k(s - s_k)^3$$

$$X^k(s) = d_0^k + d_1^k(s - s_k) + d_2^k(s - s_k)^2 + d_3^k(s - s_k)^3$$

Hereby, it is necessary to respect the initial conditions and final conditions for the state variables and their derivatives in (3.33) to (3.37). In the considered lane change scenario, it is desired that all initial and terminal conditions evaluate to zero. Only the final Y -position is determined as $Y(S) = \Delta Y$ (lane width) such that the vehicle moves to the neighboring lane at $Y(S) = \Delta Y$. For the initial and finite

points, this means that

$$a_0^0 = 0 \quad (3.40)$$

$$b_0^0 = 0 \quad (3.41)$$

$$c_0^0 = 0 \quad (3.42)$$

$$d_0^0 = 0 \quad (3.43)$$

$$a_0^N + a_1^N h + a_2^N h^2 + a_3^N h^3 = \Delta Y \quad (3.44)$$

$$b_0^N + b_1^N h + b_2^N h^2 + b_3^N h^3 = 0 \quad (3.45)$$

$$c_0^N + c_1^N h + c_2^N h^2 + c_3^N h^3 = 0 \quad (3.46)$$

$$d_0^N + d_1^N h + d_2^N h^2 + d_3^N h^3 = 0 \quad (3.47)$$

For the first derivatives, it must hold that

$$a_1^0 = 0 \quad (3.48)$$

$$b_1^0 = 0 \quad (3.49)$$

$$c_1^0 = 0 \quad (3.50)$$

$$d_1^0 = 1 \quad (3.51)$$

$$a_1^N + 2a_2^N h + 3a_3^N h^2 = 0 \quad (3.52)$$

$$b_1^N + 2b_2^N h + 3b_3^N h^2 = 0 \quad (3.53)$$

$$c_1^N + 2c_2^N h + 3c_3^N h^2 = 0 \quad (3.54)$$

$$d_1^N + 2d_2^N h + 3d_3^N h^2 = 1 \quad (3.55)$$

The initial and final conditions for the second derivatives are

$$a_2^0 = 0 \quad (3.56)$$

$$b_2^0 = 0 \quad (3.57)$$

$$c_2^0 = 0 \quad (3.58)$$

$$d_2^0 = 0 \quad (3.59)$$

$$2a_2^N + 6a_3^N h = 0 \quad (3.60)$$

$$2b_2^N + 6b_3^N h = 0 \quad (3.61)$$

$$2c_2^N + 6c_3^N h = 0 \quad (3.62)$$

$$2d_2^N + 6d_3^N h = 0 \quad (3.63)$$

Moreover, continuity of the state trajectories up to the second time derivative has to be ensured. For $k = 0, \dots, N-1$, this implies that

$$\begin{aligned} Y^k(h) &= Y^{k+1}(0), & (Y^k)'(h) &= (Y^{k+1})'(0), & (Y^k)''(h) &= (Y^{k+1})''(0) \\ \Psi^k(h) &= \Psi^{k+1}(0), & (\Psi^k)'(h) &= (\Psi^{k+1})'(0), & (\Psi^k)''(h) &= (\Psi^{k+1})''(0) \\ X^k(h) &= X^{k+1}(0), & (X^k)'(h) &= (X^{k+1})'(0), & (X^k)''(h) &= (X^{k+1})''(0) \end{aligned}$$

Evaluating the above equations, we get for $k = 0, \dots, N-1$ and Y :

$$a_0^k + a_1^k h + a_2^k h^2 + a_3^k h^3 = a_0^{k+1} \quad (3.64)$$

$$a_1^k + 2a_2^k h + 3a_3^k h^2 = a_1^{k+1} \quad (3.65)$$

$$2a_2^k + 6a_3^k h = 2a_2^{k+1} \quad (3.66)$$

For $k = 0, \dots, N-1$ and Ψ

$$b_0^k + b_1^k h + b_2^k h^2 + b_3^k h^3 = b_0^{k+1} \quad (3.67)$$

$$b_1^k + 2b_2^k h + 3b_3^k h^2 = b_1^{k+1} \quad (3.68)$$

$$2b_2^k + 6b_3^k h = 2b_2^{k+1} \quad (3.69)$$

$k = 0, \dots, N-1$ and δ :

$$d_0^k + d_1^k h + d_2^k h^2 + d_3^k h^3 = d_0^{k+1} \quad (3.70)$$

$$d_1^k + 2d_2^k h + 3d_3^k h^2 = d_1^{k+1} \quad (3.71)$$

$$2d_2^k + 6d_3^k h = 2d_2^{k+1} \quad (3.72)$$

Collecting the parameters a_i^k, b_i^k, d_i^k for $k = 1, \dots, N$ and $i = 0, 1, 2, 3$ in the vector of decision variables z , the equality constraints in (3.40) to (3.63) and (3.64) to (3.72) can be written with suitable matrices A_{eq} and b_{eq} as

$$A_{\text{eq}} z = b_{\text{eq}}. \quad (3.73)$$

In addition, the dynamic equations in (3.20) to (3.23) need to be met. Evaluating these equations at each collocation point kh for $k = 0, \dots, N$, it must hold that

$$2d_2^k \cdot v^2 + d_1^k \cdot a_r = \frac{m a_r v \cos(b_0^k + c_0^k) - F_{\text{cf}} a_1^k v - F_{\text{cr}} d_1^k v \cos(c_0^k)}{m (d_1^k v \cos(b_0^k + c_0^k) + a_1^k v \sin(b_0^k + c_0^k))} \quad (3.74)$$

$$2a_2^k \cdot v^2 + a_1^k \cdot a_r = \frac{m a_r v \sin(b_0^k + c_0^k) + F_{\text{cf}} d_1^k v + F_{\text{cr}} d_1^k v \cos(c_0^k)}{m (d_1^k v \cos(b_0^k + c_0^k) + a_1^k v \sin(b_0^k + c_0^k))} \quad (3.75)$$

$$2b_2^k \cdot v^2 + b_1^k \cdot a_r = -\frac{F_{\text{cr}} b}{I_{zz}} + \frac{a (m a_r v \sin(c_0^k) + F_{\text{cf}} (d_1^k v \cos(b_0^k) + a_1^k v \sin(b_0^k)))}{I_{zz} (d_1^k v \cos(b_0^k + c_0^k) + a_1^k v \sin(b_0^k + c_0^k))} \quad (3.76)$$

$$F_{\text{cf}}^k = D \sin(C \tan^{-1}(B \alpha_f^k - E (B \alpha_f^k - \tan^{-1}(B \alpha_f^k)))) \quad (3.77)$$

$$F_{\text{cr}}^k = D \sin(C \tan^{-1}(B \alpha_r^k - E (B \alpha_r^k - \tan^{-1}(B \alpha_r^k)))) \quad (3.78)$$

$$\alpha_f^k = \tan^{-1}\left(\frac{-d_1^k \sin(b_0^k) + a_1^k \cos(b_0^k) + a b_1^k}{d_1^k \cos(b_0^k) + a_1^k \sin(b_0^k)}\right) - c_0^k \quad (3.79)$$

$$\alpha_r^k = \tan^{-1}\left(\frac{-d_1^k \sin(b_0^k) + a_1^k \cos(b_0^k) - b b_1^k}{d_1^k \cos(b_0^k) + a_1^k \sin(b_0^k)}\right) \quad (3.80)$$

These nonlinear equality constraints on the decision variables can be summarized as

$$c_{\text{eq}}(z, \dot{X}^0, \dots, \dot{X}^N, \ddot{X}^0, \dots, \ddot{X}^N) = 0. \quad (3.81)$$

Finally, the constraints on the input signal δ , the state variables Y , Ψ and their derivatives in (3.30) to (3.37) have to be considered for $k = 0, \dots, N$

$$Y_{\min} \leq a_0^k \leq Y_{\max}, \quad ppY_{\min} \leq 2a_2^k \leq ppY_{\max}, \quad (3.82)$$

$$\Psi_{\min} \leq b_0^k \leq \Psi_{\max}, \quad pp\Psi_{\min} \leq 2b_2^k \leq pp\Psi_{\max}, \quad (3.83)$$

$$\delta_{\min} \leq c_0^k \leq \delta_{\max}, \quad p\delta_{\min} \leq c_1^k \leq p\delta_{\max}, \quad (3.84)$$

These constraints can be written as

$$z_{\min} \leq z \leq z_{\max}. \quad (3.85)$$

with the lower bound z_{\min} and the upper bound z_{\max} for the decision variables z .

In summary, the optimal control problem in (3.28) to (3.37) is converted to the nonlinear optimization problem

$$\min_z \sum_{k=0}^{N-1} h \cdot (c_0^k)^2 + \gamma h (c_1^k)^2 \quad (3.86)$$

subject to

$$z_{\min} \leq z \leq z_{\max} \quad (3.87)$$

$$c_{\text{eq}}(z, \dot{X}^0, \dots, \dot{X}^N, \ddot{X}^0, \dots, \ddot{X}^N) = 0 \quad (3.88)$$

$$A_{\text{eq}} z = b_{\text{eq}}. \quad (3.89)$$

This nonlinear program can be solved by any nonlinear programming solver. In our work, the solver SNOPT [59] provided by the Tomlab software library is used.

3.3.2 Example Solution

We next show several example solutions when applying the collocation method for $\Delta Y = 3.7$, which is a common distance for lane changes [60]. Different lane change distances $S \in \{40, 50, 60, 70, 80, 90, 100, 110, 120\}$, travel velocities of $v \in$

$\{20, 30, 40, 50\}$ and different accelerations of $a_r \in \{-2, -1, 0, 1, 2\}$ are chosen. The following plots show the evolution of the Y -position along the arc-length for the different cases. Each plot belongs to a certain lane change distance and shows one subplot for each acceleration value. The results for each velocity are shown in these subplots. Note that some combinations of velocity/acceleration might be missing in cases where no optimal control solution could be found by the collocation method.

It can be seen from Fig. 3.2 and 3.9 that short arc-lengths can only be chosen for small velocities and accelerations. Otherwise, there is no solution for the optimal control problem. In addition, it can be seen from the figures that the trajectories for higher velocities start with a smaller curvature in most of the cases, especially in cases of a positive acceleration. It also has to be noted that, although the trajectories for different velocities are similar in many cases, some cases show large deviations. This observation suggests that the obtained solution might be incorrect in some cases. In order to verify the optimal control solutions, a gradient-based method for solving the optimal control problem is investigated in the next section.

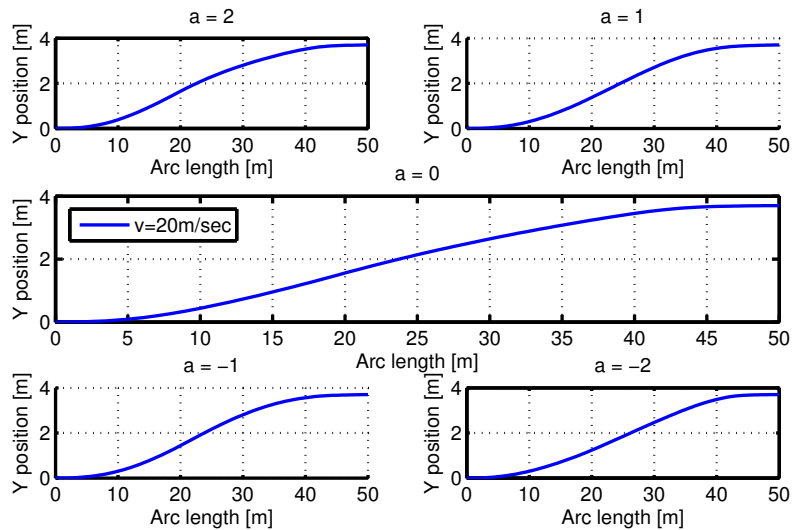


Figure 3.2: Optimal trajectory for $S = 50$, $a_r = -2$ and $a_r = -1$.

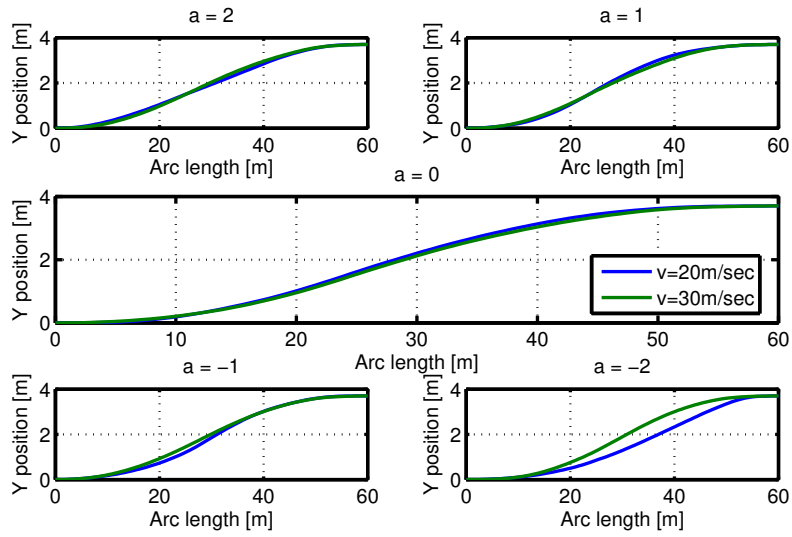


Figure 3.3: Optimal trajectory for $S = 60$; $a_r \in \{-2, -1, 0, 1, 2\}$.

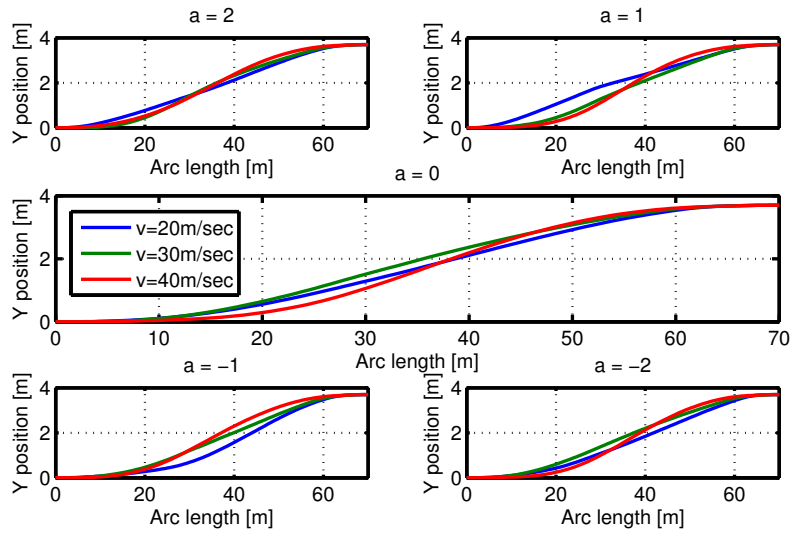


Figure 3.4: Optimal trajectory for $S = 70$; $a_r \in \{-2, -1, 0, 1, 2\}$.

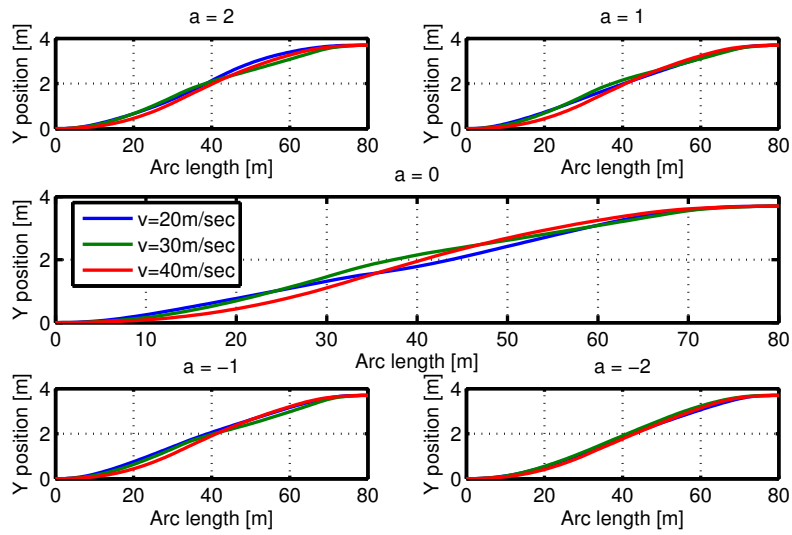


Figure 3.5: Optimal trajectory for $S = 80$; $a_r \in \{-2, -1, 0, 1, 2\}$

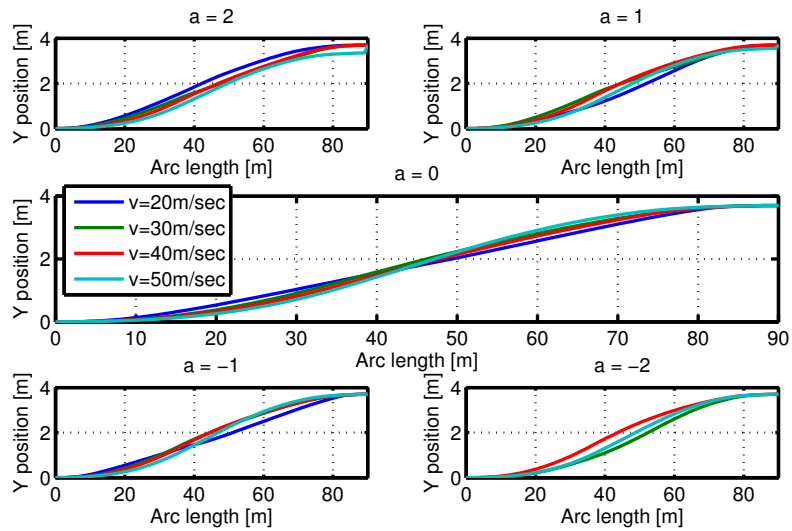


Figure 3.6: Optimal trajectory for $S = 90$; $a_r \in \{-2, -1, 0, 1, 2\}$

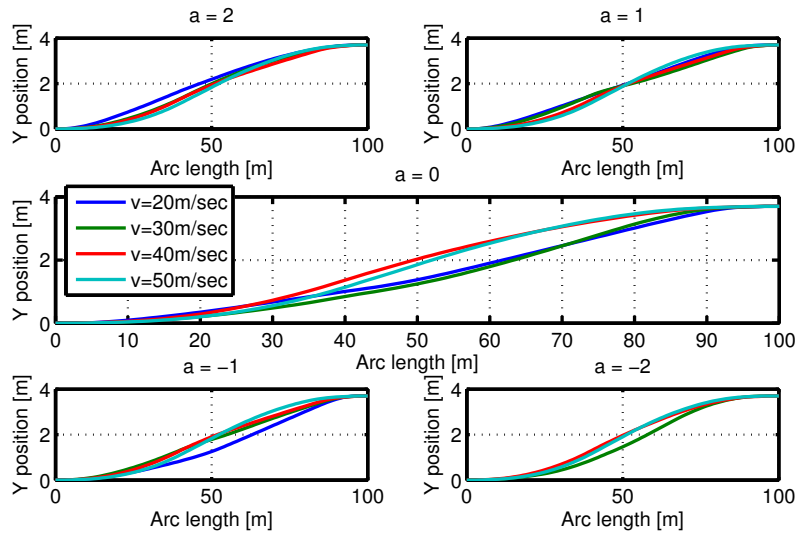


Figure 3.7: Optimal trajectory for $S = 100$; $a_r \in \{-2, -1, 0, 1, 2\}$

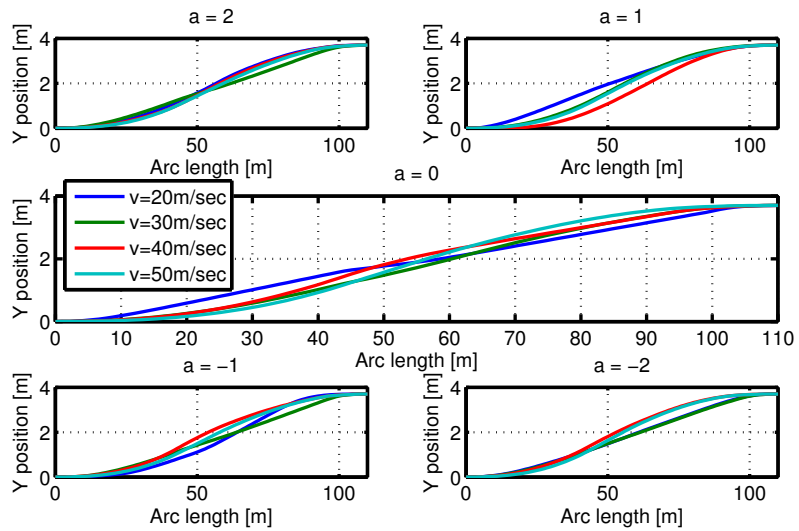


Figure 3.8: Optimal trajectory for $S = 110$; $a_r \in \{-2, -1, 0, 1, 2\}$

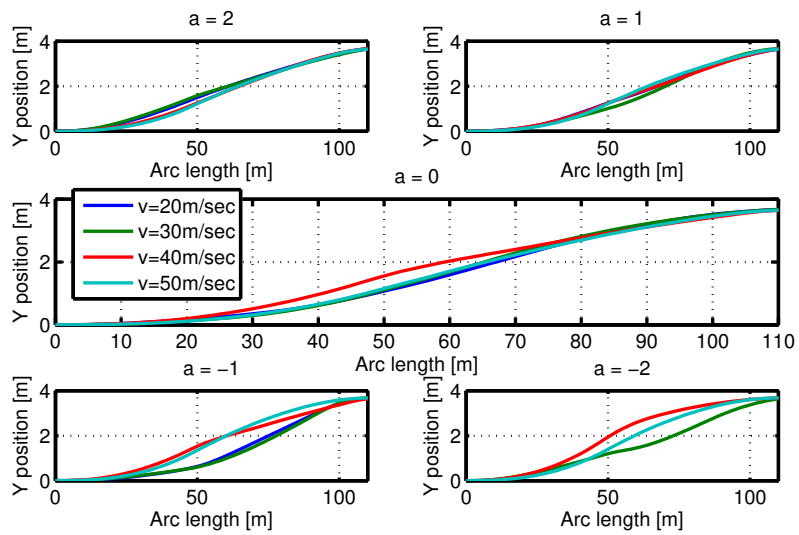


Figure 3.9: Optimal trajectory for $S = 120$; $a_r \in \{-2, -1, 0, 1, 2\}$

3.4 Gradient-based Method

In addition to the collocation method in the previous section, we develop a gradient-based method based on the model in Section 3.2.2.

3.4.1 Formulation of Our Method

In a general form, the state-space model in (3.24) to (3.27) can be written as

$$z' = f(z(s), u(s), s) \quad (3.90)$$

with the state $z = [\beta \ \Psi \ \Psi' \ X \ Y \ \delta \ w]$.

Then, the optimal control problem as in Section 3.2.3 can be formulated as

$$\min_u \phi(z(S)) \quad (3.91)$$

subject to the constraints

$$\dot{z} = f(z(s), u(s), s) \quad (3.92)$$

$$u \in \mathcal{U} \quad (3.93)$$

$$h_i(z(S)) = 0, \forall i \in E \quad (3.94)$$

$$g_j(z(S)) \leq 0, \forall j \in J \quad (3.95)$$

$$q(z(s)) \leq 0, \forall 0 \leq s \leq S. \quad (3.96)$$

The objective function is chosen as $\phi(z(S)) = w(S)$, the terminal equality constraints in (3.94) are the same as in (3.33) to (3.37), the input signal belongs to a given set \mathcal{U} in (3.93), terminal inequality constraints in (3.95) can be imposed if desired and (3.96) represents the additional state constraints in (3.30) to (3.32).

The problem in (3.91) to (3.96) is a nonlinear optimal control problem with state constraints. A gradient-based method for solving such optimal control problems is proposed in [61]. We next describe the adaption of this method for the computation of lane change maneuvers. The application of the method is based

on the reformulation of the problem in (3.91) to (3.96) in terms of the input signal u . To this end, the state depending on the applied input u is written as z^u and the objective function is written as $\tilde{F}_0(u) := \phi(z^u(s))$. Then, the reformulated problem is

$$\min_u \tilde{F}_0(u) \quad (3.97)$$

subject to the constraints

$$\tilde{h}_i(u) := h_i(z^u(S)) = 0, \forall i \in E \quad (3.98)$$

$$\tilde{g}_j(u) := g_j(z^u(S)) \leq 0, \forall j \in J \quad (3.99)$$

$$\tilde{q}(u)(t) := q(z^u(s), s) \leq 0, \forall 0 \leq s \leq S. \quad (3.100)$$

Using (3.97) to (3.100), the idea of the described method is to perform a search for the optimal input signal difference d based on first-order functional derivatives:

$$\tilde{F}_0(u+d) \approx \tilde{F}_0(u) + \langle \nabla \tilde{F}(u), d \rangle \quad (3.101)$$

$$\tilde{h}_i(u+d) \approx \tilde{h}_i(u) + \langle \nabla \tilde{h}_i(u), d \rangle, \quad \forall i \in E \quad (3.102)$$

$$\tilde{g}_j(u+d) \approx \tilde{g}_j(u) + \langle \nabla \tilde{g}_j(u), d \rangle, \quad \forall j \in J \quad (3.103)$$

$$\tilde{q}(u+d)(t) \approx \tilde{q}(u)(t) + \langle \nabla \tilde{q}(u)(t), d \rangle, \quad \forall t \in \mathbb{R}. \quad (3.104)$$

Using an arc-length discretization with (not necessarily equidistant) points s_0, s_1, \dots, s_n such that $s_0 = 0$ and $s_n = S$, the functional derivatives can be written as matrices in the form $F_0^u := \nabla \tilde{F}(u)$, $H_i^u := \nabla \tilde{h}_i(u)$, $G_j^u := \nabla \tilde{g}_j(u)$ and $Q_{s_k}^u := \nabla \tilde{q}(u)(s_k)$. These matrices are obtained by an explicit Runge-Kutta simulation using finite differences in the current implementation. Using these matrices and assuming a previously computed input signal u with the corresponding state z^u , a direction-finding subproblem is solved in order to find the best modification of the input signal d :

$$\min_{d \in \mathcal{U} - u, \beta \in \mathbb{R}} \beta + \frac{1}{2c} \|d\|^2 \quad (3.105)$$

subject to

$$\frac{F_0^u d}{c} + \max_{i \in E} |\tilde{h}_i(u) + H_i^u d| - \max_{i \in E} |\tilde{h}_i(u)| \leq \beta \quad (3.106)$$

$$\tilde{g}_j(u) + G_j^u d \leq \beta \quad (3.107)$$

$$\tilde{q}(u)(s_k) + Q_{s_k}^u d \leq \beta, \quad \forall s_0, \dots, s_n. \quad (3.108)$$

This direction-finding subproblem tries to find a small input difference d such that the first-order approximation fulfills the terminal and state inequality constraints in (3.107) and (3.108). In addition, the objective function is minimized together with the equality constraint violation in (3.106). This direction-finding subproblem is convex and can be solved by quadratic programming [61]. It is applied repeatedly during the actual optimal control algorithm:

Gradient-based Optimal Control Algorithm

1. Fix parameters $\gamma, \eta \in (0, 1)$, $c_0 > 0$, $\kappa > 1$. Choose an initial control input $u_0 \in \mathcal{U}$ which satisfies the constraints $\tilde{g}_j(u_0) \leq 0$ for $j \in J$ and $\tilde{q}(u_0)(t) \leq 0$ for all s_0, \dots, s_n . Set $l = 0$, $c_{-1} = c_0$,
2. Let c_l be the smallest number from the set $\{c_{l-1}, \kappa c_{l-1}, \kappa^2 c_{l-1}, \dots\}$ such that the solution (d_l, β_l) from the direction-finding subproblem satisfies

$$\beta_l + \frac{\max_{i \in E} |\tilde{h}_i(u_l)|}{c_l} \leq 0$$

3. **if $\beta_l = 0$ return**
4. Let a_l be the largest number from the set $\{1, \eta, \eta^2, \dots\}$ such that

$$\begin{aligned} \frac{\tilde{F}_0(u_l + a_l d_l)}{c_l} + \max_{i \in E} |\tilde{h}_i(u_l + a_l d_l)| &\leq \frac{\tilde{F}_0(u_l)}{c_l} + \max_{i \in E} |\tilde{h}_i(u_l)| + \gamma a_l \beta_l, \\ \tilde{g}_j(u_l + a_l d_l) &\leq 0, \forall j \in J \\ \tilde{q}(u_l + a_l d_l)(t_k) &\leq 0, \forall t_0, \dots, t_n. \end{aligned}$$

Write $u_{l+1} = u_l + a_l d_l$.

5. $l := l + 1$. **Go to step 2)**

The algorithm repeatedly tries to adjust the input signal by a difference d in order to minimize the objective function while fulfilling the terminal and state constraints. Step 1) defines parameters γ, η, κ and initializes the weight parameter c_l . In addition, an initial input signal is selected. Step 2) finds a suitable search direction d_l in order to jointly minimize the objective function and the violation of the equality constraints. If $\beta_l = 0$ in Step 3), it is concluded that no further improvement is possible such that the algorithm terminates. Otherwise, step 4) determines a largest possible input adjustment $a_l d_l$ along the chosen search direction without violating the actual constraints. This adjustment is added to the previously computed input signal such that the new input signal becomes $u_{l+1} = u_l + a_l d_l$. The algorithm is then repeated with the new input signal.

3.4.2 Example Solution

We apply the developed gradient-based method to the same scenarios as in Section 3.3.2. The resulting trajectories can be seen in the following figures. Similar to the evaluation of the collocation method in Section 3.3.2, it is the case that the optimal control problem cannot be solved for large velocities and small arc-lengths. Fig. 3.10 and 3.11 show that solutions for $S = 40$ and $S = 50$ are only possible for $v = 20$ m/sec. Optimal solutions for $v = 50$ m/sec are found starting from an arc-length of $S = 90$ (see Fig. 3.15). In general, it is observed that the optimal trajectories for larger velocities start with a smaller curvature. This effect can be intuitively explained by the fact that less steering is preferred when traveling at higher velocities.

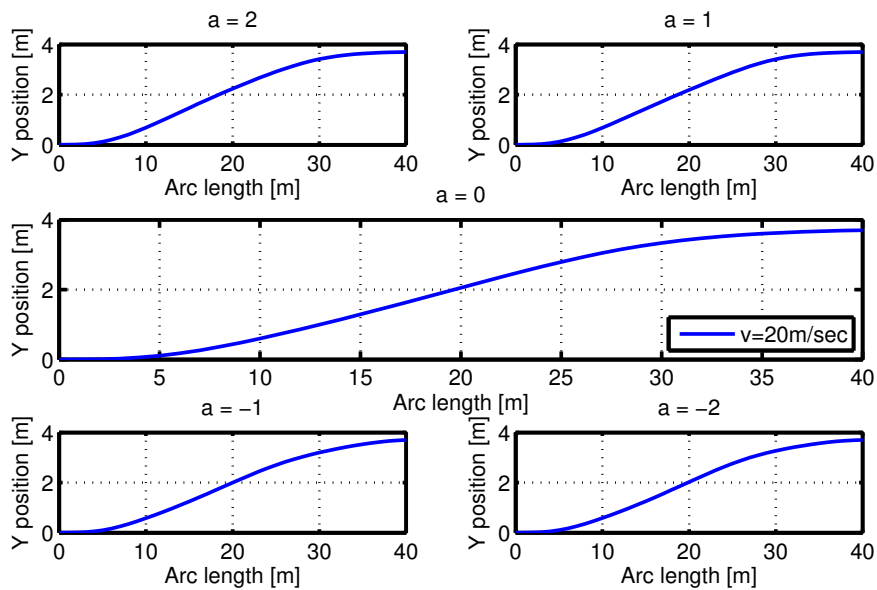


Figure 3.10: Gradient method: $S = 40$, $\Delta Y = 3.7$, $a \in \{-2, -1, 0, 1, 2\}$.

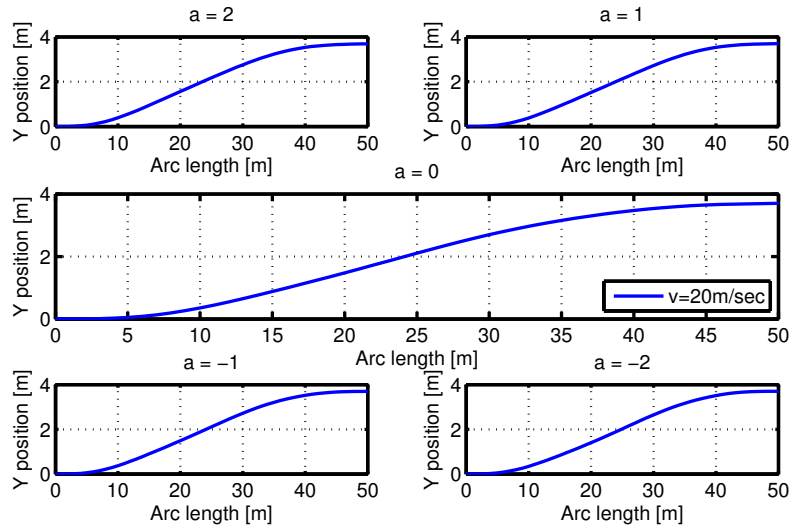


Figure 3.11: Gradient method: $S = 50$, $\Delta Y = 3.7$, $a \in \{-2, -1, 0, 1, 2\}$.

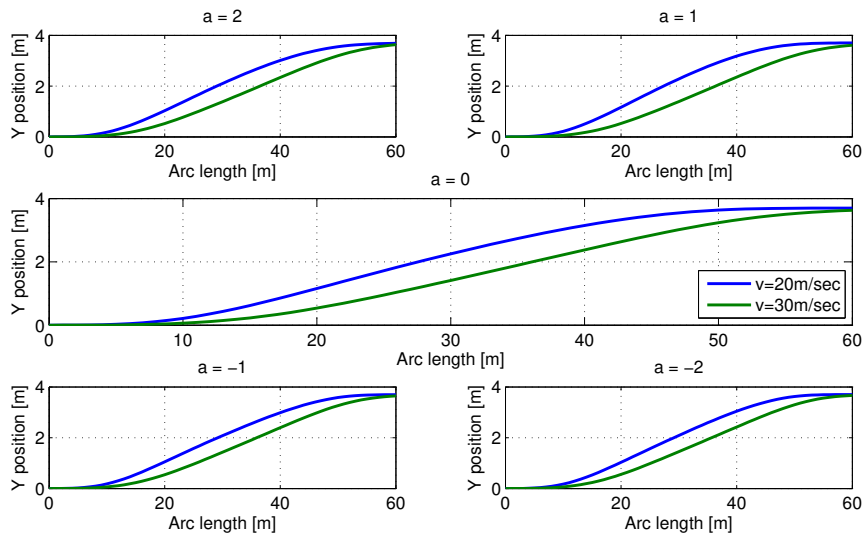


Figure 3.12: Gradient method: $S = 60$, $\Delta Y = 3.7$, $a \in \{-2, -1, 0, 1, 2\}$.

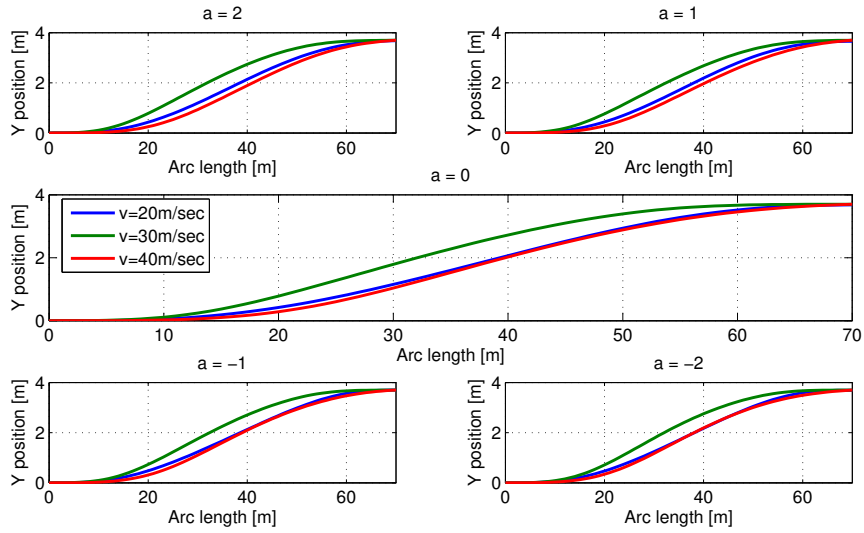


Figure 3.13: Gradient method: $S = 70$, $\Delta Y = 3.7$, $a \in \{-2, -1, 0, 1, 2\}$.

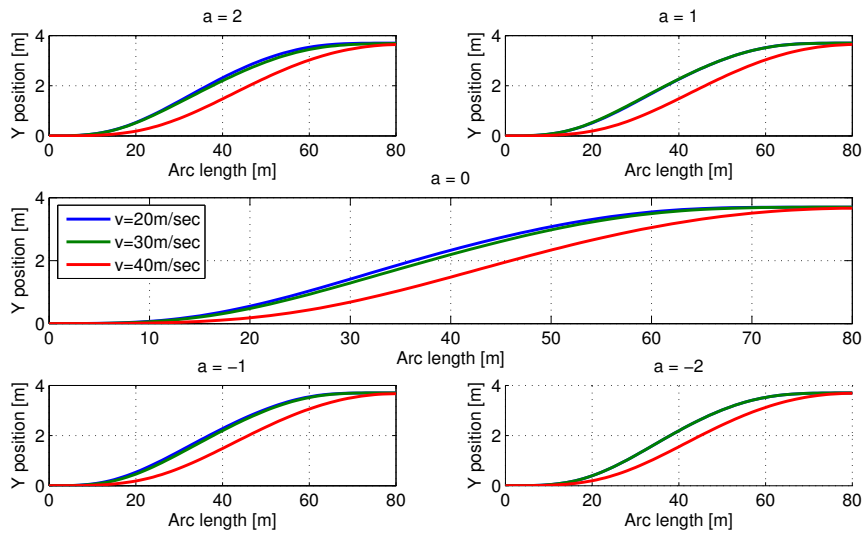


Figure 3.14: Gradient method: $S = 80$, $\Delta Y = 3.7$, $a \in \{-2, -1, 0, 1, 2\}$.

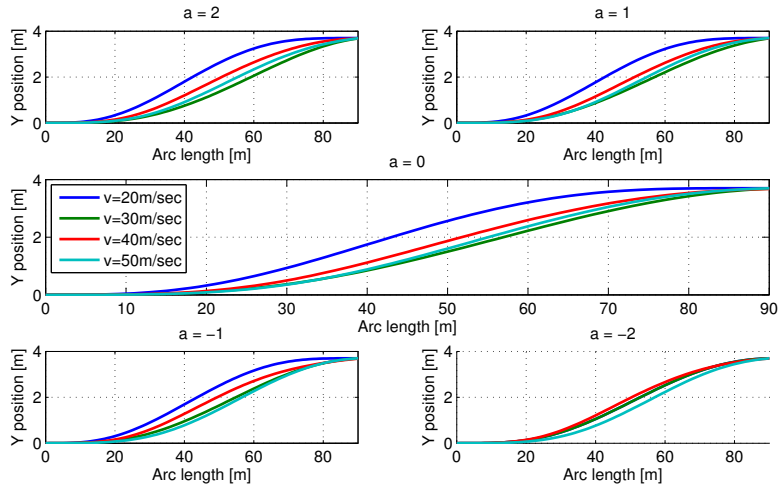


Figure 3.15: Gradient method: $S = 90$, $\Delta Y = 3.7$, $a \in \{-2, -1, 0, 1, 2\}$.

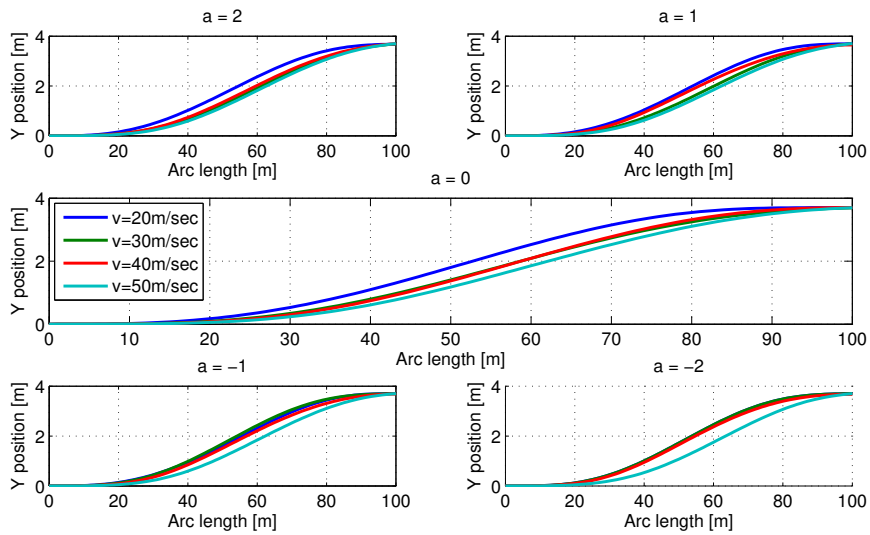


Figure 3.16: Gradient method: $S = 100$, $\Delta Y = 3.7$, $a \in \{-2, -1, 0, 1, 2\}$.

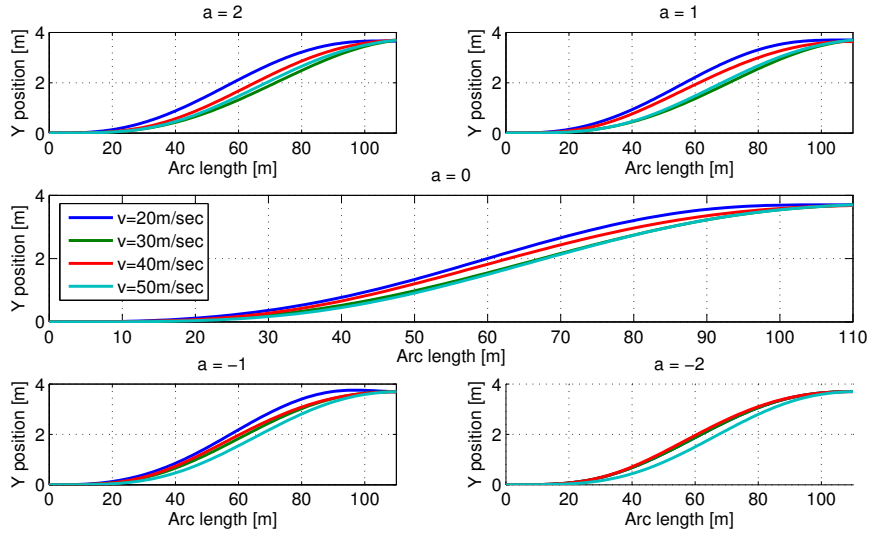


Figure 3.17: Gradient method: $S = 110$, $\Delta Y = 3.7$, $a \in \{-2, -1, 0, 1, 2\}$.

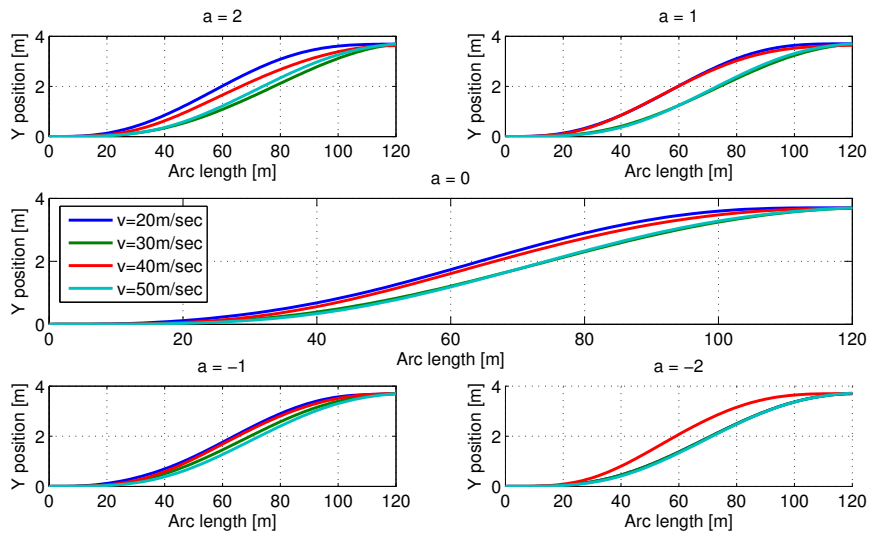


Figure 3.18: Gradient method: $S = 120$, $\Delta Y = 3.7$, $a \in \{-2, -1, 0, 1, 2\}$.

3.5 Comparison And Discussion

We finally compare the trajectories found by the two different optimal control methods. We choose different arc-lengths S and a low velocity of $v = 20$ and a high velocity of $v = 40$ for this comparison.

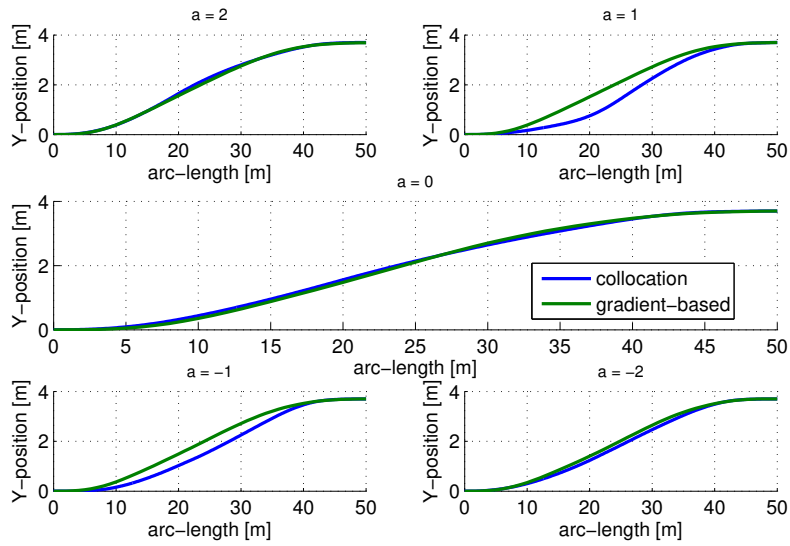


Figure 3.19: Comparison of optimal trajectories for $S = 50$, $v = 20$ and $a \in \{-2, -1, 0, 1, 2\}$.

It can be seen that both methods cannot find a solution for small arc-lengths and large velocities/accelerations. This is expected due to the vehicle dynamics. If a solution can be found, it can further be seen that the position trajectories for both methods are mostly similar. Nevertheless, it has to be noted that the optimal costs determined for both methods are not identical when looking at Table 3.1. In particular, much higher costs are required when using the collocation method, especially in the case of large velocities.

It is hence concluded that the collocation method faces numerical problems. When inspecting the optimal control solutions it turns out that these problems occur when representing the steering angle δ . In particular, oscillations in the steering angle are observed, leading to the larger cost compared to the gradient-

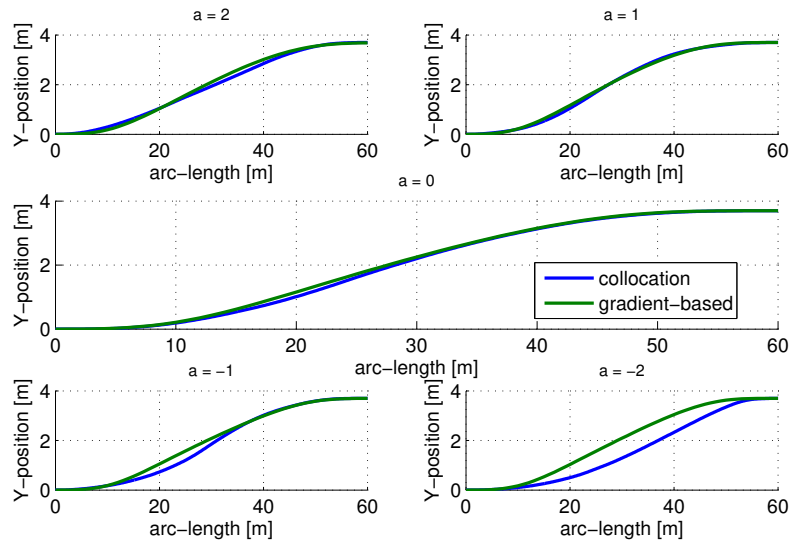


Figure 3.20: Comparison of optimal trajectories for $S = 60$, $v = 20$ and $a \in \{-2, -1, 0, 1, 2\}$.

based method when solving the optimal control problem. These oscillations can be seen in Fig. 3.31 and 3.32.

Together, it is concluded that the gradient-based method provides better and more reliable optimal control solutions for lane changes. Accordingly, the results of the gradient-based method are used for the further development of the thesis.

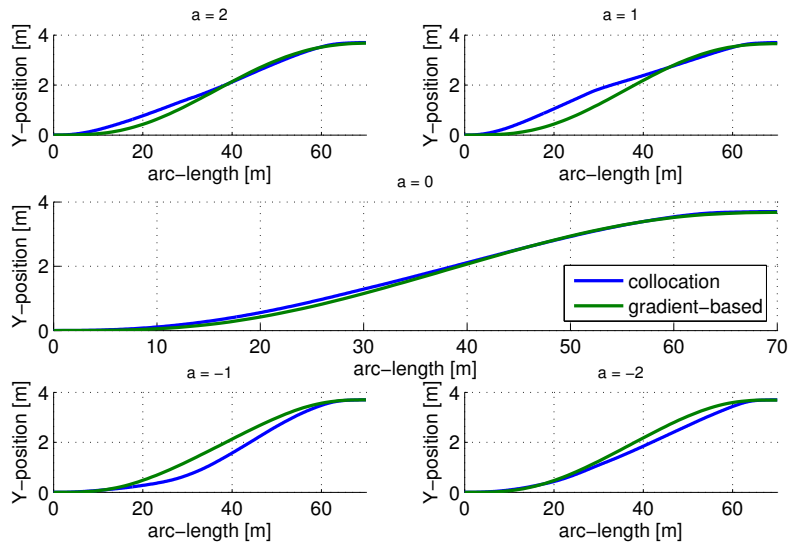


Figure 3.21: Comparison of optimal trajectories for $S = 70$, $v = 20$ and $a \in \{-2, -1, 0, 1, 2\}$.

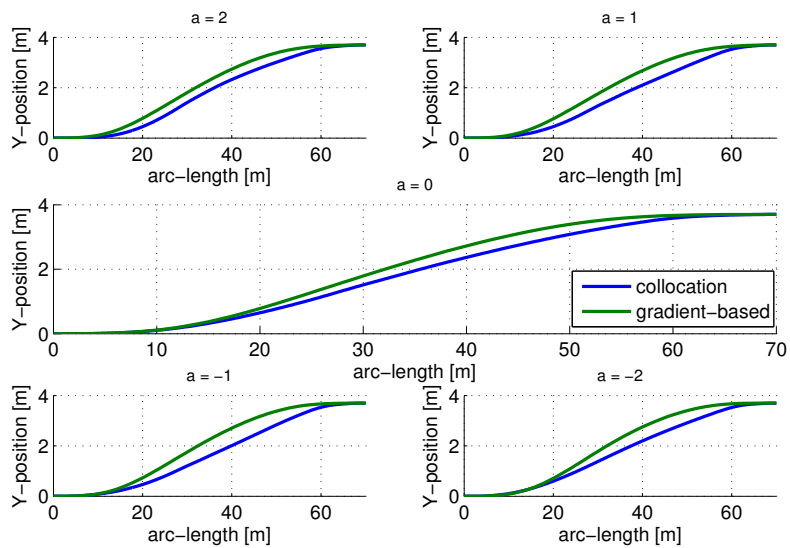


Figure 3.22: Comparison of optimal trajectories for $S = 70$, $v = 30$ and $a \in \{-2, -1, 0, 1, 2\}$.

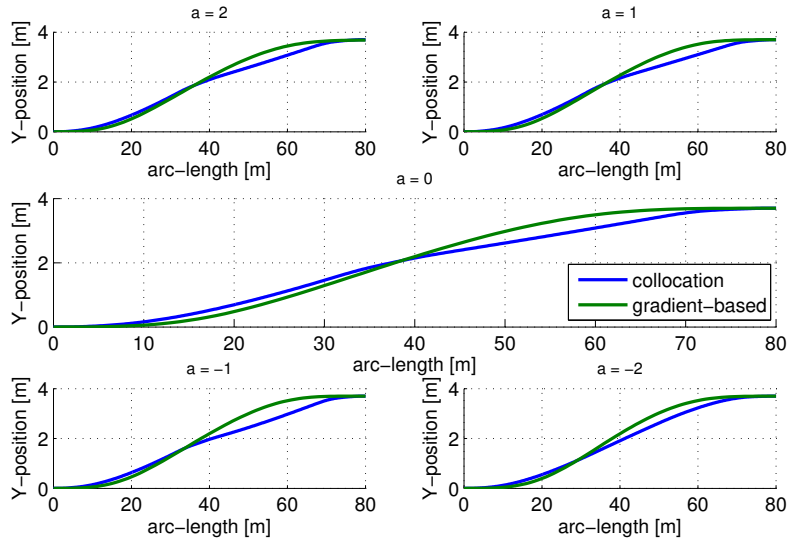


Figure 3.23: Comparison of optimal trajectories for $S = 80$, $v = 30$ and $a \in \{-2, -1, 0, 1, 2\}$.

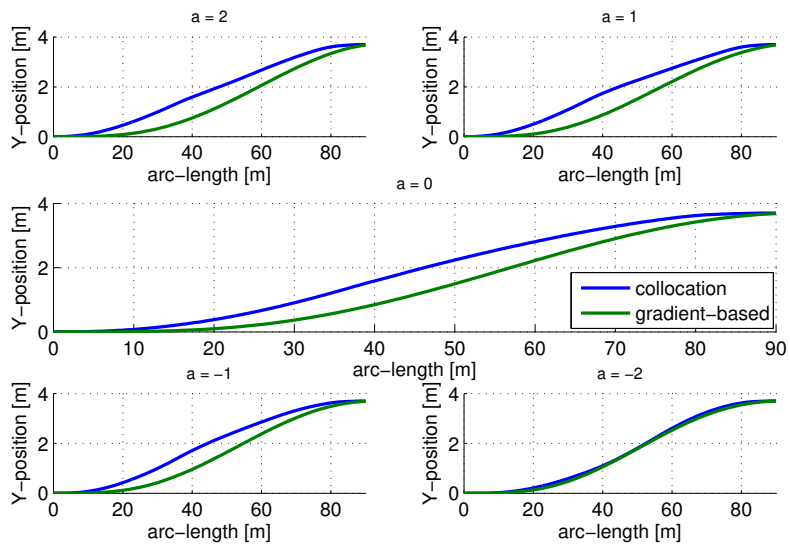


Figure 3.24: Comparison of optimal trajectories for $S = 90$, $v = 30$ and $a \in \{-2, -1, 0, 1, 2\}$.

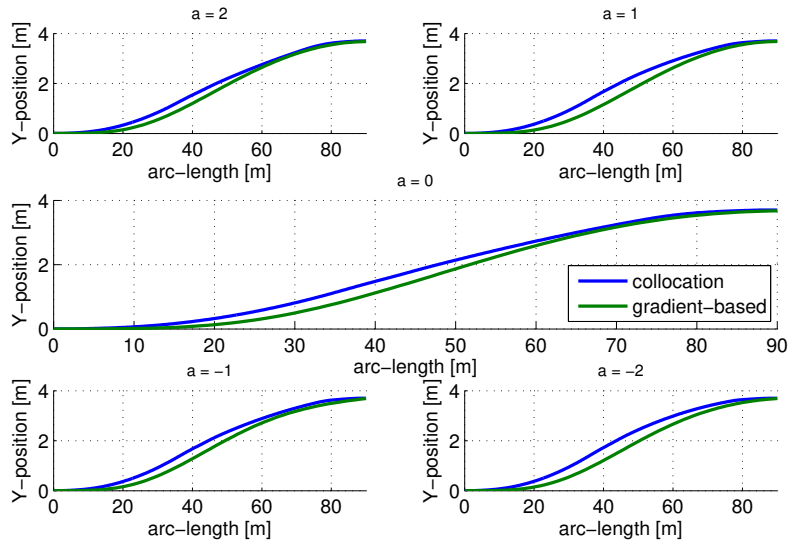


Figure 3.25: Comparison of optimal trajectories for $S = 90$, $v = 40$ and $a \in \{-2, -1, 0, 1, 2\}$.

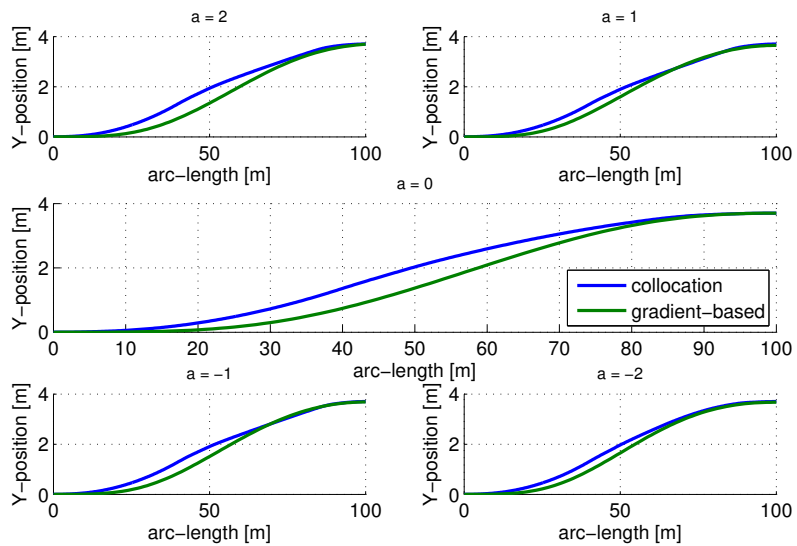


Figure 3.26: Comparison of optimal trajectories for $S = 100$, $v = 40$ and $a \in \{-2, -1, 0, 1, 2\}$.

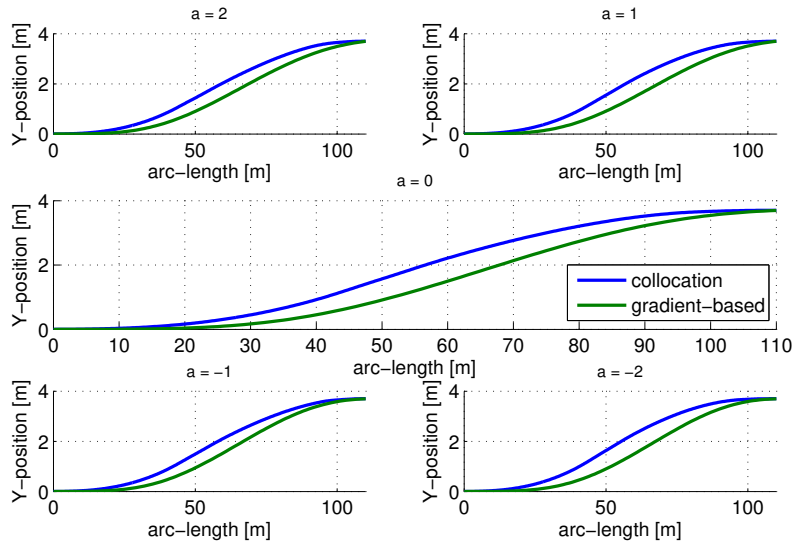


Figure 3.27: Comparison of optimal trajectories for $S = 110$, $v = 40$ and $a \in \{-2, -1, 0, 1, 2\}$.

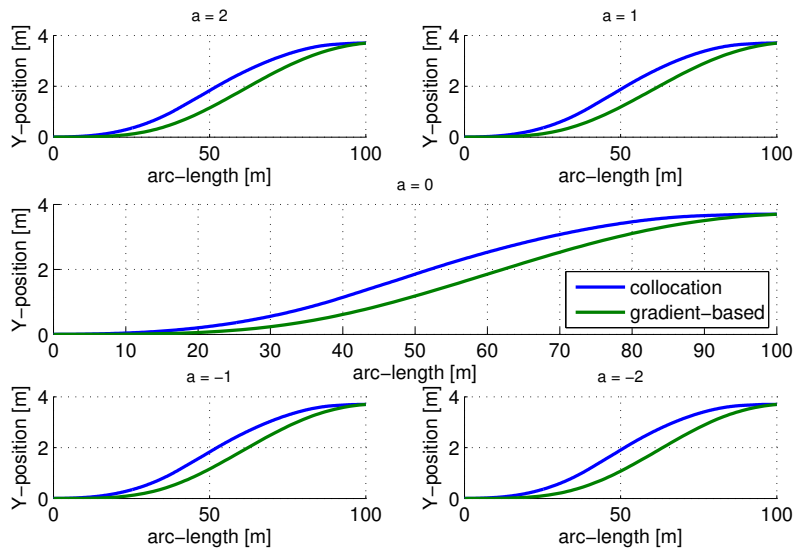


Figure 3.28: Comparison of optimal trajectories for $S = 100$, $v = 50$ and $a \in \{-2, -1, 0, 1, 2\}$.

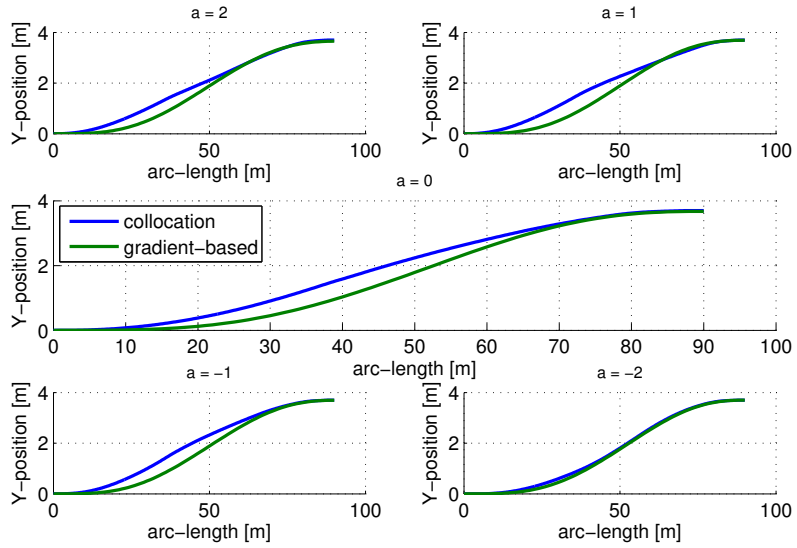


Figure 3.29: Comparison of optimal trajectories for $S = 110$, $v = 50$ and $a \in \{-2, -1, 0, 1, 2\}$.

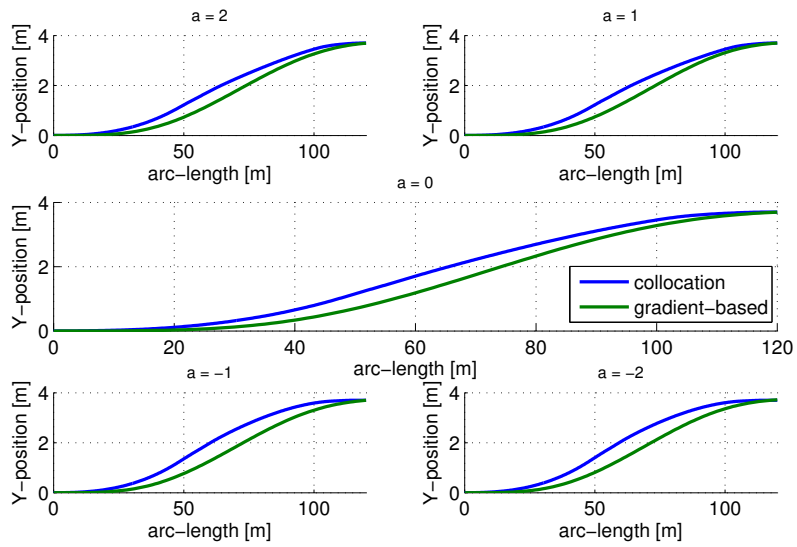


Figure 3.30: Comparison of optimal trajectories for $S = 120$, $v = 50$ and $a \in \{-2, -1, 0, 1, 2\}$.

Table 3.1: Comparison of optimal cost (10^{-3}) for collocation and gradient-based method

	$a = -2$		$a = -1$		$a = 0$		$a = 1$		$a = 2$	
	coll	grad	coll	grad	coll	grad	coll	grad	coll	grad
$S = 70, v = 20$	0.67	0.22	0.50	0.16	0.25	0.12	0.78	0.12	0.49	0.10
$S = 60, v = 20$	0.94	0.35	0.76	0.30	0.53	0.31	0.70	0.30	0.59	0.23
$S = 50, v = 20$	0.82	0.57	1.06	0.56	0.85	0.55	1.57	0.56	1.00	0.58
$S = 90, v = 30$	0.21	0.04	0.48	0.03	0.42	0.03	0.60	0.02	0.53	0.02
$S = 80, v = 30$	0.20	0.09	1.49	0.09	1.51	0.09	1.44	0.11	1.44	0.10
$S = 70, v = 30$	0.70	0.18	1.05	0.17	0.71	0.19	1.54	0.19	1.28	0.22
$S = 110, v = 40$	0.33	0.01	0.86	0.02	1.38	0.02	0.45	0.02	0.62	0.02
$S = 100, v = 40$	0.63	0.03	1.39	0.02	0.53	0.03	1.39	0.03	1.32	0.03
$S = 90, v = 40$	1.30	0.04	1.28	0.05	0.94	0.04	1.13	0.04	1.11	0.05
$S = 120, v = 50$	0.80	0.02	0.85	0.02	0.74	0.02	1.15	0.03	1.12	0.03
$S = 110, v = 50$	0.73	0.03	1.01	0.03	0.86	0.03	0.84	0.03	0.78	0.04
$S = 100, v = 50$	0.80	0.04	0.87	0.04	0.80	0.04	0.80	0.05	0.82	0.06

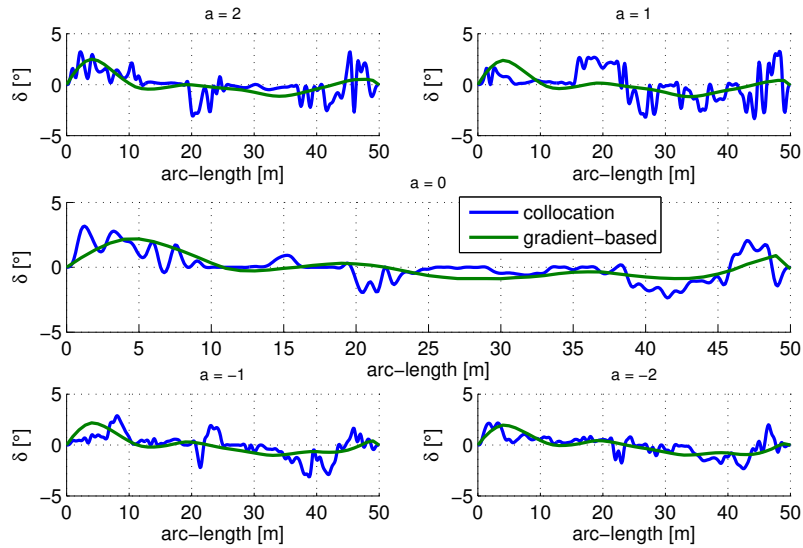


Figure 3.31: Comparison of optimal trajectories for $S = 50, v = 20$ and $a \in \{-2, -1, 0, 1, 2\}$.

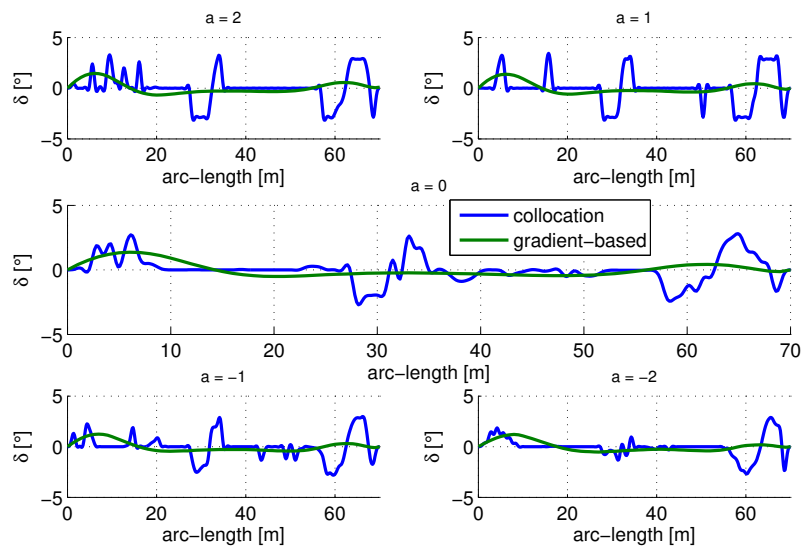


Figure 3.32: Comparison of optimal trajectories for $S = 70$, $v = 30$ and $a \in \{-2, -1, 0, 1, 2\}$.

CHAPTER 4

Approximation of Optimal Control Solutions

The previous chapter shows that lane change trajectories for self-driving vehicles can be determined by applying optimal control to nonlinear vehicle models. Although the computed optimal control inputs could be directly used as feedforward signals for performing lane changes, it has to be noted that it is not possible to determine the optimal control solutions in real-time. This chapter shows that the obtained optimal control trajectories are very similar to bi-elementary paths, which consist of clothoid segments. Accordingly, the focus of the chapter is the approximation of the optimal control solutions by bi-elementary arc-splines which can be computed in real-time.

The chapter is organized as follows. Section 4.1 presents a suitable control architecture and Section 4.2 provides a representation of position trajectories that are in general suitable for vehicle following applications. Section 4.3 shows an approximation of such trajectories that enables an easy trajectory parametrization. The parametrization of approximated optimal control trajectories is proposed and analyzed in detail in Section 4.4.

4.1 Control Architecture

It was identified in the previous chapter that optimal control trajectories for lane changes can be computed by the proposed gradient-based method. Nevertheless, it has to be noted that the computation of such optimal control trajectories has several practical disadvantages. First, it is not possible to solve the optimal control problem in real-time due to the different optimization steps. In addition, it has to be pointed out that the suggested computation requires a precise knowledge of the

velocity and acceleration signal of the vehicle during the lane change. Finally, it is the case that the computed optimal control solution is given by a feedforward input signal that has to be precisely applied to the vehicle. Hereby, the input signal is represented by time/steering angle pairs or position/steering angle pairs which need to be determined for each different lane change.

In order to circumvent the stated problems, this thesis suggests to employ a generic representation of the position trajectories that is suitable for lane changes. These position trajectories are then used as reference signals to be followed by the vehicle, whereby the trajectory following task can be realized by any lane keeping application. The suggested architecture can be seen in Fig. 4.1.

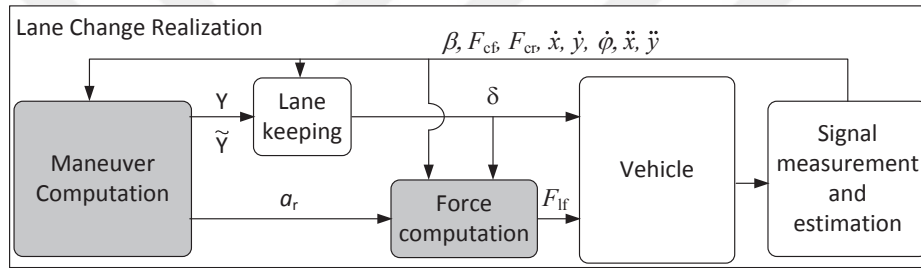


Figure 4.1: Control architecture for trajectory following during lane changes.

In this architecture, the vehicle receives the traction force F_{lf} and the steering angle δ as input signals. F_{lf} is computed as decoupling force according to (3.3). The steering angle is computed by the respective lane keeping control application. In this thesis, we assume that the lane keeping controller obtains the planned lane change trajectory Y and a short-term prediction of the vehicle trajectory \tilde{Y} as an input signal from the maneuver computation unit. In addition, real-time measurements are received from the vehicle. The main subject of this chapter is the computation of suitable lane change trajectories and predicted vehicle trajectories by the maneuver computation unit. Hereby, it is desired to determine a suitable representation of lane change trajectories that closely approximates the actual optimal control solution but that can be evaluated in real-time.

4.2 Elementary Paths and Bi-elementary Paths

In this section, we first introduce the notions of an elementary path and a bi-elementary path and discuss several properties of these curves.

4.2.1 Elementary Path

An elementary path consists of two clothoid curves that are joined together. Denoting the overall arc-length of an elementary path as S_e , the elementary path consists of two curves:

- First curve $C_1 = \mathcal{C}(P_s, \Psi_s, 0, k_1, S_e/2)$ with the curvature $k(s) = \frac{2k_1}{S_e}s$, $s \in [0, S_e/2]$. In particular, $k_f(C_1) = k_1$ is the curvature at the end of C_1 .
- Second curve: $C_2 = \mathcal{C}(P_e(C_1), \Psi_f(C_1), k_1, 0, S_e/2)$ with $k(s) = \frac{2k_1}{S_e}(S_e - s)$, $s \in [S_e/2, S_e]$. That is, the curvature at the end of the second curve is zero.

For convenience we denote such elementary path as

$$\mathcal{E}(P_s, \Psi_s, k_1, S_e) \quad (4.1)$$

An example for an elementary path with length $S_e = 100$ is show in Fig. 4.2.

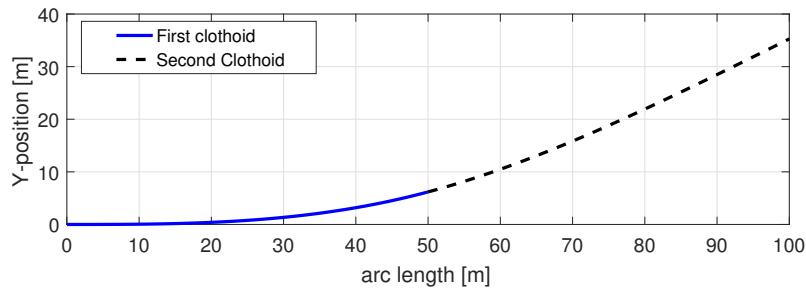


Figure 4.2: Elementary path $\mathcal{E}(0, 0, 0, 0.015, 100)$.

Using the same notation as in Section 2.2.1, several facts about elementary paths can be derived [31]. Consider a generic elementary path $E = \mathcal{E}(P_s, \Psi_s, k_1, S_e)$.

First, it holds that the tangent angle change can be expressed depending on the arc-length and the curvature parameter k_1 :

$$\alpha_E = \Psi_f(E) - \Psi_s(E) = 2 \tan^{-1} \left(\frac{Y_f(E) - Y_s(E)}{X_f(E) - X_s(E)} \right) = \frac{S_e k_1}{2}. \quad (4.2)$$

From the practical perspective, it is as well important to establish a relation between the tangent angle change α_E and the change $\Delta Y_E = Y_f(E) - Y_s(E)$ in the Y-position. For example, such relation will later be needed to evaluate the width of a lane change. To this end, it is recalled from [60] that

$$\Delta Y_E = S_e \cdot D(\alpha_E) \cdot \sin(\alpha_E/2). \quad (4.3)$$

Hereby, the function $D(\alpha_E)$ is defined as

$$D(\alpha_E) = 2 \int_0^{0.5} \cos(2\alpha(-s^2 + s)) ds. \quad (4.4)$$

Although it is not possible to evaluate (4.4) analytically, it is possible to compute $D(\alpha_E)$ for the relevant range of values for α_E . In this thesis, values of $\alpha_E \in [-\pi/4, \pi/4]$ are used. Noting that $D(\alpha_E) = D(-\alpha_E)$, it is hence, sufficient to evaluate $D(\alpha_E)$ in the interval $[0, \pi/4]$. The resulting function evaluation is shown in Fig. 4.3. For computational purposes, we propose to use a tight polynomial approximation of $D(\alpha_E)$. In the sequel, we use the approximation

$$\hat{D}(\alpha) = p_0 + p_1 \alpha + p_2 \alpha^2 + p_3 \alpha^3 \quad (4.5)$$

with the parameters $p_0 = 1$, $p_1 = 1.34 \cdot 10^{-4}$, $p_2 = -6.75 \cdot 10^{-2}$ and $p_3 = 1.64 \cdot 10^{-3}$. The approximation is chosen such that the residual norm is below 10^{-5} . $\hat{D}(\alpha_E)$ is also shown in Fig. 4.3.

4.2.2 Bi-elementary Path

The main objective of this section is the representation of lane change trajectories with the help of clothoids and their arc-spline approximations. Hereby, it has to

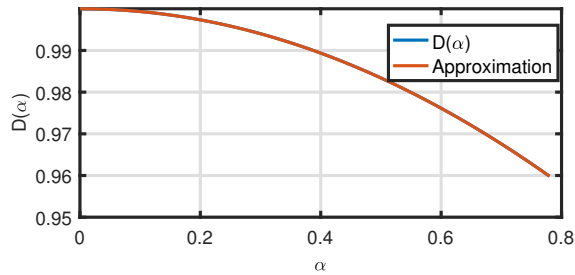


Figure 4.3: Approximation of $D(\alpha)$

be pointed out that elementary paths are not suitable for this task since they lead to a change α_E in the tangent angle, which is not desired for a lane change. However it is possible to concatenate two elementary paths with an opposite tangent angle change in order to obtain a bi-elementary path for lane change trajectories as shown in Fig. 4.4.

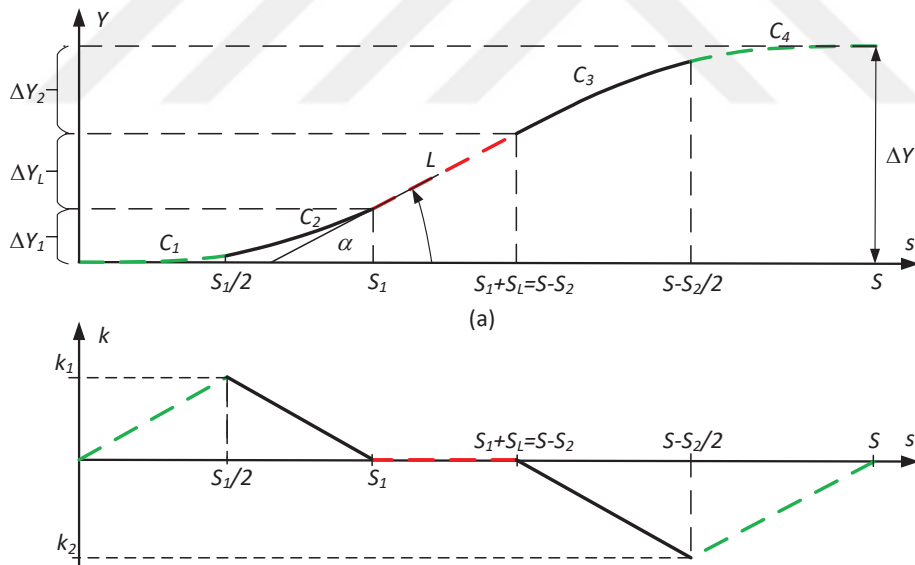


Figure 4.4: Components of a bi-elementary path.

A bi-elementary path consists of 5 segments C_1, C_2, L, C_3, C_4 that are defined in terms of the arc-length parameter s . The segments C_1 and C_2 form an elementary

path

$$E_1 = \mathcal{E}(0, 0, k_1, S_{e1}) \quad (4.6)$$

starting from the point $P_s(E_1) = 0$ with the tangent angle $\Psi_s(E_1) = 0$. The length of E_1 is S_{E_1} and the maximum curvature is k_1 . As a result, an angle change of $\alpha_{E_1} = \frac{S_{E_1} k_1}{2}$ is obtained. Writing $\alpha = \alpha_{E_1}$ for brevity, the change in the Y-position is approximated by

$$\Delta Y_{E_1} = S_{E_1} \hat{D}(\alpha) \sin(\alpha/2). \quad (4.7)$$

E_1 is followed by a straight line segment

$$L = \mathcal{L}(P_E(E_1), \Psi_f(E_1), S_l) \quad (4.8)$$

with length S_l and with the orientation angle α_{E_1} of the preceding elementary path E_1 . Accordingly, the change in the Y-position of L is

$$\Delta Y_L = S_l \sin(\alpha_{E_1}) \quad (4.9)$$

C_4 and C_5 again form an elementary path

$$E_2 = \mathcal{E}(P_f(L), \alpha, k_2, S_{E_2}) \quad (4.10)$$

with length S_{E_2} that starts from the end point $P_f(L)$ of the preceding line segment with the tangent angle α . In order to ensure that the tangent orientation $\Psi_f(E_2)$ at the end of the curve is zero, it must hold that

$$\alpha_{E_2} = \frac{S_{E_2} k_2}{2} = -\frac{S_{E_1} k_1}{2} = -\alpha.$$

That is, it must hold that

$$k_2 = -\frac{S_{e1} k_1}{S_{e2}}. \quad (4.11)$$

Since the tangent angle changes from α to zero, the associated change in the Y-position is approximated by

$$\Delta Y_{E_2} = S_{E_2} \hat{D}(\alpha) \sin(\alpha/2). \quad (4.12)$$

Then, the overall change in the Y-position of a bi-elementary path is derived from (4.7), (4.9) and (4.12) as

$$\Delta Y = S_{E_1} \hat{D}(\alpha) \sin(\alpha/2) + S_l \sin(\alpha) + S_{E_2} \hat{D}(\alpha) \sin(\alpha/2). \quad (4.13)$$

In the remainder of the thesis, it will be more convenient to consider a different parameterization of a bi-elementary path based on the share of each part in the overall arc-length S . To this end, we introduce the parameters $\lambda \in (0, 1)$ and $\gamma \in (0, 1]$ and define

$$\begin{aligned} S_{E_1} + S_{E_2} &= \gamma S \\ S_L &= (1 - \gamma) \cdot S \\ S_{E_1} &= \lambda \gamma S \\ S_{E_2} &= (1 - \lambda) \gamma S. \end{aligned}$$

That is, γ represents the length of the elementary paths in relation to the overall arc-length S . A large value of γ (and hence small value of $1 - \gamma$) implies a short straight line segment L . The ratio of the arc-lengths of the elementary paths E_1 and E_2 is given by λ . If $\lambda > 0.5$, it holds that E_1 is longer than E_2 .

Using these shape parameters λ and γ , a bi-elementary path can be characterized as

$$\mathcal{B}(S, k_1, \lambda, \gamma). \quad (4.14)$$

and the overall change in the Y-position is approximated as

$$\begin{aligned}
\Delta\hat{Y} &= \Delta Y_{E_1} + \Delta Y_L + \Delta Y_{E_2} \\
&= S_{E_1} \hat{D}(\alpha) \sin(\alpha/2) + S_L \sin(\alpha) + S_{E_2} \hat{D}(\alpha) \sin(\alpha/2) \\
&= \lambda \gamma S \hat{D}(\alpha) \sin(\alpha/2) + (1 - \gamma) S \sin(\alpha) + (1 - \lambda) \gamma \hat{D}(\alpha) \sin(\alpha/2) \\
&= S (\gamma \hat{D}(\alpha) \sin(\alpha/2) + (1 - \gamma) \sin(\alpha)). \tag{4.15}
\end{aligned}$$

In addition, we define the function $P_{\mathcal{B}} : [0, S] \mapsto \mathbb{R} : P_{\mathcal{B}}(s) = \begin{bmatrix} X(\mathcal{B}, s) \\ Y(\mathcal{B}, s) \end{bmatrix}$ as the trajectory of the bi-elementary path in the X-position and Y-position.

Fig. 4.5 and 4.6 show bi-elementary paths with arc-length $S = 100$ and curvature $k_1 = 0.005$ for different values of λ and γ . The variation of λ in Fig. 4.5 shows that choosing a larger value of λ (a longer first elementary path E_1) also leads to a larger change in the Y-position. The same effect is observed for a larger value of γ (a shorter straight line segment L) in Fig. 4.6.

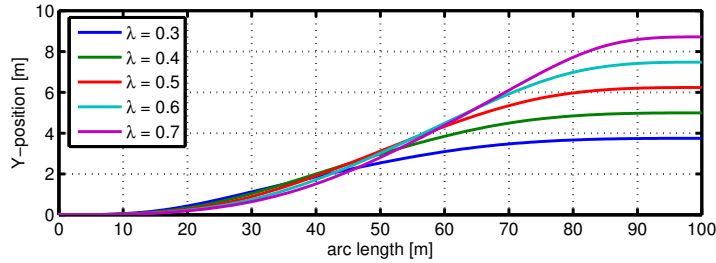


Figure 4.5: $\mathcal{B}(S, k_1, \lambda, \gamma)$ for $S = 100$, $k_1 = 0.005$, $\gamma = 1$ and different λ .

4.2.3 Parameter Computations

When determining lane change trajectories for self-driving vehicles based on bi-elementary paths, it is required to determine the relevant parameters S , λ , γ , ΔY , k_1 and α . According to the previous section, these 6 parameters are related by the

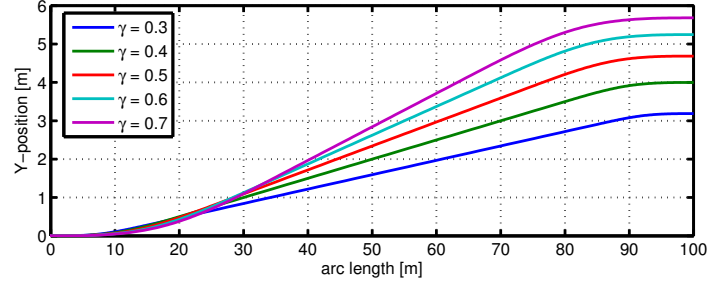


Figure 4.6: $\mathcal{B}(S, k_1, \lambda, \gamma)$ for $S = 100$, $k_1 = 0.005$, $\lambda = 0.5$ and different γ .

following equations:

$$\Delta Y = S (\gamma \hat{D}(\alpha) \sin(\alpha/2) + (1 - \gamma) \sin(\alpha)) \quad (4.16)$$

$$\alpha = \frac{\lambda \gamma S k_1}{2} \quad (4.17)$$

That is, it is required to assign four of these parameters. The remaining parameters can be computed from (4.16) and (4.17).

Regarding the choice of the fixed parameters, we consider two relevant cases. In all cases, the change in Y-position ΔY and the shape parameters λ and γ are given.

Case 1: λ , γ , k_1 and ΔY are given

In this case, it is assumed that also the curvature parameter k_1 is known. Since $|k_1|$ denotes the maximum curvature of the first elementary path and $|k_2| = \frac{\lambda k_1}{1 - \lambda}$ denotes the maximum curvature of the second elementary path, the choice of k_1 determines the maximum curvature encountered on the bi-elementary path. Then it is required to determine α and S . We know from (4.16) and (4.17) that

$$\frac{\gamma \lambda S k_1}{2} \Rightarrow S = \frac{2 \alpha}{\gamma \lambda k_1}.$$

This can be substituted in the equation for ΔY and we get

$$\Delta Y = \frac{2\alpha}{\gamma\lambda k_1} (\gamma\hat{D}(\alpha) \sin(\alpha/2) + (1 - \gamma) \sin(\alpha)).$$

This gives a nonlinear equation for α

$$f_1(\alpha) = 2\alpha (\gamma\hat{D}(\alpha) \sin(\alpha/2) + (1 - \gamma) \sin(\alpha)) - \Delta Y \lambda \gamma k_1 = 0. \quad (4.18)$$

It will be shown in Section 4.2.4 that (4.18) can be solved uniquely using the Newton method.

Case 2: λ , γ , S and ΔY are given

In this case, it is assumed that also the arc-length S is known. The choice of S determines the length of the lane change on the road. Then it is required to determine α and k_1 .

We know from the above equations that

$$\alpha = \frac{\gamma\lambda S k_1}{2} \Rightarrow k_1 = \frac{2\alpha}{\gamma\lambda S}.$$

This can be substituted in the equation for ΔY and we get

$$\Delta Y = S (\gamma\hat{D}(\alpha) \sin(\alpha/2) + (1 - \gamma) \sin(\alpha)).$$

This again gives a nonlinear equation for α that can be uniquely solved using the Newton method:

$$f_2(\alpha) = (\gamma\hat{D}(\alpha) \sin(\alpha/2) + (1 - \gamma) \sin(\alpha)) - \Delta Y/S = 0 \quad (4.19)$$

4.2.4 Newton Method

It is desired to obtain a fast solution of the nonlinear equations in (4.18) and (4.19) in order to evaluate bi-elementary paths for lane changes in real-time. This section shows that the Newton method is suitable for this purpose and even provides

a unique solution in both cases. To this end, we first briefly describe the Newton method. Consider the equation $f(\alpha) = 0$, where $f(\alpha)$ is a nonlinear function. Using an initial value α_0 and the first derivative $f'(\alpha)$ of $f(\alpha)$, the Newton iteration proceeds as follows

$$z_{i+1} = -\frac{f(z_i)}{f'(z_i)} + z_i, \quad i = 0, 1, \dots \quad (4.20)$$

The iteration terminates if $|f(\alpha_{i+1})| < \varepsilon$, where ε is a small tolerance value. Depending on the nonlinear function f , the convergence of the Newton method might be slow and it is not ensured that the correct root is found for functions with multiple roots. Nevertheless, there are several results that support unique convergence [62].

Proposition 2. *Consider a function $f : \alpha \mapsto f(\alpha) : [a, b] \rightarrow \mathbb{R}$. Assume that $f(\alpha)$ is twice differentiable and satisfies the following conditions on $[a, b]$:*

1. $f(a) < 0$ and $f(b) > 0$
2. $f'(\alpha) > 0$ on $[a, b]$
3. $f'' > 0$ on $[a, b]$

Then, the Newton iteration converges to a unique solution α^ of the equation $f(\alpha) = 0$ in $[a, b]$ if the starting value fulfills $\alpha_0 \geq \alpha^*$.*

Proposition 3. *Consider a function $f : \alpha \mapsto f(\alpha) : [a, b] \rightarrow \mathbb{R}$. Assume that $f(\alpha)$ is twice differentiable and satisfies the following conditions on $[a, b]$:*

1. $f(a) < 0$ and $f(b) > 0$
2. $f'(\alpha) > 0$ on $[a, b]$
3. $f'' < 0$ on $[a, b]$

Then, the Newton iteration converges to a unique solution α^ of the equation $f(\alpha) = 0$ in $[a, b]$ if the starting value fulfills $\alpha_0 \leq \alpha^*$.*

We next use these two propositions to show that the Newton iteration converges to a unique solution for the cases in Section 4.2.3 and 4.2.3.

Case 1

Theorem 1 shows that the nonlinear equation (4.18) fulfills the conditions in Proposition 2.

Theorem 1. Consider that $\alpha \in [0, \pi/4]$, $0 \leq \gamma \leq 1$, $0 \leq \lambda \cdot k_1 \leq 0.05$ and $0 < \Delta Y \leq 10$. Then, the nonlinear equation in (4.18) has a unique solution α^* that can be computed by the Newton iteration in (4.20) with the initial value $\alpha_0 = \pi/4$.

Proof. In order to prove Theorem 1 we show that (4.18) fulfills the conditions in Proposition 2. We consider the function $f(\alpha) = f_1(\alpha)$ in (4.18) and write

$$f_1(\alpha) = g_1(\alpha, \gamma) - \Delta Y \lambda \gamma k_1$$

with

$$g_1(\alpha, \gamma) = 2\alpha (\gamma \hat{D}(\alpha) \sin(\alpha/2) + (1 - \gamma) \sin(\alpha)).$$

That is, $g_1(\alpha, \gamma)$ depends on α, γ and $g_1(0, \gamma) = 0$ such that the offset value $f_1(0) = -\Delta Y \lambda \gamma k_1$ is only determined by $\Delta Y, \lambda, \gamma$ and k_1 . The evaluation of $g_1(\alpha, \gamma)$ for values of $\gamma \in (0, 1]$ and the relevant range of $\alpha \in [0, \pi/4]$ is given in Fig. 4.7.

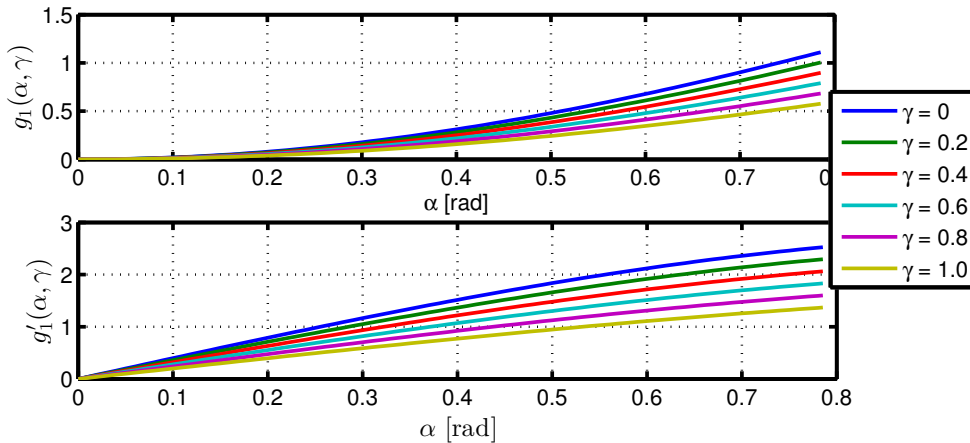


Figure 4.7: $g_1(\alpha, \gamma)$ and $g'_1(\alpha, \gamma)$ for $\gamma \in (0, 1]$ and $\alpha \in [0, \pi/4]$.

Focusing on the interval $[a, b] = [0, \pi/4]$, it is readily observed that $g_1(a, \gamma) = g_1(0, \gamma) = 0$ for all $\gamma \in (0, 1]$ and $g_1(b) = g_1(\pi/4) \geq 0.577$. In order to apply Proposition 2 item 1), it must hold that $f_1(a) < 0$ and $f_1(b) > 0$. Considering that $f_1(\alpha) = g_1(\alpha, \gamma) - \Delta Y \lambda \gamma k_1$ and $\Delta Y > 0$, $\lambda > 0$, $\gamma > 0$, $k_1 > 0$, it is clear that

$$f_1(a) = f_1(0) = g_1(0, \gamma) - \Delta Y \lambda \gamma k_1 = -\Delta Y \lambda \gamma k_1 < 0.$$

Then, it must be confirmed that $f_1(b) = f_1(\pi/4) = g_1(\pi/4, \gamma) - \Delta Y \lambda \gamma k_1 > 0$. To this end, we determine the largest value of $\Delta Y \lambda \gamma k_1$. It holds by assumption that $\lambda \in (0, 1)$, $\gamma \in (0, 1]$, $0 \leq k_1 \leq 0.05$ and $\Delta Y \leq 10$. Together, the desired bound evaluates to

$$\Delta Y \lambda \gamma k_1 < 10 \cdot 1 \cdot 0.05 = 0.5 < \min_{\gamma} g_1(b, \gamma) = 0.577.$$

That is, indeed $f_1(b) > 0$ such that condition 1) in Proposition 2 is fulfilled.

In addition, it holds that

$$f_1'(\alpha) = g_1'(\alpha, \gamma) > 0$$

for all values of $\gamma \in (0, 1]$, $\lambda \in (0, 1)$, ΔY and k_1 and $f_1''(\alpha) = g_1''(\alpha, \gamma)$ is always positive for $\alpha \in [0, \pi/4]$ as can be verified by Fig. 4.7. Hence, condition 2) and 3) in Proposition 2 are also true.

Since it is assumed that only angles in the interval $[0, \pi/4]$ are suitable for lane changes, it suffices to choose $\alpha_0 = \pi/4$ in order to fulfill all conditions in Proposition 2. \square

In words, Theorem 1 confirms that the Newton iteration with the function $f_1(\alpha)$ in (4.18) converges to the unique solution α^* . Applying $S^* = \frac{2\alpha^*}{\lambda \gamma k_1}$, this leads to a lane change with width ΔY using the bi-elementary path $\mathcal{B}(S^*, k_1, \lambda, \gamma)$.

When applying Theorem 1, the defined bounds for λ , γ , k_1 and ΔY need to be justified. By definition, it is clear that $0 \leq \lambda, \gamma \leq 1$. In addition, it holds that the curvature parameter k_1 represents the inverse of the road radius. Considering that the smallest possible radius for a vehicle is given by the turning circle radius R_T ,

it must hold that $k_1 \leq 1/R_T$ and $|k_2| = \frac{\lambda k_1}{1-\lambda} \leq 1/R_T$. That is,

$$\frac{\lambda k_1}{1-\lambda} \leq 1/R_T \Rightarrow \lambda (k_1 + 1/R_T) < 1/R_T \Rightarrow \lambda < \frac{1/R_T}{k_1 + 1/R_T} \Rightarrow \lambda k_1 < \frac{1/R_T k_1}{k_1 + 1/R_T}$$

Considering that k_1 is bounded by $1/R_T$, the bound for λk_1 is given by

$$\lambda k_1 < \frac{1/R_T \cdot 1/R_T}{1/R_T + 1/R_T} = \frac{1}{2R_T}. \quad (4.21)$$

Applying the fact that the turning radius of series vehicles is usually not below 10m, it can hence be assumed that $\lambda k_1 \leq 0.05$. In addition, ΔY represents the lane width for a lane change. When performing a single lane change, the lane width is usually assumed as $\Delta Y = 3.7$ m. Also allowing for multiple or wider lane changes, we consider a bound of $\Delta Y \leq 10$.

We next provide several examples for bi-elementary paths that were computed according to Case 1 as described before. Fig. 4.8 shows the case where k_1 is varied. It is evident that a larger curvature enables a shorter lane change trajectory. Similarly, a larger value of λ in Fig. 4.9 and a larger value of γ in Fig. 4.10 result in shorter lane change trajectories.

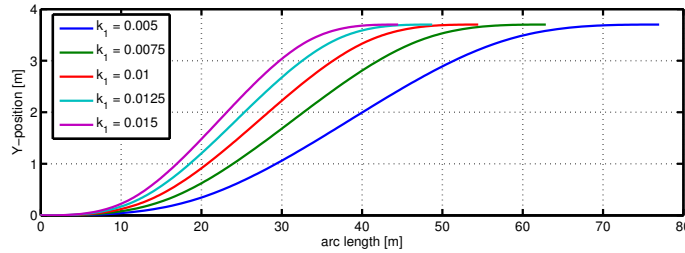


Figure 4.8: $\mathcal{B}(S, k_1, \lambda, \gamma)$ for $\Delta Y = 3.7$, $\lambda = 0.5$, $\gamma = 1$ and different k_1 .

Case 2

We next show that the nonlinear equation (4.19) fulfills the conditions in Proposition 2.

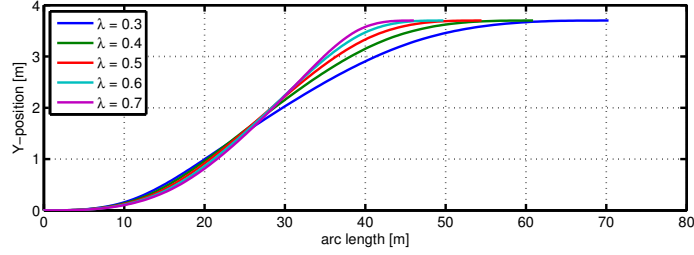


Figure 4.9: $\mathcal{B}(S, k_1, \lambda, \gamma)$ for $\Delta Y = 3.7$, $k_1 = 0.01$, $\gamma = 1$ and different λ .

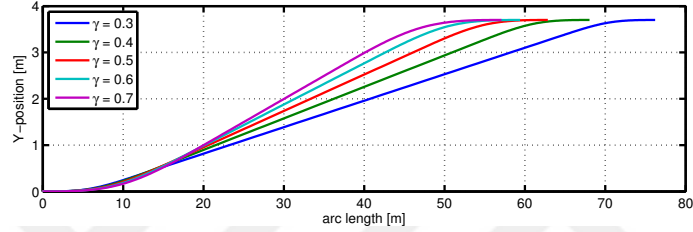


Figure 4.10: $\mathcal{B}(S, k_1, \lambda, \gamma)$ for $\Delta Y = 3.7$, $k_1 = 0.01$, $\lambda = 0.5$ and different γ .

Theorem 2. Consider that $\alpha \in [0, \pi/4]$, $0 \leq \gamma \leq 1$, $S \geq 30$ and $0 < \Delta Y \leq 10$. Then, the nonlinear equation in (4.19) has a unique solution α^* that can be computed by the Newton iteration in (4.20) with the initial value $\alpha_0 = 0$.

Proof. We consider the function $f(\alpha) = f_2(\alpha)$ in (4.19) and write

$$f_2(\alpha) = g_2(\alpha, \gamma) - \Delta Y/S$$

with

$$g_2(\alpha, \gamma) = (\gamma \hat{D}(\alpha) \sin(\alpha/2) + (1 - \gamma) \sin(\alpha)).$$

That is, $g_2(\alpha, \gamma)$ depends on α, γ and $g_2(0, \gamma) = 0$ such that the offset value $f_2(0) = -\Delta Y/S$ is only determined by ΔY and S . The evaluation of $g_2(\alpha, \gamma)$ for values of $\gamma \in (0, 1]$ and the relevant range of $\alpha \in [0, \pi/4]$ is given in Fig. 4.11.

Focusing on the interval $[a, b] = [0, \pi/4]$, it is readily observed that $g_2(a, \gamma) = g_2(0, \gamma) = 0$ for all $\gamma \in [0, 1]$ and $g_2(b) = g_2(\pi/4) \geq 0.367$. In order to apply Proposition 3 1), it must hold that $f_2(a) < 0$ and $f_2(b) > 0$. Considering that

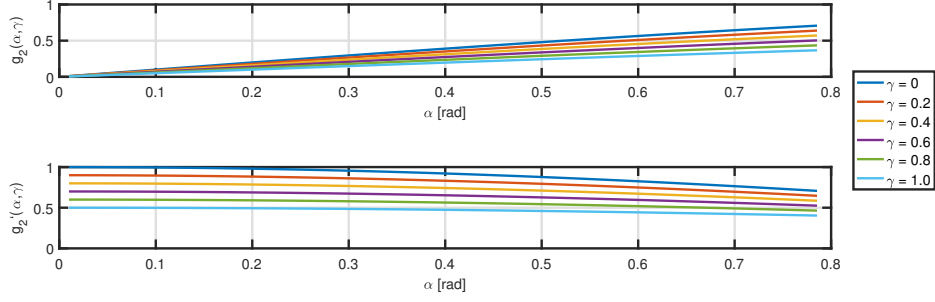


Figure 4.11: $g_2(\alpha, \gamma)$ for $\gamma \in (0, 1]$ and $\alpha \in [0, \pi/4]$.

$f_2(\alpha) = g_2(\alpha, \gamma) - \Delta Y/S$ and $\Delta Y > 0$, $S > 0$, it is clear that

$$f_2(a) = f_2(0) = g_2(0, \gamma) - \Delta Y/S = -\Delta Y/S < 0.$$

Then, it must be confirmed that $f_2(b) = f_2(\pi/4) = g_2(\pi/4, \gamma) - \Delta Y/S > 0$. To this end, we determine the largest value of $\Delta Y/S$. Similar to Section 4.2.4, we consider a bound of $\Delta Y \leq 10$. In addition, we consider a shortest arc-length for a lane change of $S = 30$ as in [60]. Then, the desired bound evaluates to

$$\Delta Y/S < 10/40 = 0.25 < \min_{\gamma} g_2(b, \gamma) = 0.367.$$

That is, indeed $f_2(b) > 0$ such that condition 1) in Proposition 3 is fulfilled.

In addition, it holds that

$$f_2'(\alpha) = g_2'(\alpha, \gamma) > 0$$

for all values of $\gamma \in [0, 1]$, $\lambda \in (0, 1)$, ΔY and k_1 and $f_2''(\alpha) = g_2''(\alpha, \gamma)$ is always negative for $\alpha \in [0, \pi/4]$ as can be verified by Fig. 4.11. Hence, condition 2) and 3) in Proposition 2 are also true.

Since it is assumed that only angles in the interval $[0, \pi/4]$ are suitable for lane changes, it suffices to choose $\alpha_0 = 0$ in order to fulfill all conditions in Proposition 3. \square

We next provide several examples for bi-elementary paths that were computed according to Case 2 as described before. Fig. 4.12 shows the case of an increasing arc-length, Fig. 4.13 shows the case of an increased value of λ and Fig. 4.14 shows the case of an increased value of γ .

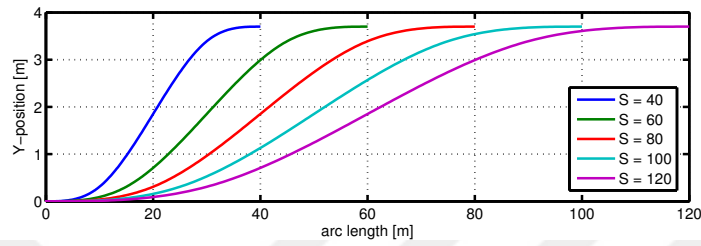


Figure 4.12: $\mathcal{B}(S, k_1, \lambda, \gamma)$ for $\Delta Y = 3.7$, $\lambda = 0.5$, $\gamma = 1$ and different S .

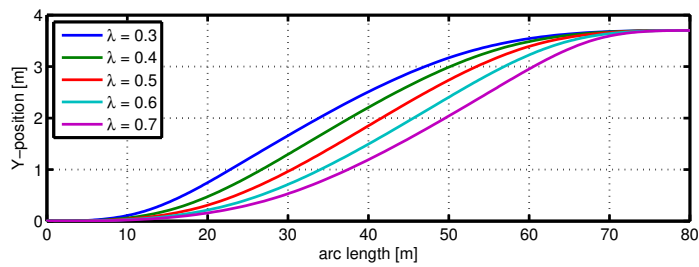


Figure 4.13: $\mathcal{B}(S, k_1, \lambda, \gamma)$ for $\Delta Y = 3.7$, $S = 80$, $\gamma = 1$ and different λ .

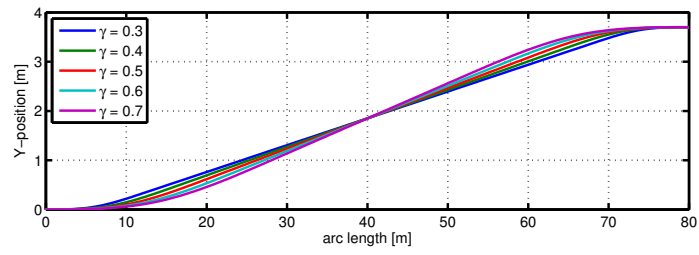


Figure 4.14: $\mathcal{B}(S, k_1, \lambda, \gamma)$ for $\Delta Y = 3.7$, $S = 80$, $\lambda = 0.5$ and different γ .

4.3 Approximations of Elementary and Bi-elementary Paths

4.3.1 Approximation of Elementary Paths

According to Section 4.2.1, an elementary path with arc-length S_e is represented by two clothoid curves $C_1 = \mathcal{C}(P_s, \Psi_s, 0, k_1, S_e/2)$ and $C_2 = \mathcal{C}(P_e(C_1), \Psi_f(C_1), k_1, 0, S_e/2)$. Hence, it is possible to approximate an elementary path by arc-spline approximations $\hat{C}_1 = \hat{\mathcal{C}}(P_s, \Psi_s, 0, k_1, S_e/2, n)$ and $\hat{C}_2 = \hat{\mathcal{C}}(P_e(C_1), \Psi_f(C_1), k_1, 0, S_e/2, n)$ of C_1 and C_2 , respectively. We denote the corresponding approximated elementary path as $\hat{\mathcal{C}}(P_s, \Psi_s, k_1, S, n)$.

An example of such approximation is shown in Fig. 4.15.

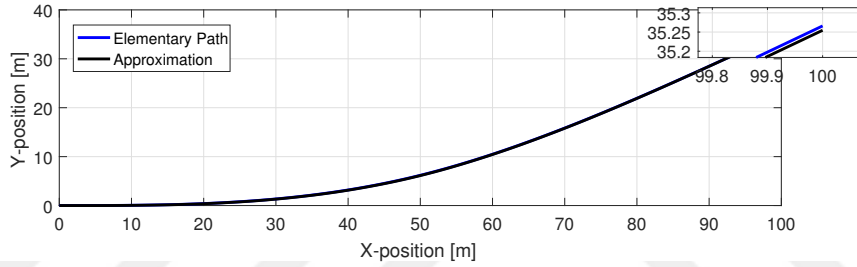


Figure 4.15: Elementary path $\mathcal{C}(0,0,0,0.015,100)$ and approximation $\hat{\mathcal{C}}(0,0,0,0.015,100,5)$.

4.3.2 Approximation of Bi-elementary Paths

In analogy to Section 4.3.1, a bi-elementary path can be approximated by arc-splines. Consider $\mathcal{B}(S, k_1, \lambda, \gamma)$, which is defined by $E_1 = \mathcal{C}(0,0, k_1, \lambda \gamma S)$, $L = \mathcal{L}(P_e(E_1), \Psi_f(E_1), \gamma S)$ and $E_2 = \mathcal{C}(P_e(L), \Psi_f(L), \frac{-\lambda k_1}{1-\lambda}, (1-\lambda) \gamma S)$. Then, the approximation of a bi-elementary path is given by the corresponding approximations $\hat{E}_1 = \hat{\mathcal{C}}(0,0, k_1, \lambda \gamma S, n)$, $\hat{L} = \mathcal{L}(P_e(\hat{E}_1), \Psi_f(\hat{E}_1), \gamma S)$ and $\hat{E}_2 = \hat{\mathcal{C}}(P_e(\hat{L}), \Psi_f(\hat{L}), \frac{-\lambda k_1}{1-\lambda}, (1-\lambda) \gamma S, n)$. It is denoted as $\hat{\mathcal{B}}(S, k_1, \lambda, \gamma, n)$.

4.3.3 Distance Computation

When using arc-splines to approximate vehicle trajectories, it is possible to analytically evaluate the distance of any point to the arc-spline. This is of high relevance when evaluating the distance error for trajectory following. We next present this distance evaluation for the two relevant trajectory segments. Line segments and arc segments.

The basic layout for line segments is shown in Fig. 4.16.

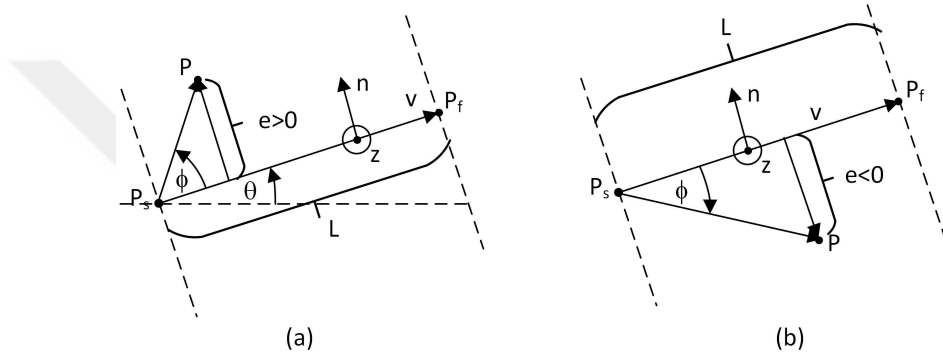


Figure 4.16: Distance error for a line segment: (a) positive error; (b) negative error.

We consider a generic line segment $L = \mathcal{L}(P_s, \Psi_s, S)$ with the starting point P_s , the orientation angle Ψ_s and the length S . The point of interest is P . The vectors in the figure are computed as

$$v = L \begin{bmatrix} \cos(\theta) \\ \sin(\theta) \end{bmatrix}, \quad (4.22)$$

$$n = \frac{1}{L} \cdot z \otimes v = \frac{1}{L} \cdot \begin{bmatrix} 0 \\ 0 \\ 1 \end{bmatrix} \otimes \begin{bmatrix} v \\ 0 \end{bmatrix} = \frac{1}{L} \begin{bmatrix} -\sin(\theta) \\ \cos(\theta) \end{bmatrix}, \quad (4.23)$$

$$w = P - P_s. \quad (4.24)$$

\otimes in (4.23) denotes the vector product.

Using these vectors, two relevant questions can be answered. First, it is de-

terminated if the point P is in the range of the line segment L . This is the case if P lies between the two parallel dashed lines in the figure and is computationally evaluated as

$$0 \leq \frac{\langle w, v \rangle}{\|w\| \cdot L} \leq 1. \quad (4.25)$$

Here, $\langle \bullet, \bullet \rangle$ denotes the scalar product and $\|\bullet\|$ denotes the vector-2-norm. Note that $\|v\| = L$.

The distance of P to the line L is the projection of the vector w on the vector n . That is,

$$e = \frac{\langle w, n \rangle}{\|w\|}. \quad (4.26)$$

Note that e is positive in the configuration in Fig. 4.16 (a) and negative in the configuration in Fig. 4.16 (b).

Regarding arc segments, we consider a generic arc $\mathcal{A}(C, R, \Psi_s, \Psi_f)$ with the center point C , the radius R , the starting orientation angle Ψ_s and the final orientation angle Ψ_f as shown in Fig. 4.17.

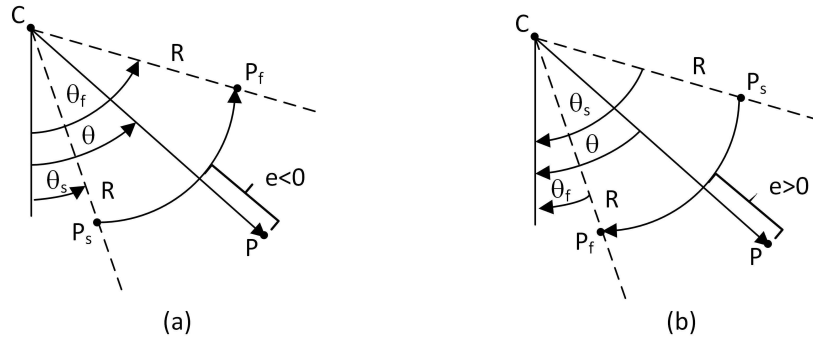


Figure 4.17: Distance error for an arc segment: (a) positive radius; (b) negative radius.

We first evaluate if a point P is in the range of the arc segment \mathcal{A} . That is, it has to be checked if P lies between the dashed lines in Fig. 4.17. This is precisely

the case if the angle θ assumes values between Ψ_s and Ψ_f . Hereby,

$$\Psi = \tan^{-1}(v_y/v_x). \quad (4.27)$$

Using the vector $v = P - C$, we distinguish the two cases $R > 0$ and $R < 0$ as follows (recall that a negative value R indicates a negative change in the orientation angle in our formulation). It holds that $\Psi_s < \Psi_f$ if $R > 0$ and $\Psi_s > \Psi_f$ if $R < 0$. That is, P is in the range of \mathcal{A} if

$$\begin{cases} \Psi_s < \Psi < \Psi_f & \text{if } R > 0 \\ \Psi_f \leq \Psi \leq \Psi_s & \text{if } R < 0. \end{cases} \quad (4.28)$$

Then, the distance error is

$$e = \begin{cases} R - \|v\| & \text{if } R > 0 \\ \|v\| + R & \text{if } R < 0 \end{cases}. \quad (4.29)$$

In summary, (4.26) and (4.29) can both be evaluated by simple arithmetic operations.

4.3.4 Trajectory Prediction

The lane keeping controller in Fig. 4.1 receives the lane change trajectory Y as well as a predicted vehicle trajectory \tilde{Y} from the maneuver computation unit. Although this is not the main focus of the thesis, we next propose a possible representation of \tilde{Y} assuming that Y is given and the vehicle is currently located at a point $P = \begin{bmatrix} X \\ Y \end{bmatrix}$ with the orientation angle Ψ as shown in Fig. 4.18.

Then, \tilde{Y} is computed along the arc-length s starting from P . Considering the closest arc-spline segment C_1 and its successors C_2, \dots , the predicted trajectory is

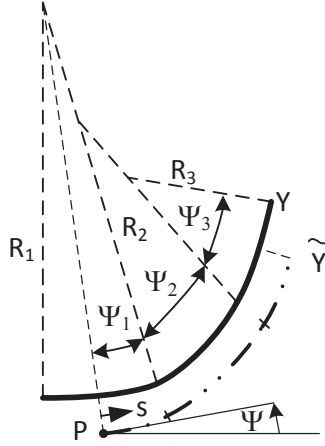


Figure 4.18: Computation of the predicted vehicle trajectory \tilde{Y} .

evaluated as

$$\tilde{Y} = \begin{cases} A_1 = \mathcal{A}(P, \Psi, R_1) & \text{for } s \leq R_1 \cdot \Psi_1 \\ A_2 = \mathcal{A}(P_f(A_1), \Psi + \Psi_1, R_2) & \text{for } R_1 \cdot \Psi_1 \leq s \leq R_1 \cdot \Psi_1 + R_2 \cdot \Psi_2 \\ A_3 = \mathcal{A}(P_f(A_1), \Psi + \Psi_1 + \Psi_2, R_3) & \text{for } R_1 \cdot \Psi_1 + R_2 \cdot \Psi_2 \leq s \leq R_1 \cdot \Psi_1 + R_2 \cdot \Psi_2 + R_3 \cdot \Psi_3 \\ \vdots & \vdots \end{cases} \quad (4.30)$$

There are several advantages of this parametrization. First, it holds that every point on \tilde{Y} has an analytical representation such that distance computations are straightforward as has been shown in Section 4.3.3. Second, the predicted trajectory \tilde{Y} captures the properties of the current vehicle location P , orientation Ψ and the knowledge about the curvature of the future path Y to be followed.

4.4 Approximations of Optimal Control Trajectories

4.4.1 Explanation of the Method

The main aim of this section is the approximation of the optimal control trajectories computed in Section 3.4 by bi-elementary paths. To this end, we develop an

algorithm for finding the relevant parameters k_1 , λ and γ . The algorithm evaluated a grid of parameters for λ and γ and determines the values that constitute the smallest deviation from the actual optimal control trajectory. The candidate sets for λ and γ are given as follows.

- Candidate set for λ : $\Lambda = \{0.2, 0.21, \dots, 0.9\}$
- Candidate set for γ : $\Gamma = \{0.4, 0.41, \dots, 1.0\}$

```

1 Input:  $\Lambda, \Gamma, S, \Delta Y$ 
2 Output:  $\lambda, \gamma, k_1, d_{\min} = \text{Inf}$ 
3 for  $\lambda \in \Lambda$  do
4   for  $\gamma \in \Gamma$  do
5     Solve  $f_2(\alpha) = 0$  with solution  $\alpha^*$  in (4.19)
6     Compute  $k_1 = \frac{2\alpha}{\gamma\lambda S}$ 
7     Compute  $B = \mathcal{B}(S, k_1, \lambda, \gamma)$ 
8     Compute  $O = \mathcal{O}(S, \Delta Y)$ 
9     Compute distance value  $d = \int_0^S (P_B(s) - P_O(s))^2 ds$ 
10    if  $d < d_{\min}$  then
11      Set  $d_{\min} = d, \lambda_{\min} = \lambda, \gamma_{\min} = \gamma, k_{1,\min} = k_1$ 
12    end
13  end
14 return  $\lambda_{\min}, \gamma_{\min}, k_{1,\min}$ 

```

Algorithm 1: Approximation of the optimal control solution.

In the next sections, we apply Algorithm 1 for different choices of the vehicle velocity v .

4.4.2 Comparison for Low Speeds

We first consider small speeds by focusing on $v = 20$. Table 4.1 shows the maximum distance values between the respective optimal control trajectories and their approximations. Note that no trajectories for $S \geq 80$ and $a = -2$ were obtained since the velocity becomes negative. In the remaining cases, it can be seen that the approximation is very tight. Comparably large deviations are only observed for the small arc-length $S = 50$ which seem to be unsuitable for the chosen velocity.

Table 4.1: Maximum distance for the optimal control approximations in cm.

a	-2	-1	0	1	2
$S = 50$	8.4	17.1	12.1	17.6	25.8
$S = 60$	4.4	6.6	4.2	2.6	8.1
$S = 70$	5.5	6.1	6.9	6.9	7.3
$S = 80$	—	4.7	3.5	3.2	6.3
$S = 90$	—	2.2	3.7	5.1	7.1
$S = 100$	—	3.6	2.5	4.4	5.7
$S = 110$	—	13.0	7.0	2.9	4.9
$S = 120$	—	5.5	7.7	2.9	2.4

For illustration, the approximated trajectories for values of $S \in \{50, 60, \dots, 120\}$ and $a_r \in \{-2, -1, 0, 1, 2\}$ are shown in the following figures.

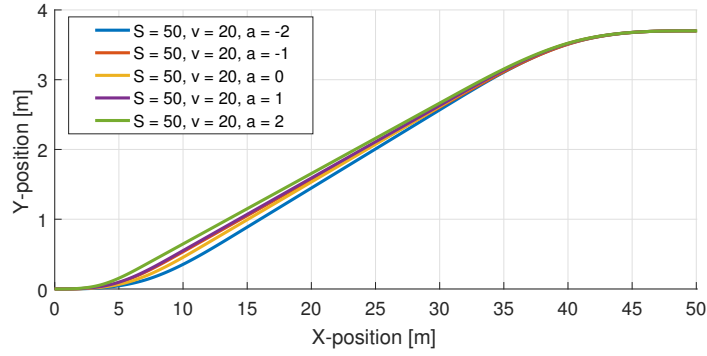


Figure 4.19: Optimal control approximation for $S = 50$, $v = 20$ and different values of a .

In addition, the respective parameter values for the best approximation are listed in Table 4.2.

The main observations from the approximation experiments are summarized as follows. First, it can be seen in Table 4.2 that feasible trajectories cannot be obtained if $S = 50$ is small and the acceleration $a_r = 1, 2$ is large. Here, a very large curvature larger than 0.02 is encountered, which cannot be followed at the designated speed. In order to justify this claim, consider that the maximum possible

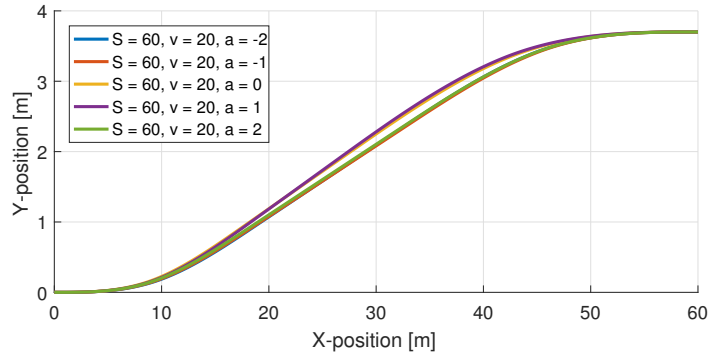


Figure 4.20: Optimal control approximation for $S = 60$, $v = 20$ and different values of a .

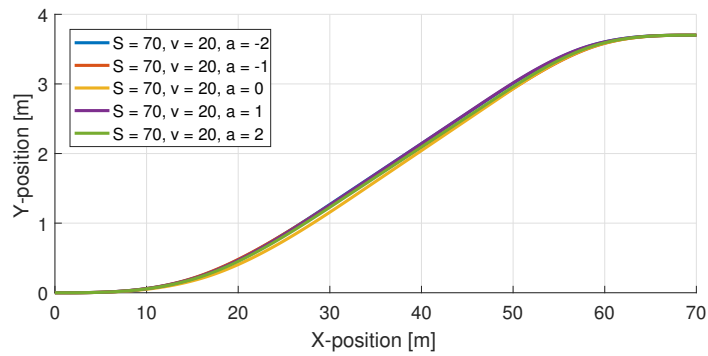


Figure 4.21: Optimal control approximation for $S = 70$, $v = 20$ and different values of a .

curvature at $v = 20$ is given by

$$\mu g/v^2 = 0.82 \cdot 9.81/20^2 = 0.02.$$

It can also be seen that all the other cases lead to feasible trajectories, whereby the parameter values for each specific value of S are similar. It is further interesting to note that short trajectories ($S = 50$ and $S = 60$) require $\lambda < 0.5$ such that the first elementary path is shorter than the second one. All other trajectories have $\lambda > 0.5$. It can also be seen that $\gamma > 0.8$ in most of the cases and the maximum curvature clearly decreases for longer trajectories.

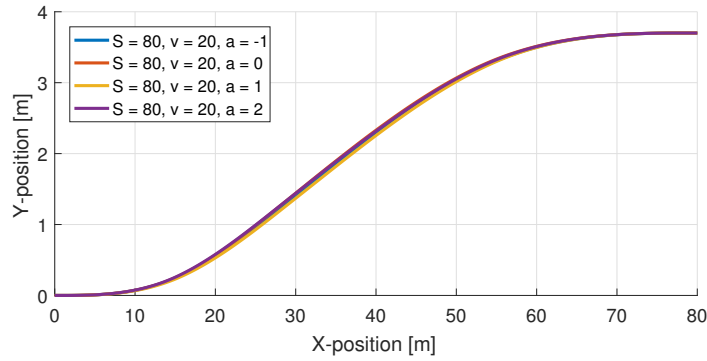


Figure 4.22: Optimal control approximation for $S = 80$, $v = 20$ and different values of a .

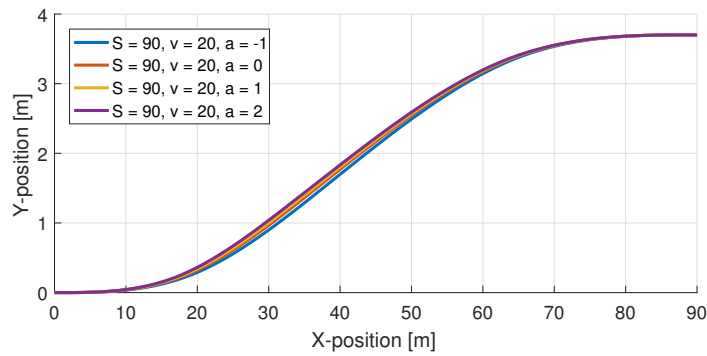


Figure 4.23: Optimal control approximation for $S = 90$, $v = 20$ and different values of a .

For the practical application, the main question is which of the parameter combinations should be chosen for the given velocity of $v = 20$. In principle, a larger value of S leads to a trajectory with a smaller curvature that can be followed more easily by a vehicle. On the other hand, such trajectory leads to a longer duration of the lane change, which is undesirable. In addition, the cost of the trajectory should be low. According to the study in Section 3.4, the lowest cost for $v = 20$ are obtained for $S = 70$. Hence, a choice of $S \approx 70$ is most suitable for this velocity. In addition, it can be seen from Table 4.2 that the maximum curvature should be around 0.009, $\lambda = 0.67$ and $\gamma = 0.84$ when looking at the case of $a = 2$ for the most critical trajectory.

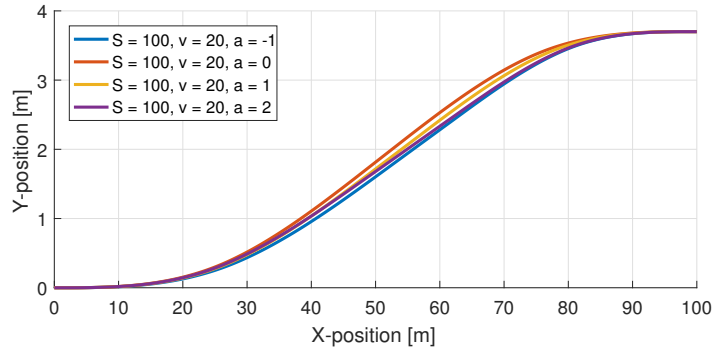


Figure 4.24: Optimal control approximation for $S = 100$, $v = 20$ and different values of a .

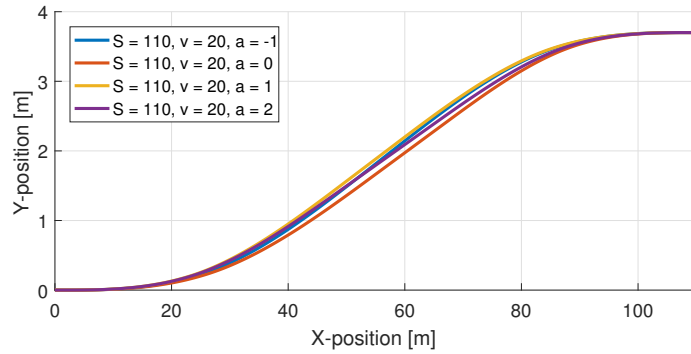


Figure 4.25: Optimal control approximation for $S = 110$, $v = 20$ and different values of a .

Using the choice of $k_1 = 0.004$ and hence $k_2 = 0.009$, $\lambda = 0.67$ and $\gamma = 0.84$, we next perform simulation experiments for $v = 20$ and $a_r = -2, -1, 0, 1, 2$. The simulation results are presented in Fig. 4.27 to 4.31. In these experiments, the lane-keeping controller from [63] is used.

It is interesting to observe that the trajectories and input signals are very similar. In addition, it holds that the trajectories for $a_r = -2, -1$ are followed slightly slower compared to the optimal control trajectory due to the choice of the trajectory parameters. Slightly larger deviations are observed for the case of large accelerations. It can also be seen from Table 4.3 that the control cost is only slightly larger when using trajectory following. This difference can also be con-

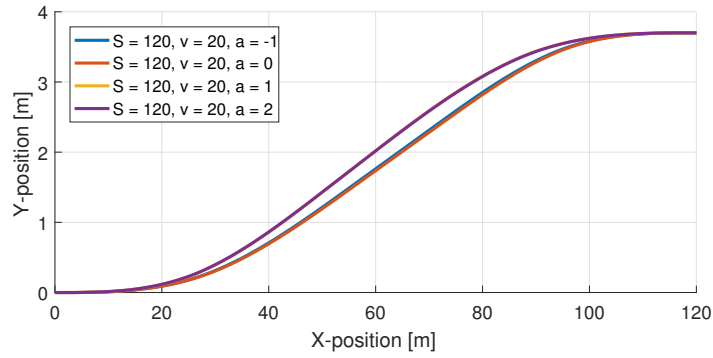


Figure 4.26: Optimal control approximation for $S = 120$, $v = 20$ and different values of a .

Table 4.2: Parameters (k_1, λ, γ) for the optimal control approximations.

a	-2	-1	0	1	2
$S = 50$	(0.016,0.42,0.68)	(0.021,0.34,0.57)	(0.019,0.37,0.63)	(0.022,0.33,0.58)	(0.028,0.27,0.54)
$S = 60$	(0.011,0.4,0.79)	(0.011,0.4,0.77)	(0.012,0.35,0.84)	(0.012,0.35,0.88)	(0.011,0.39,0.77)
$S = 70$	(0.012,0.74,0.77)	(0.008,0.60,0.82)	(0.008,0.62,0.83)	(0.009,0.65,0.79)	(0.009,0.67,0.84)
$S = 80$	(0.006,0.6,0.89)	(0.006,0.63,0.85)	(0.006,0.62,0.90)	(0.006,0.63,0.83)	(0.006,0.64,0.83)
$S = 90$	(0.004,0.59,0.9)	(0.006,0.68,0.92)	(0.005,0.64,0.81)	(0.005,0.63,0.8)	(0.005,0.61,0.79)
$S = 100$	(0.003,0.56,0.9)	(0.004,0.63,0.83)	(0.004,0.66,0.91)	(0.004,0.6,0.8)	(0.005,0.71,0.8)
$S = 110$	(0.003,0.57,0.91)	(0.003,0.57,0.88)	(0.003,0.56,0.89)	(0.003,0.57,0.85)	(0.004,0.7,0.8)
$S = 120$	(0.002,0.5,0.99)	(0.002,0.53,0.88)	(0.002,0.54,0.87)	0.002,0.45,0.96)	(0.002,0.45,0.95)

cluded from Fig. 4.27 to 4.31 when inspecting the steering angle δ .

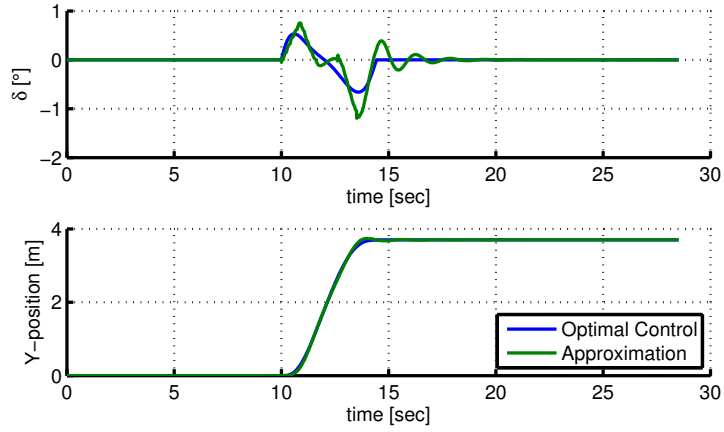


Figure 4.27: Trajectory following for $v = 20$ and $a_r = -2$.

Table 4.3: Comparison of the optimal cost for the gradient method and the cost of trajectory following ($\cdot 10^{-3}$)

a_r	-2	-1	1	0	2
gradient	0.22	0.16	0.12	0.12	0.10
following	0.38	0.25	0.18	0.14	0.12

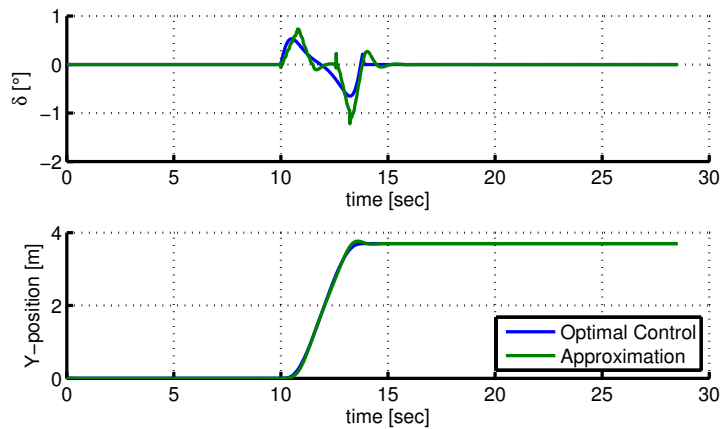


Figure 4.28: Trajectory following for $v = 20$ and $a_r = -1$.

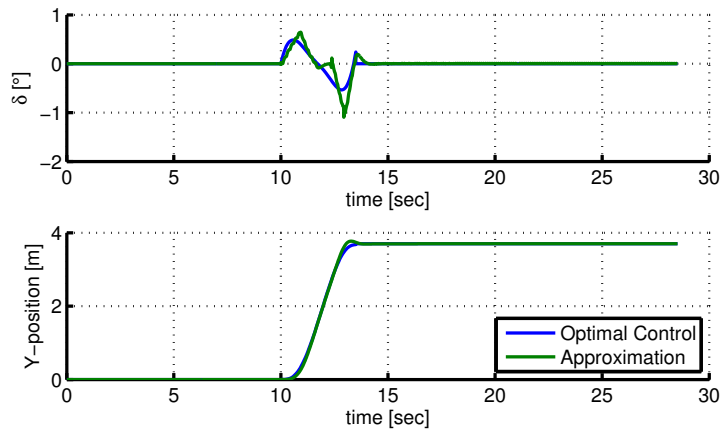


Figure 4.29: Trajectory following for $v = 20$ and $a_r = 0$.

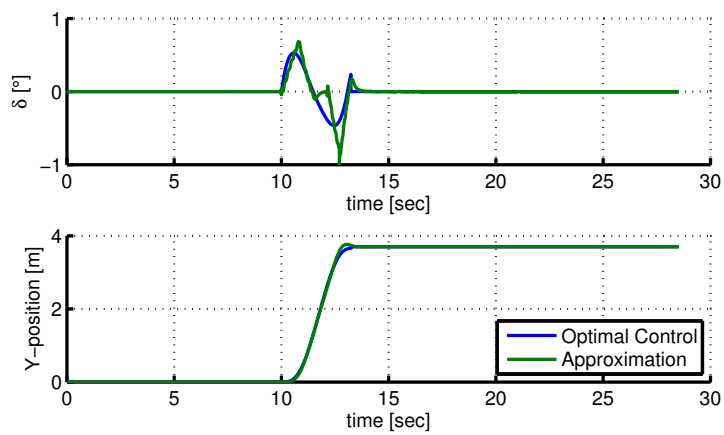


Figure 4.30: Trajectory following for $v = 20$ and $a_r = 1$.

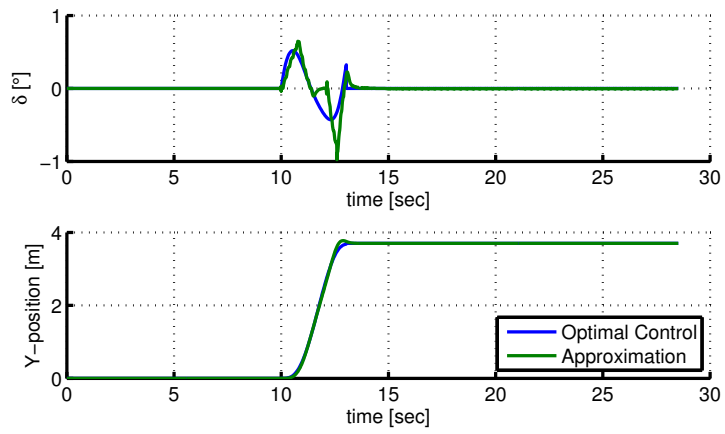


Figure 4.31: Trajectory following for $v = 20$ and $a_r = 2$.

4.4.3 Comparison for High Speeds

We next perform the same comparison as in Section 4.4.2 for a large velocity of $v = 40$. We first evaluate the optimal control approximation according to Algorithm 1. Table 4.4 shows the maximum distance values between the respective optimal control trajectories and their approximations.

Table 4.4: Maximum distance for the optimal control approximations in cm.

a	-2	-1	0	1	2
$S = 70$	12.8	11.7	11.0	10.5	9.6
$S = 80$	10.1	12.9	10.5	16.2	13.9
$S = 90$	8.4	16.5	10.7	9.7	11.1
$S = 100$	9.4	8.2	5.6	12.0	11.3
$S = 110$	6.6	8.2	10.0	11.7	10.1
$S = 120$	6.9	7.8	8.1	10.1	12.7

For illustration, the approximated optimal control trajectories are shown in Fig. 4.32 to 4.37.

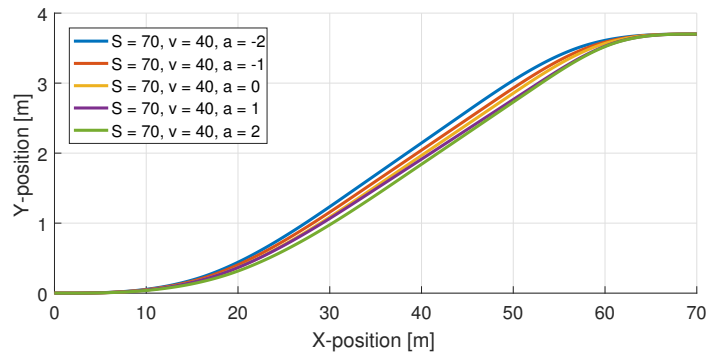


Figure 4.32: Optimal control approximation for $S = 70$, $v = 40$ and different values of a .

In addition, the respective parameter values for the best approximation are listed in Table 4.5.

The main observations from the approximation experiments for $v = 40$ are as follows. First, we determine the maximum curvature that leads to feasible

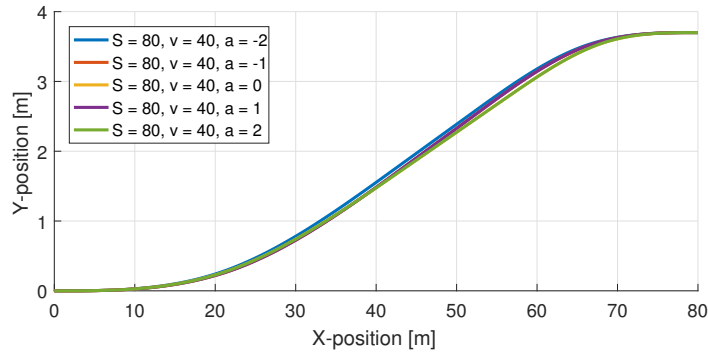


Figure 4.33: Optimal control approximation for $S = 80$, $v = 40$ and different values of a .

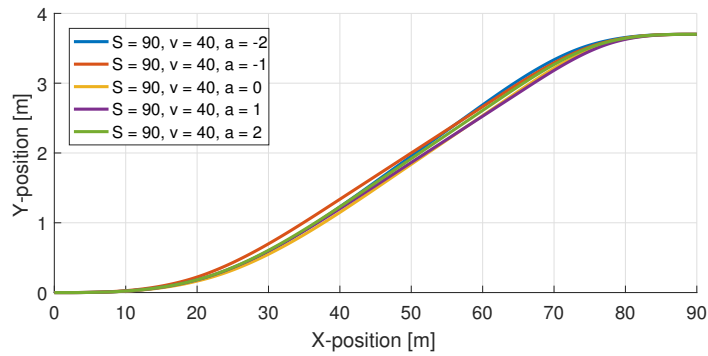


Figure 4.34: Optimal control approximation for $S = 90$, $v = 40$ and different values of a .

trajectories at $v = 40$ as

$$\mu g/v^2 = 0.82 \cdot 9.81/40^2 = 0.005.$$

That is, the minimum possible arc-length is $S = 90$, whereas the trajectories for $S = 70$ and $S = 80$ are at the limit of feasible driving.

For the practical application, the main question is which of the parameter combinations should be chosen for the given velocity of $v = 40$. Similar to the previous section, we consider that a larger value of S leads to a trajectory with a smaller curvature that can be followed more easily by a vehicle. On the other hand, such

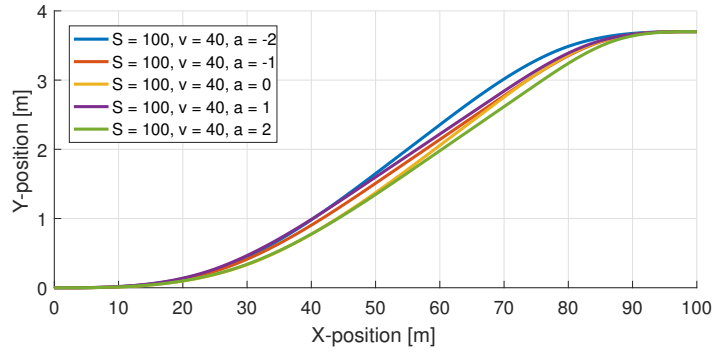


Figure 4.35: Optimal control approximation for $S = 100$, $v = 40$ and different values of a .

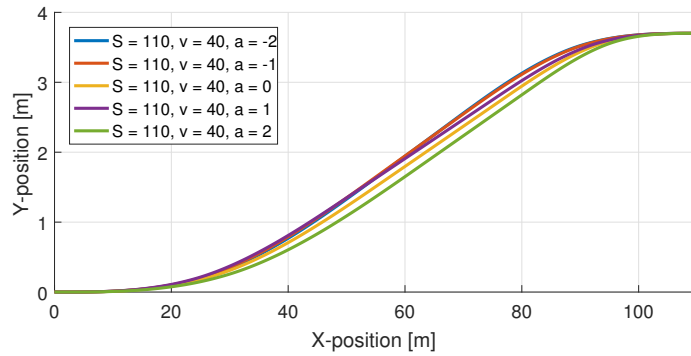


Figure 4.36: Optimal control approximation for $S = 110$, $v = 40$ and different values of a .

trajectory leads to a longer duration of the lane change, which is undesirable. In addition, the cost of the trajectory should be low. According to the study in Section 3.4, trajectories with a low cost for $v = 40$ are already obtained for $S = 90$. Hence, a choice of $S \approx 90$ is suitable for this velocity. In addition, it can be seen from Table 4.2 that the maximum curvature should be around 0.005, $\lambda = 0.61$ and $\gamma = 0.81$ when looking at the case of $a = 2$ for the most critical trajectory.

Using the choice of $k_1 = 0.0032$ and hence $k_2 = 0.005$, $\lambda = 0.61$ and $\gamma = 0.81$, we next perform simulation experiments for $v = 40$ and $a_r = -2, -1, 0, 1, 2$. The simulation results are presented in Fig. 4.38 to 4.42. In these experiments, the lane-keeping controller from [63] is used.

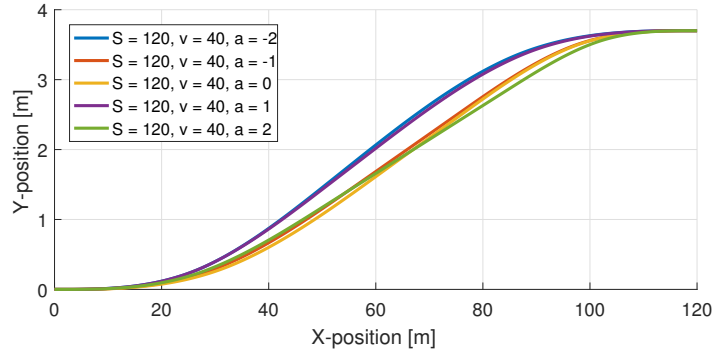


Figure 4.37: Optimal control approximation for $S = 120$, $v = 40$ and different values of a .

Table 4.5: Parameters (k_1, λ, γ) for the optimal control approximations.

a	-2	-1	0	1	2
$S = 70$	(0.007,0.56,0.84)	(0.008,0.6,0.81)	(0.009,0.63,0.81)	(0.009,0.66,0.76)	(0.01,0.66,0.76)
$S = 80$	(0.006,0.6,0.89)	(0.006,0.62,0.91)	(0.007,0.64,0.84)	(0.006,0.62,0.91)	(0.007,0.64,0.84)
$S = 90$	(0.005,0.59,0.88)	(0.005,0.58,0.76)	(0.005,0.64,0.82)	(0.005,0.64,0.76)	(0.005,0.61,0.81)
$S = 100$	(0.003,0.56,0.95)	(0.004,0.63,0.83)	(0.004,0.65,0.94)	(0.004,0.6,0.81)	(0.005,0.69,0.84)
$S = 110$	(0.003,0.57,0.91)	(0.003,0.57,0.88)	(0.003,0.63,0.83)	(0.003,0.59,0.8)	(0.04,0.68,0.85)
$S = 120$	(0.002,0.44,0.99)	(0.002,0.56,0.85)	(0.003,0.58,0.89)	(0.002,0.45,0.95)	(0.003,0.59,0.73)

Similar to Section 4.4.2, the trajectories and input signals are very similar. In addition, it can be observed that slightly larger deviations are observed for the case of large accelerations. It can also be seen from Table 4.3 that the control cost is not significantly larger when using trajectory following.

Table 4.6: Comparison of the optimal cost for the gradient method and the cost of trajectory following for $v = 40$

a_r	-2	-1	1	0	2
gradient	0.04	0.05	0.04	0.04	0.04
following	0.06	0.07	0.06	0.06	0.07

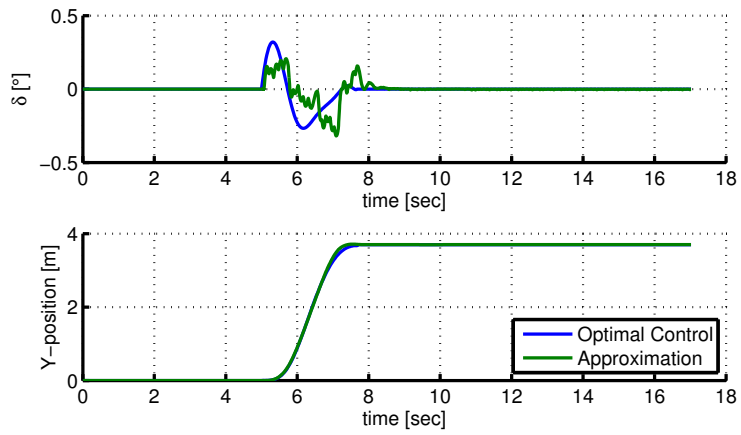


Figure 4.38: Trajectory following for $v = 40$ and $a_r = -2$.

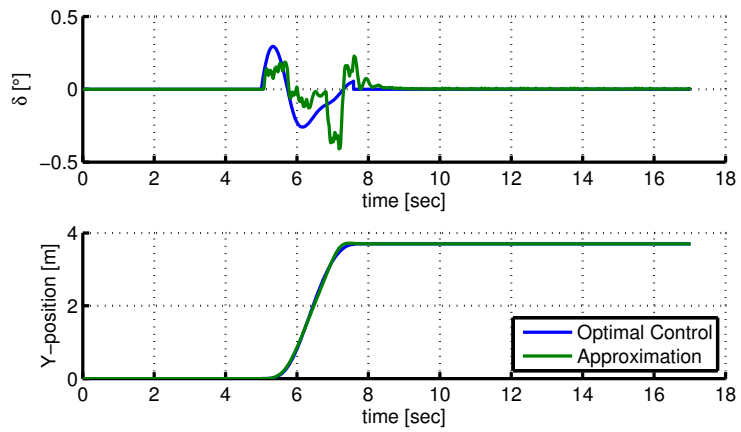


Figure 4.39: Trajectory following for $v = 40$ and $a_r = -1$.

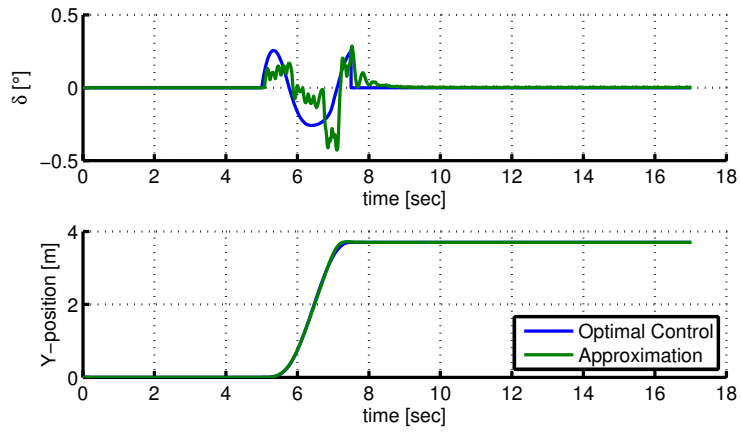


Figure 4.40: Trajectory following for $v = 40$ and $a_r = 0$.

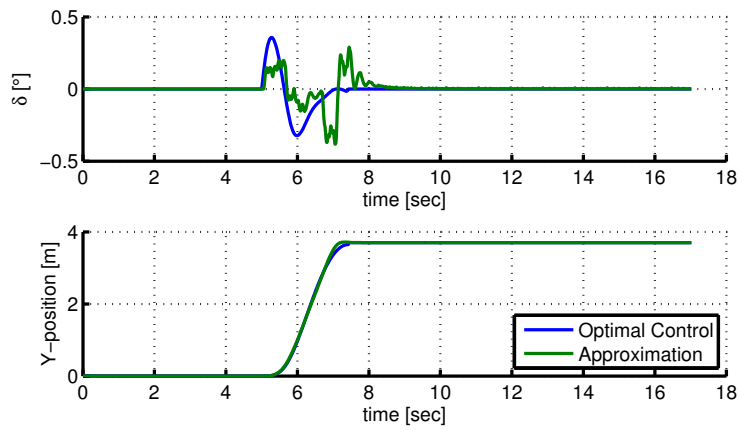


Figure 4.41: Trajectory following for $v = 40$ and $a_r = 1$.

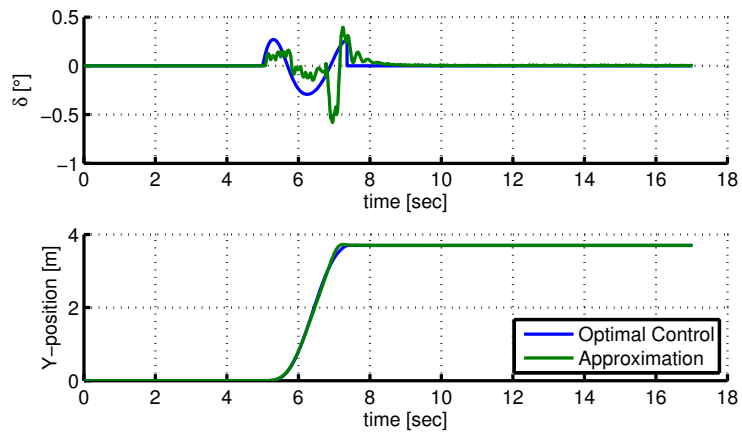


Figure 4.42: Trajectory following for $v = 40$ and $a_r = 2$.

CHAPTER 5

Application Examples Using Approximated Trajectories

The previous thesis study considered the decoupling of the longitudinal and lateral vehicle motion and the arc-length representation of the vehicle model in Section 3.2, the optimal control computations in Section 3.3 and 3.4, as well as the computation of optimal control approximations using arc-splines in Section 4.4. This chapter uses the previous results for three driving applications. First, Section 5.1 considers the efficient parameter selection for bi-elementary paths for lane changes. Second, Section 5.2 shows how the developed arc-spline representation of road trajectories can be used for lane keeping. Finally, Section 5.3 develops a method for safe and comfortable vehicle following on curved roads using a combination of the decoupling strategy in Section 3.2 and cooperative adaptive cruise control (CACC).

5.1 Parameter Selection for Bi-elementary Paths

5.1.1 Computational Method

The method presented in the previous section enables the efficient computation of bi-elementary paths assuming that the relevant parameters such as k_1 , λ and γ are already given. The remaining question is the selection of these parameters depending on the driving situation. Qualitatively, it holds that small curvature values (and hence long trajectories) should be chosen at large speeds and/or accelerations, whereas large curvature values (short trajectories) can be tolerated at small velocities. In the sequel, we develop a method for selecting the relevant parameters based on a characterization of the maximum possible curvature for a

given velocity/acceleration profile.

To this end, we assume that the *entry velocity* of a lane change is v_0 and the maximum acceleration during a lane change is a_{\max} . In practice, the entry velocity is the current vehicle velocity when initiating a lane change and hence available. In addition, a_{\max} is determined by the limits for comfortable driving which are in the order of $a_{\max} = 2 \text{ m/sec}^2$ [64, 65, 66]. Using v_0 and a_{\max} , the maximum velocity profile during a lane change is given by

$$v(t) = v_0 + a_{\max} t \quad (5.1)$$

and the corresponding arc-length is computed as

$$s(t) = v_0 t + \frac{1}{2} a_{\max} t^2. \quad (5.2)$$

Since bi-elementary paths are formulated depending on the arc-length parameter s , we next write the maximum velocity profile in terms of the arc-length as

$$t(s) = \frac{1}{a_{\max}} (-v_0 + \sqrt{v_0^2 + 2a_{\max} s}), \quad (5.3)$$

$$v_{\max}(s) = v_0 + a_{\max} t(s) = v_0 - v_0 + \sqrt{v_0^2 + 2a_{\max} s} = \sqrt{v_0^2 + 2a_{\max} s}. \quad (5.4)$$

It is now possible to establish a relation between the maximum velocity profile in (5.4) and the maximum feasible curvature based on the well-established friction circle [67]. Assuming a point mass vehicle model as in [60], it must hold that

$$a_{\text{long}}^2 + a_{\text{lat}}^2 \leq \mu^2 g^2, \quad (5.5)$$

whereby, a_{long} is the longitudinal vehicle acceleration, a_{lat} is the lateral vehicle acceleration, μ is the friction coefficient of the road and g is the gravity constant. Moreover, the lateral acceleration on a curved road with radius R and curvature

$k = 1/R$ depends on the longitudinal velocity $v(s)$ via

$$a_{\text{lat}}(s) = \frac{v(s)^2}{R} = v(s)^2 \cdot k. \quad (5.6)$$

Respecting that $a_{\text{long}} \leq a_{\text{max}}$, the maximum curvature profile is derived as

$$k_{\text{max}}(s) = \frac{\sqrt{\mu^2 \cdot g^2 - a_{\text{max}}^2}}{v_{\text{max}}^2(s)} = \frac{\sqrt{\mu^2 \cdot g^2 - a_{\text{max}}^2}}{v_0^2 + 2 a_{\text{max}} s} \quad (5.7)$$

In words, any lane change trajectory with a curvature, whose absolute value at each arc-length s remains below $k_{\text{max}}(s)$ can be taken by vehicles that enter the lane change with velocity v_0 and whose acceleration is bounded by a_{max} . Moreover, in view of the previous discussion on lane change trajectories in Section 3.2, it is desired to find a shortest possible bi-elementary path with a curvature that is bounded by $k_{\text{max}}(s)$.

Consider a generic bi-elementary path $\mathcal{B}(S, k_1, \lambda, \gamma)$. According to Fig. 4.4, the maximum curvature is reached at $s = \lambda \gamma S/2$ with a curvature value k_1 and at $s = S - (1 - \lambda) \gamma S/2$ with a curvature value $k_2 = -\lambda/(1 - \lambda) k_1$. In order to determine a bi-elementary path with the shortest arc-length (and hence largest curvature), it is required to achieve

$$k_1 = k_{\text{max}}(\lambda \gamma S/2) \text{ and } k_2 = -\lambda/(1 - \lambda) k_1 = -k_{\text{max}}(S - (1 - \lambda) \gamma S/2). \quad (5.8)$$

Substituting (5.8) into (5.7), it follows that

$$k_{\text{max}}(s_2) = \frac{\lambda}{1 - \lambda} k_{\text{max}}(s_1) \quad (5.9)$$

$$\Rightarrow \frac{\sqrt{\mu^2 \cdot g^2 - a_{\text{max}}^2}}{v_0^2 + 2 a (S - (1 - \lambda) \gamma S/2)} = \frac{\lambda}{1 - \lambda} \frac{\sqrt{\mu^2 \cdot g^2 - a_{\text{max}}^2}}{v_0^2 + 2 a \lambda \gamma S/2} \quad (5.10)$$

This equation can be solved for λ and the corresponding value of k_1 follows from

(5.8).

$$\begin{aligned}\lambda_{\max} &= f_{\lambda}(S) \\ &= -\frac{(S a_{\max} - \sqrt{S^2 a_{\max}^2 \gamma^2 - 2 S^2 a_{\max}^2 \gamma + S^2 a_{\max}^2 + 2 S a_{\max} v_0^2 + v_0^4 + v_0^2} - S a_{\max} \gamma)}{2 S a_{\max} \gamma}\end{aligned}\quad (5.11)$$

$$k_{1,\max} = f_{k_1}(S, \lambda) = \frac{\sqrt{g^2 \cdot \mu^2 - a_{\max}^2}}{v_0^2 + S \cdot a_{\max} \cdot \gamma \cdot \lambda}.\quad (5.12)$$

That is, (5.11) and (5.12) must be fulfilled in order to achieve the maximum feasible curvature. In addition, (4.18) must be ensured to obtain the desired lane width ΔY . In the sequel, we reformulate (4.18) in terms of the arc-length S by substituting $\alpha = \frac{\lambda \gamma k_1 S}{2}$. Accordingly, it must hold that

$$f_S(S, k_1, \lambda, \gamma) = S \left(\gamma \hat{D} \left(\frac{\lambda \gamma k_1 S}{2} \right) \sin \left(\frac{\lambda \gamma k_1 S}{4} \right) + (1 - \gamma) \sin \left(\frac{\lambda \gamma k_1 S}{2} \right) \right) - \Delta Y = 0.\quad (5.13)$$

Substituting (5.11) and (5.12) into (5.13), we must solve

$$f_S(S, f_{k_1}(S, f_{\lambda}(S)), f_{\lambda}(S), \gamma) = 0\quad (5.14)$$

in order to obtain a bi-elementary path with the maximum possible curvature. Theorem 3 states that a unique solution of (5.14) can be obtained using the Newton iteration in (4.20).

Theorem 3. *Consider that $S \in [0, 500]$, $0.3 \leq \gamma \leq 1$ and $0 < \Delta Y \leq 10$. Then, the nonlinear equation in (5.14) has a unique solution S^* that can be computed by the Newton iteration in (4.20) with the initial value $S_0 = 500$.*

Proof. In order to prove Theorem 3 we show that (5.14) fulfills the conditions in Proposition 2. For each value of γ , we consider the function $f(S) = f_S(S, \gamma)$ in

(5.14). Inspecting (5.13), it holds that $f_S(S, \gamma)$ can be written as

$$f_S(S, \gamma) = g_S(S, \gamma) - \Delta Y.$$

The function $g_S(S, \gamma)$ is shown for different values of γ , a_{max} , v_0 and μ in Fig. 5.1.

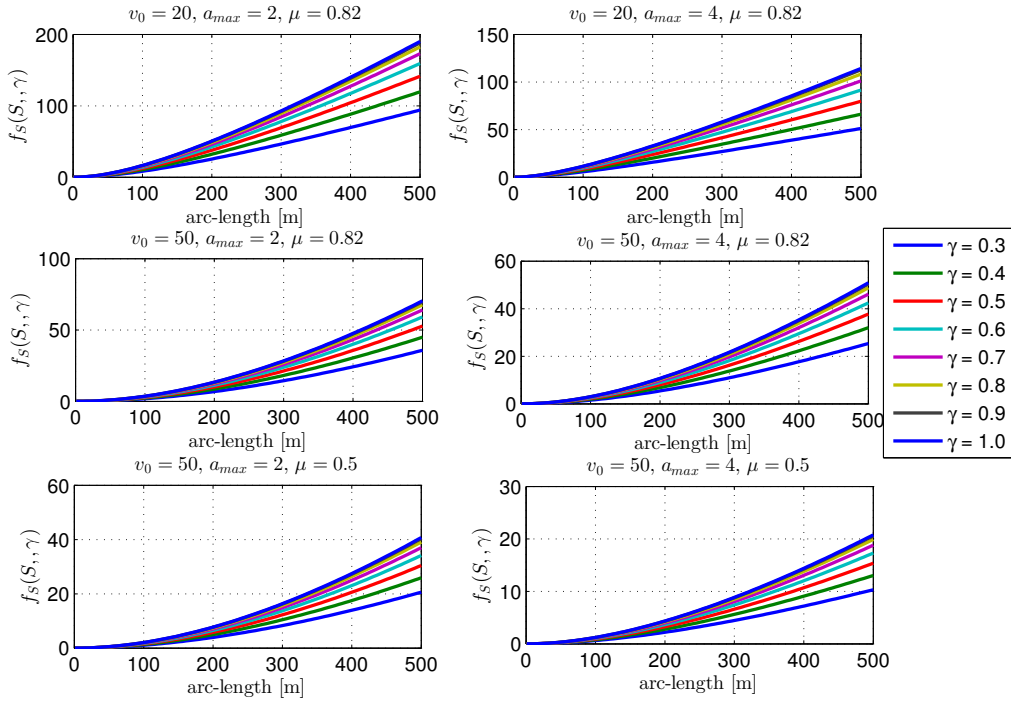


Figure 5.1: Evaluation of f_S in (5.14) for different values of γ .

Focusing on the interval $[a, b] = [0, 500]$ for S , it is readily observed that $g_S(a, \gamma) = g_S(0, \gamma) = 0$ for all $\gamma \in [0.3, 1]$ and $g_S(b) = g_1(500) \geq 10.32$. In order to apply Proposition 2 1), it must hold that $f_S(a, \gamma) < 0$ and $f_S(b, \gamma) > 0$. Considering that $f_S(S, \gamma) = g_S(S, \gamma) - \Delta Y$ and $\Delta Y > 0$, it is clear that

$$f_S(a, \gamma) = f_S(0, \gamma) = g_S(0, \gamma) - \Delta Y = -\Delta Y < 0.$$

Similarly, it is confirmed that

$$f_S(b, \gamma) = f_S(500, \gamma) = g_S(500, \gamma) - \Delta Y > 10.32 - 10 > 0.$$

Hence, condition 1) in Proposition 2 is fulfilled.

In addition, it holds that

$$f'_S(S, \gamma) = g'_S(S, \gamma) > 0$$

for all values of $\gamma \in [0.3, 1]$ and $f''_S(S, \gamma) = g''_S(S, \gamma)$ is always positive for $S \in [0, 500]$ as can be verified by Fig. 5.1. Hence, condition 2) and 3) in Proposition 2 are also true.

Since it is assumed that only arc-lengths in the interval $[0, 500]$ are suitable for lane changes, it suffices to choose $S_0 = 500$ in order to fulfill all conditions in Proposition 2. \square

We again note that the parameter intervals in Theorem 3 are chosen according to practical considerations. First, the same values for ΔY as in Section 4.2.3 are assumed. Second, the values for γ are selected based on the fact that smaller values of γ lead to very long bi-elementary paths as was already observed in Fig. 4.10. In addition, it will be further highlighted in Section 5.1.2 that small values for γ are not suitable for lane change trajectories.

In summary, this section develops a straightforward procedure for selecting the parameters of a bi-elementary lane change path for a given entry velocity v_0 , maximum acceleration a_{\max} and shape parameter γ . The steps of the procedure are listed as follows.

1. Determine the solution S^* of (5.14) using the Newton method
2. Compute $\lambda^* = f_\lambda(S^*)$ from (5.11) and $k_1^* = f_{k_1}(S^*, \lambda^*)$ from (5.12).
3. Evaluate the desired bi-elementary path as $\mathcal{B}(S^*, k_1^*, \lambda^*, \gamma)$.

The resulting bi-elementary path is the shortest path for a given value of γ that fulfills the curvature constraint in (5.7) for all possible velocity profiles that start

from the entry velocity v_0 and that meet the acceleration constraint a_{\max} . A suitable choice for the parameter γ will be discussed in the subsequent section.

5.1.2 Trajectory Examples

In this section, we validate the proposed method by several examples. We consider different friction coefficients $\mu = 0.82$ (dry asphalt) and $\mu = 0.5$ (wet asphalt) and accelerations up to 5 m/sec^2 . Considering that accelerations below $a = 2 \text{ m/sec}^2$ are considered as comfortable [64, 65, 66], $a_{\max} = 5 \text{ m/sec}^2$ is selected as a case with a large acceleration.

In the first example, the entry velocity is $v_0 = 20 \text{ m/sec}$, the friction coefficient is $\mu = 0.82$ (which corresponds to dry road) and $\gamma = 1$. Fig. 5.2 shows the computed bi-elementary path (upper part) and its curvature $k(s)$ with the corresponding maximum curvature $k_{\max}(s)$ (lower part) for different maximum accelerations. It is readily observed that the bi-elementary paths are computed such that the curvature constraint $k_{\max}(s)$ is met. In accordance with (5.11) and (5.12), $k(s)$ equals k_{\max} at the two points of maximum curvature such that there is no feasible shorter bi-elementary path. Comparing the different accelerations, it is clear that larger accelerations require a longer arc-length due to the reduced maximum curvature.

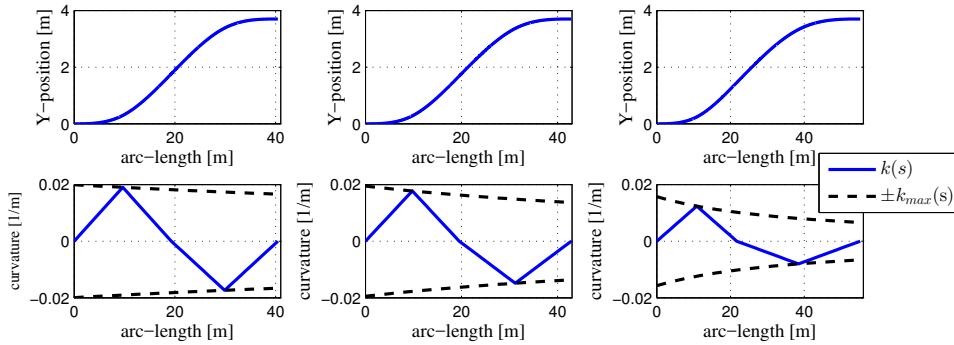


Figure 5.2: Trajectory computation for $v_0 = 20 \text{ m/sec}$, $\gamma = 1$, $\mu = 0.82$ and $a_{\max} = 1 \text{ m/sec}^2$ (left), $a_{\max} = 2 \text{ m/sec}^2$ (middle) and $a_{\max} = 5 \text{ m/sec}^2$ (right).

Fig. 5.3 considers the same case as Fig. 5.2 with the difference that the entry velocity $v_0 = 40 \text{ m/sec}$ is increased. Since a larger entry-velocity implies a reduced

maximum curvature in (5.7), the bi-elementary paths in this case are considerably longer compared to the ones in Fig. 5.2.

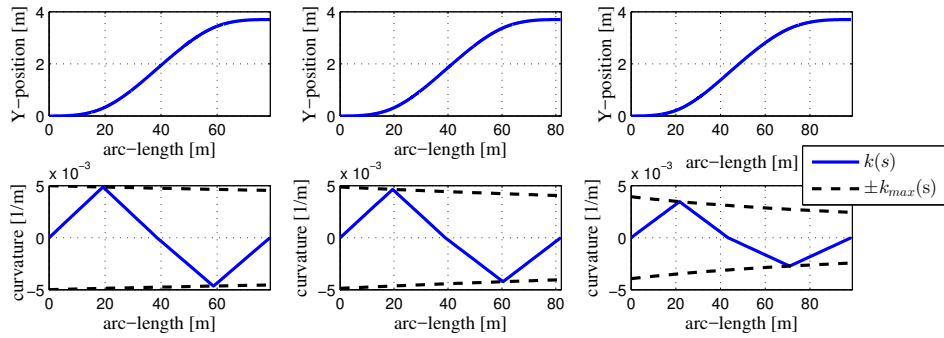


Figure 5.3: Trajectory computation for $v_0 = 40 \text{ m/sec}$, $\gamma = 1$, $\mu = 0.82$ and $a_{\max} = 1 \text{ m/sec}^2$ (left), $a_{\max} = 2 \text{ m/sec}^2$ (middle) and $a_{\max} = 5 \text{ m/sec}^2$ (right).

Fig. 5.4 repeats the experiment in Fig. 5.2 with a reduced friction coefficient $\mu = 0.5$. It can again be seen that the resulting bi-elementary paths perform the lane change with the smallest possible arc-length, whereby the arc-length is increased compared to Fig. 5.2. In particular, it turns out that an acceleration of $a_{\max} = 5 \text{ m/sec}^2$ is not tolerable in this case. Fig. 5.4 shows the computation for $a = 4 \text{ m/sec}^2$ because of this reason.

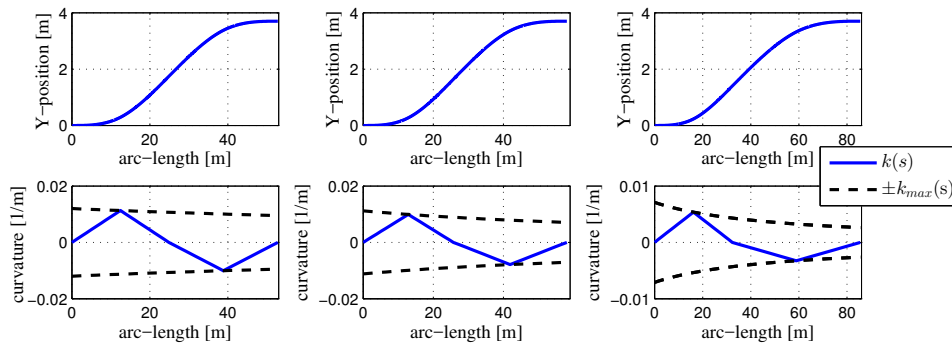


Figure 5.4: Trajectory computation for $v_0 = 20 \text{ m/sec}$, $\gamma = 1$, $\mu = 0.5$ and $a_{\max} = 1 \text{ m/sec}^2$ (left), $a_{\max} = 2 \text{ m/sec}^2$ (middle) and $a_{\max} = 4 \text{ m/sec}^2$ (right).

The previous examples are evaluated for $\gamma = 1$, that is, there is no straight line

segment in the resulting bi-elementary paths. We next study the effect of changing γ using $v_0 = 20$ m/sec, $a_{\max} = 2$ m/sec² and $\mu = 0.82$. The resulting bi-elementary paths are shown in Fig. 5.5. It is clear from this experiment that smaller values of γ lead to longer trajectories. This effect is mainly caused by the usage of a non-zero curvature during a shorter fraction of the overall arc-length when γ is decreased. We note that the same effect was observed for all experiments with different values of v_0 , μ , a_{\max} and ΔY . An analytical evaluation of this observation is not in the scope of this thesis.

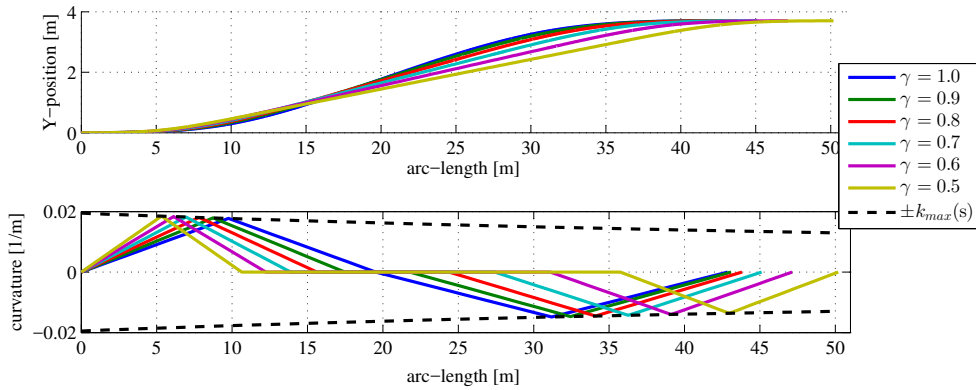


Figure 5.5: Trajectory computation for $v_0 = 20$ m/sec, $\mu = 0.82$ and $a_{\max} = 2$ m/sec² and different values of γ .

In summary, the evaluation in this section shows that the proposed parameter selection method in Section 5.1.1 indeed determines bi-elementary paths for lane changes with the shortest possible arc-length, while meeting the imposed curvature constraints. Considering that the shortest lane change trajectory was obtained for $\gamma = 1$, it is suggested to apply the proposed method for this value of γ . It is finally pointed out that the proposed parameter selection method can be applied in real-time. It is only required to solve (5.13), which can be done using the Newton method with a limited number of iterations. In all our experiments, a solution of (5.13) for $\varepsilon = 10^{-8}$ (which corresponds to a precision of 1 μ m) could be obtained within not more than 15 iterations.

5.1.3 Realization and Evaluation

The lane change trajectories in Section 5.1.1 were computed based on the maximum curvature evaluation in (5.7), which is based on a point mass vehicle model. This section validates the suitability of the computed trajectories using the control architecture in Fig. 4.1 with the vehicle model in Section 2.1.3.

We first consider the case of dry roads such that $\mu = 0.82$. We perform simulation experiments in the control architecture in Fig. 4.1. Lateral control is realized by the lane keeping method in [63] and the traction force F_{f} is computed such that the desired acceleration profile for each experiment is achieved. In each experiment, the vehicle performs a lane change after traveling 50 m on a straight road and continues driving on that road after the lane change until the X -position reaches 250 m. The lane width of 3.7 m is chosen if not stated otherwise. Following the discussion in Section 5.1.2, the value $\gamma = 1$ is used.

In the first experiment, the entry velocity is $v_0 = 20$ m/sec and the maximum acceleration is $a_{\text{max}} = 2$ m/sec². In this case, a trajectory with $\lambda^* = 0.46$, $k_1^* = 0.018$ $S^* = 42.86$ m is computed. Fig. 5.10 shows the simulation result. In the upper plot, the reference trajectory is compared to the actual vehicle trajectory and the lower plot shows the acceleration bound μg as well as the applied longitudinal acceleration a_{long} and the overall acceleration $\sqrt{a_{\text{long}}^2 + a_{\text{lat}}^2}$. It is readily observed that the vehicle is able to follow the reference trajectory with a small error. This is due to the fact that the reference trajectory is computed respecting the constraint in (5.7) on the maximum curvature. As a result, the overall acceleration does not exceed the acceleration bound as can be seen in the lower part of Fig. 5.6.

Fig. 5.7 shows the simulation result for $v_0 = 20$ m/sec and $a_{\text{max}} = 4$ m/sec². In this case a longer lane change trajectory with $\lambda^* = 0.42$, $k_1^* = 0.015$ and $S^* = 49.74$ is obtained due to the increased maximum acceleration. Again, it is the case that the vehicle can follow the computed reference trajectory.

Similarly, Fig. 5.8 shows the case of an increased entry velocity $v_0 = 40$ m/sec and $a_{\text{max}} = 2$ m/sec². The resulting parameters are $\lambda^* = 0.48$, $k_1^* = 0.005$ and $S^* = 81.80$. It is again observed that the lateral acceleration stays below the computed maximum acceleration such that the vehicle can follow the reference trajectory.

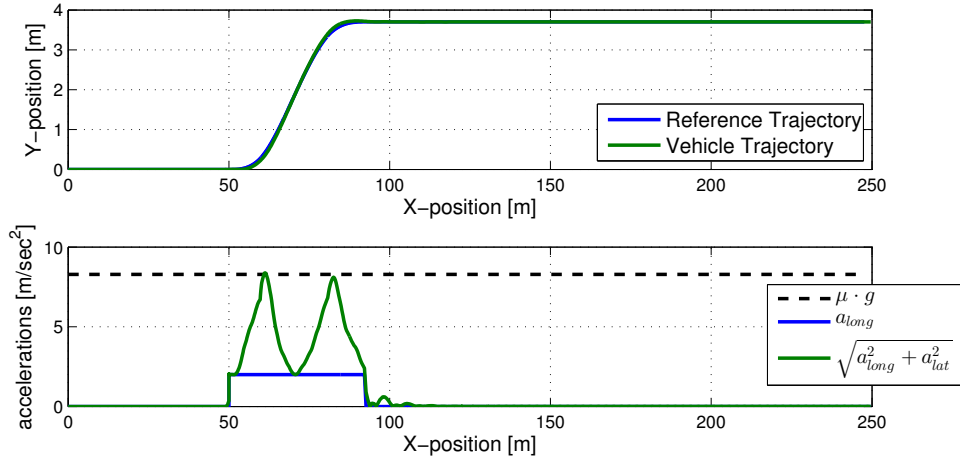


Figure 5.6: Trajectory following for $v_0 = 20$ m/sec, $a_{\max} = 2$ m/sec², $\mu = 0.82$ and $\Delta Y = 3.7$ m.

The last experiment in this section is concerned with the case of a double lane change with $\Delta Y = 7.4$ m at $v_0 = 20$ m/sec and $a_{\max} = 2$ m/sec². The resulting parameter values are $\lambda^* = 0.44$, $k_1^* = 0.017$ and $S^* = 62.94$ m. Fig. 5.9 shows that the computed reference trajectory is suitable for vehicle following.

We next consider the same type of experiment for the case of wet roads. That is, $\mu = 0.5$. Fig. 5.10 displays the case of $v_0 = 20$ m/sec and $a_{\max} = 2$ m/sec² with the parameter values $\lambda^* = 0.44$, $k_1^* = 0.01$ and $S^* = 58.08$ m. Fig. 5.11 shows the case of $v_0 = 40$ m/sec and $a_{\max} = 2$ m/sec² with the parameter values $\lambda^* = 0.47$, $k_1^* = 0.003$ and $S^* = 109.47$ m. In comparison to the case of dry roads, it is observed that the computed trajectories are longer. This is expected to the reduced available lateral force. In addition, both figures show that the computed trajectories are suitable for vehicle following and the acceleration bound is always met.

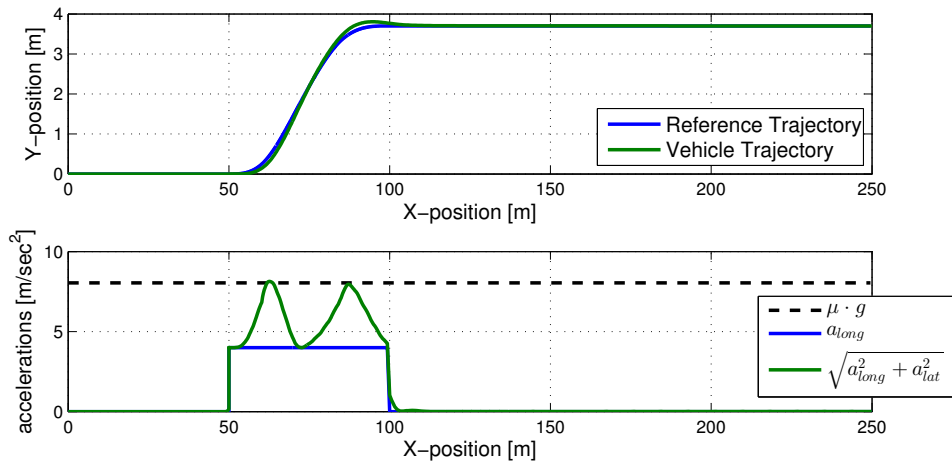


Figure 5.7: Trajectory following for $v_0 = 20$ m/sec, $a_{max} = 4$ m/sec², $\mu = 0.82$ and $\Delta Y = 3.7$ m.

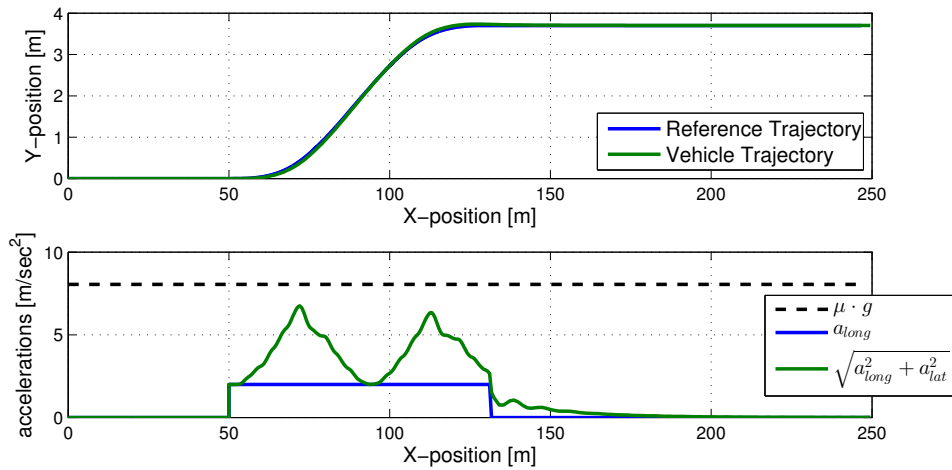


Figure 5.8: Trajectory following for $v_0 = 40$ m/sec, $a_{max} = 2$ m/sec², $\mu = 0.82$ and $\Delta Y = 3.7$ m.

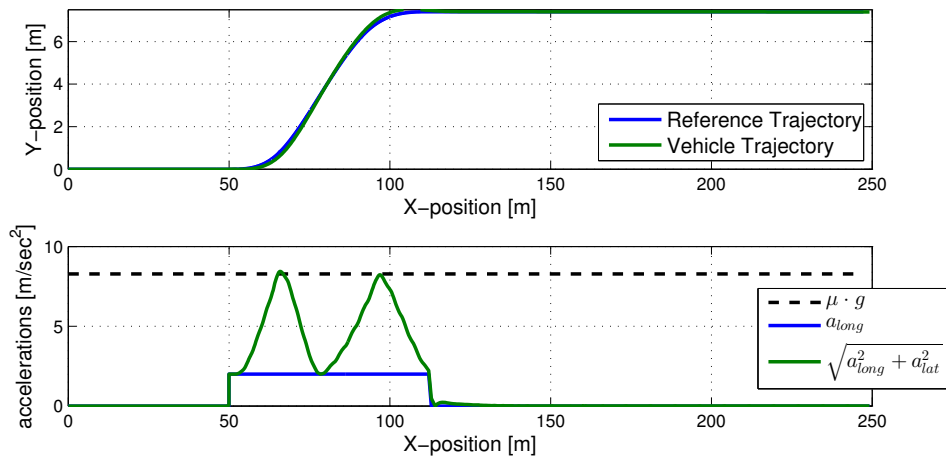


Figure 5.9: Trajectory following for $v_0 = 20$ m/sec, $a_{\max} = 2$ m/sec², $\mu = 0.82$ and $\Delta Y = 7.4$ m.

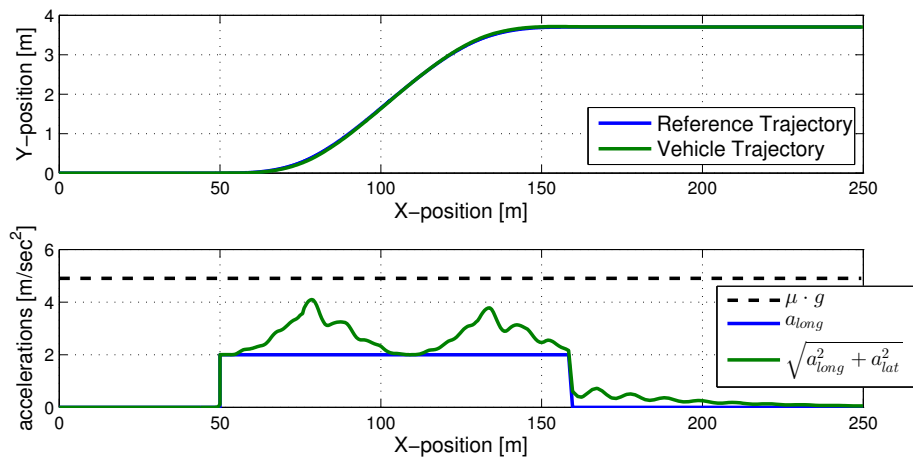


Figure 5.10: Trajectory following for $v_0 = 20$ m/sec, $a_{\max} = 2$ m/sec², $\mu = 0.5$ and $\Delta Y = 3.7$ m.

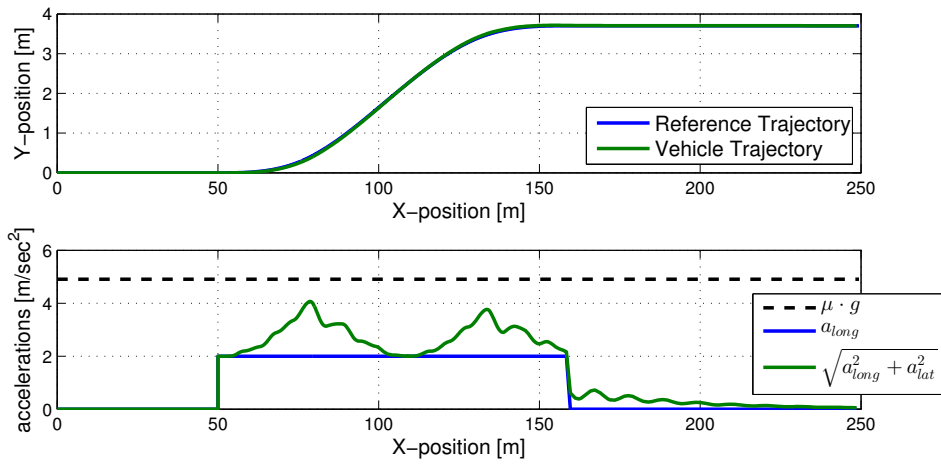


Figure 5.11: Trajectory following for $v_0 = 40$ m/sec, $a_{\max} = 2$ m/sec², $\mu = 0.5$ and $\Delta Y = 3.7$ m.

5.2 Trajectory Following using Lane Keeping Control

The previous sections show that clothoid-based trajectories and their arc-spline approximations are suitable for the representation and fast computation of lane change trajectories. This section is based on the fact that clothoid-based trajectories and their arc-spline approximations can in general be used to represent road segments [31, 37, 38]. That is, lane keeping can be effectively be applied in the control architecture in Section 4.1 when using arc-spline trajectories as a road representation. In addition, the relations between the trajectory curvature and the admissible vehicle velocity established in Section 5.1.1 can be used to evaluate which velocity profile is suitable for a given road segment. Next, Section 5.2.1 formalizes the representation of road segments. Then, Section 5.2.2 determines if a given velocity profile is suitable for driving along a road segment. Finally, Section 5.2.3 evaluates road following by several simulation examples.

5.2.1 Road Representation

We introduce a set $\mathcal{T} = \{T_1, T_2, \dots, T_N\}$ in order to represent the trajectory of a road. Each road segment $T_i \in \mathcal{T}$ is given by a clothoid curve $\mathcal{C}(P_s, \Psi_s, k_s, k_f, S)$, by an arc segment $\mathcal{A}(C, R, \Psi_s, S)$ or by a line segment $\mathcal{L}(P_s, \Psi_s, S)$. The relation between consecutive segments is given by

$$P_s(\mathcal{T}_{i+1}) = P_f(\mathcal{T}_i), \Psi_s(\mathcal{T}_{i+1}) = \Psi_f(\mathcal{T}_i), k_s(\mathcal{T}_{i+1}) = k_f(\mathcal{T}_i), \quad i = 1, \dots, N-1. \quad (5.15)$$

That is, a road trajectory \mathcal{T} has a continuous position, orientation angle and curvature. In the sequel, the curvature of a road trajectory \mathcal{T} is denoted as $k_{\mathcal{T}}(s)$. Furthermore, an arc-spline approximation $\hat{\mathcal{T}}$ of a road trajectory \mathcal{T} is obtained by replacing all clothoid curves in \mathcal{T} by the corresponding arc-spline according to Section 2.2.

An example for a road trajectory is shown in Fig. 5.12. It is given by the set $\mathcal{T} = \{T_1, T_2, \dots, T_{17}\}$, whose entries are specified in Table 5.1.

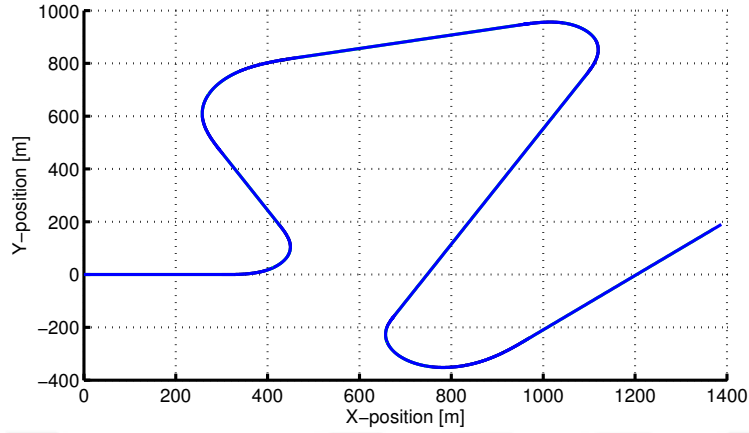


Figure 5.12: Example road trajectory \mathcal{T} .

5.2.2 Verification of Velocity Profiles

As was discussed in Section 5.1.1, there is a relation between the velocity/acceleration profile of a vehicle and the admissible curvature of vehicle trajectories as given in (5.5). This expression can be used to evaluate the drivability of a road trajectory \mathcal{T} when given a desired velocity profile. Let

$$\mathcal{V} : \mathbb{R} \mapsto \mathbb{R} : t \rightarrow \mathcal{V}(t) \quad (5.16)$$

be a velocity profile that maps each time instant t to a velocity value $\mathcal{V}(t)$. Then, the traveled arc-length is

$$\mathcal{S}(t) = \int_0^t \mathcal{V}(\tau) d\tau. \quad (5.17)$$

and the acceleration profile is

$$\mathcal{A}(t) = \frac{d\mathcal{V}(t)}{dt}. \quad (5.18)$$

Assuming that $\mathcal{V}(t)$ is a non-negative function such that vehicles always travel in the forward direction, it follows that $\mathcal{S}(t)$ in (5.17) is a monotonically increasing

Table 5.1: Parameters of the example road trajectory

T_1	T_2	T_3
$\mathcal{L}(0, 0, 300)$	$\mathcal{C}(P_f(T_1), \Psi_f(T_1), 0, 0.01, 100)$	$\mathcal{A}(P_f(T_2), \Psi_f(T_2), 100, 100)$
T_4	T_5	T_6
$\mathcal{C}(P_f(T_3), \Psi_f(T_3), 0.01, 0, 100)$	$\mathcal{L}(P_f(T_4), \Psi_f(T_4), 300)$	$\mathcal{C}(P_f(T_5), \Psi_f(T_5), 0, -0.005, 150)$
T_7	T_8	T_9
$\mathcal{A}(P_f(T_6), \Psi_f(T_6), -200, 200)$	$\mathcal{C}(P_f(T_7), \Psi_f(T_7), -0.005, 0, 150)$	$\mathcal{L}(P_f(T_8), \Psi_f(T_8), 500)$
T_{10}	T_{11}	T_{12}
$\mathcal{C}(P_f(T_9), \Psi_f(T_9), 0, -0.01, 100)$	$\mathcal{A}(P_f(T_{10}), \Psi_f(T_{10}), -100, 100)$	$\mathcal{C}(P_f(T_{11}), \Psi_f(T_{11}), -0.01, 0, 150)$
T_{13}	T_{14}	T_{15}
$\mathcal{L}(P_f(T_{12}), \Psi_f(T_{12}), 1000)$	$\mathcal{C}(P_f(T_{13}), \Psi_f(T_{13}), 0, 0.008, 50)$	$\mathcal{A}(P_f(T_{14}), \Psi_f(T_{14}), 125, 200)$
T_{16}	T_{17}	
$\mathcal{C}(P_f(T_{15}), \Psi_f(T_{15}), 0.008, 0, 250)$	$\mathcal{L}(P_f(T_{16}), \Psi_f(T_{16}), 600)$	

function. We write

$$\mathcal{S}^{-1} : \mathbb{R} \mapsto \mathbb{R} : s \rightarrow \mathcal{S}^{-1}(s) = t \text{ such that } \mathcal{S}(t) = s. \quad (5.19)$$

Both (5.16) and (5.18) can be parametrized using the arc-length in (5.17). The resulting velocity and acceleration profile in terms of the arc-length are hence written as

$$\mathcal{V}(s) = \mathcal{V}(\mathcal{S}^{-1}(s)), \quad (5.20)$$

$$\mathcal{A}(s) = \mathcal{A}(\mathcal{S}^{-1}(s)). \quad (5.21)$$

Using (5.5), it must hold that

$$\sqrt{a_{\text{long}}^2 + a_{\text{lat}}^2} = \sqrt{\mathcal{A}^2(s) + \mathcal{V}^4(s) k_{\mathcal{S}}^2} \leq \mu g, \quad (5.22)$$

which can be verified knowing the road curvature $k_{\mathcal{S}}(s)$, the velocity profile $\mathcal{V}(s)$ and the acceleration profile $\mathcal{A}(s)$.

5.2.3 Evaluation

We illustrate the condition in the previous section by using different velocity profiles for the example road in Fig. 5.12. We note that $k_{\max} = 0.01 \cdot 1/\text{m}$ is the largest curvature along the example road. That is, the velocity when passing the location with the largest curvature is given by

$$\hat{v}_{0.82} = \sqrt{\mu g / k_{\max}} = 28.36 \text{ m/sec},$$

when using $\mu = 0.82$ (dry road) and

$$\hat{v}_{0.5} = \sqrt{\mu g / k_{\max}} = 22.15 \text{ m/sec},$$

when using $\mu = 0.5$ (wet road). Accordingly, we first consider the simple case of a constant velocity $v_{0.82}$ and $v_{0.5}$ when passing the example road. The resulting simulations are shown in Fig. 5.13 to 5.18.

The upper part of Fig. 5.13 shows the road curvature, whereas the lower part compares the maximum admissible velocity

$$v_{\max}(s) = \sqrt{\mu g / k_{\mathcal{S}}(s)}$$

and the actual velocity $\mathcal{V}(s)$. Note that v_{\max} is only displayed for cases where $k_{\mathcal{S}}(s) \neq 0$. It can be seen that the actual vehicle velocity always stays below $v_{\max}(s)$, whereby a higher velocity could be admissible in curves with a smaller curvature.

This observation is also confirmed in Fig. 5.14 that compares the admissible acceleration according to the friction circle with the actual acceleration. A small violation of the bound μg is observed for a very short time duration in sharp turns.

Nevertheless, Fig. 5.15 confirms that the chosen velocity profile is suitable for trajectory following. The tracking error for the overall example road trajectory stays below 8 cm.

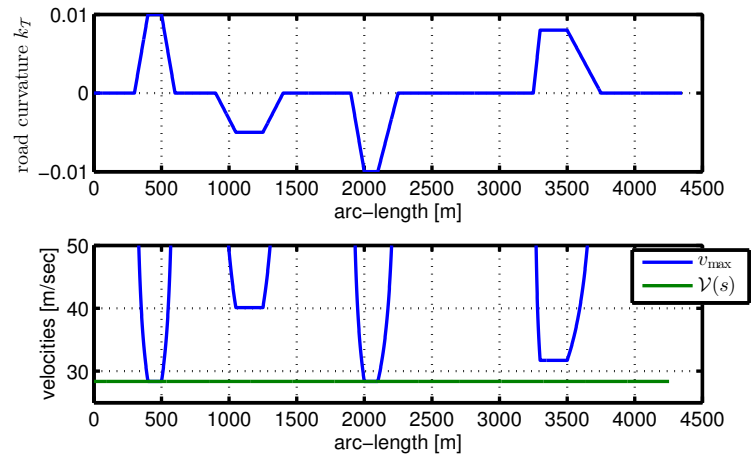


Figure 5.13: Road curvature (upper) and velocity comparison (lower) for $v_{0.82}$.

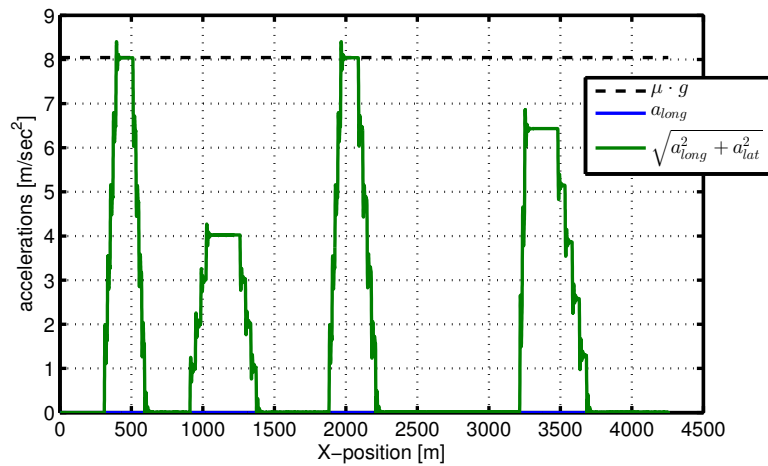


Figure 5.14: Acceleration comparison for $v_{0.82}$.

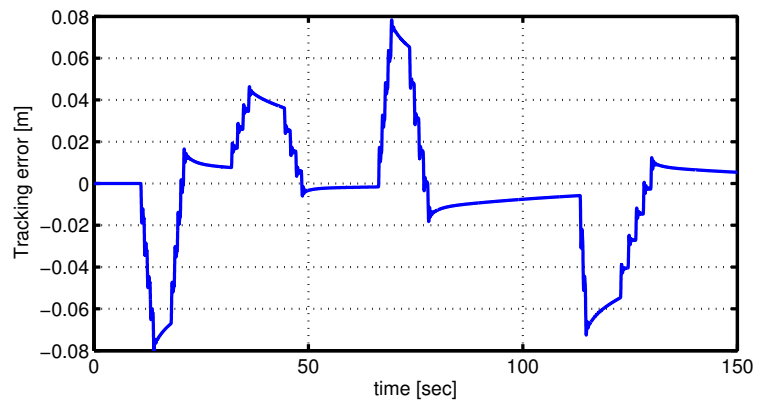


Figure 5.15: Tracking error for $v_{0.82}$.

The same observations are made in Fig. 5.16 to 5.18 for the case of $\mu = 0.5$ with the reduced velocity $v_{0.5} = 22.15$ m/sec. Here, the tracking error in Fig. 5.18 is slightly smaller compared to Fig. 5.15 and more time is needed to complete the road.

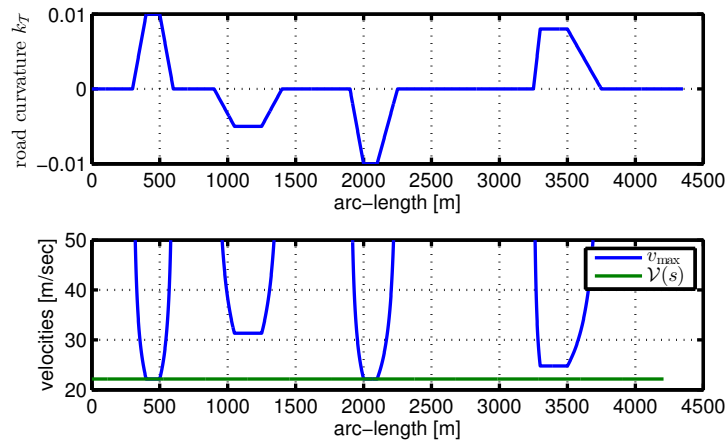


Figure 5.16: Road curvature (upper) and velocity comparison (lower) for $v_{0.5}$.

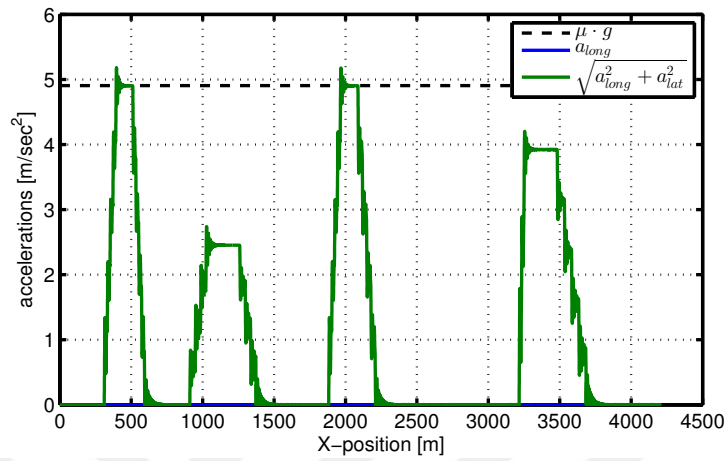


Figure 5.17: Acceleration comparison for $v_{0.5}$.

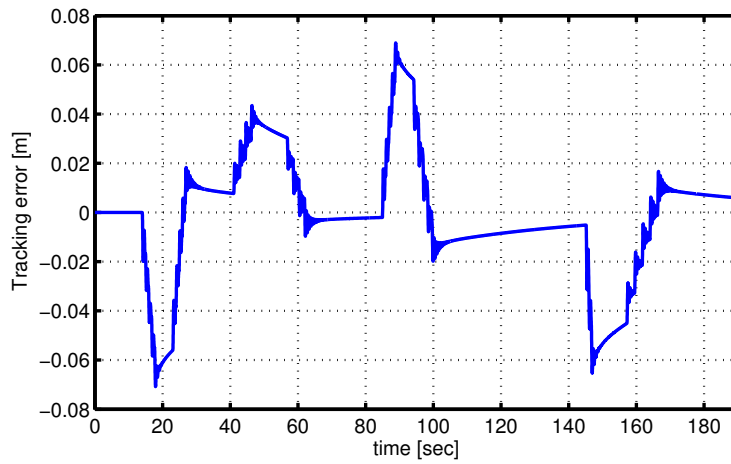


Figure 5.18: Tracking error for $v_{0.5}$.

The previous experiments were conducted with a constant velocity along the whole road. The next experiment uses $\mu = 0.82$ and a velocity profile that approaches the respective maximum velocity of each curve as shown in the lower part of Fig. 5.19.

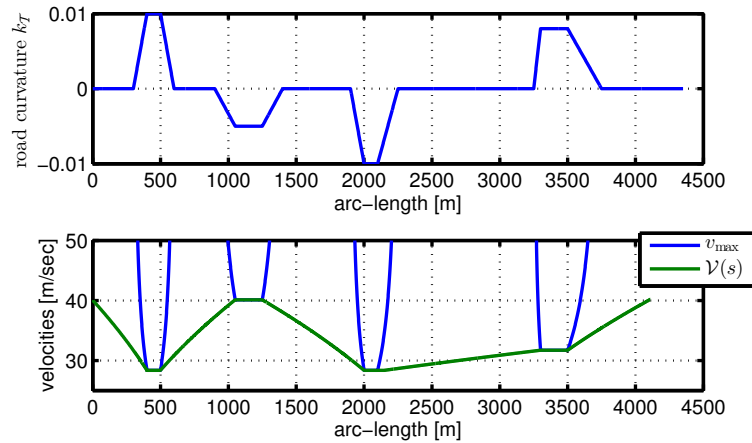


Figure 5.19: Road curvature (upper) and velocity comparison (lower) for $v_{0.5}$.

It is again the case that there is a slight violation of the acceleration constraint in Fig. 5.20 that does not show any negative effect on the tracking error in Fig. 5.21. Moreover, the travel time along the road trajectory is considerably shortened than the comparable case in Fig. 5.15. That is, even when using such fast velocity profile, the road approximation and prediction by arc-splines according to Section 5.2.1 and 4.3.4 is suitable for trajectory following with a small tracking error if the acceleration constraint in (5.22) is fulfilled.

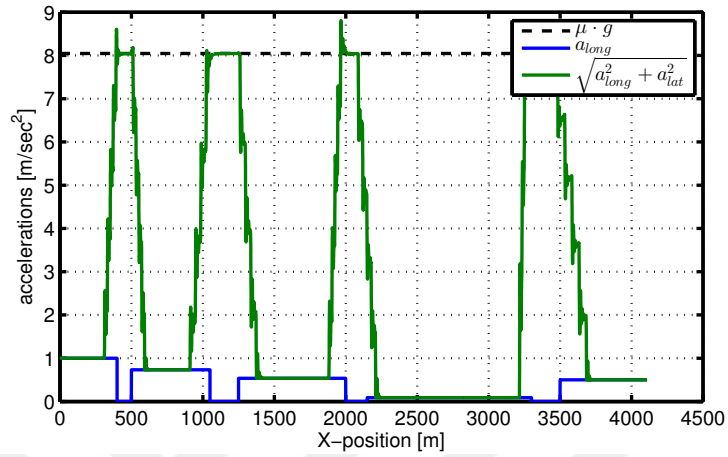


Figure 5.20: Acceleration comparison for $v_{0.5}$.

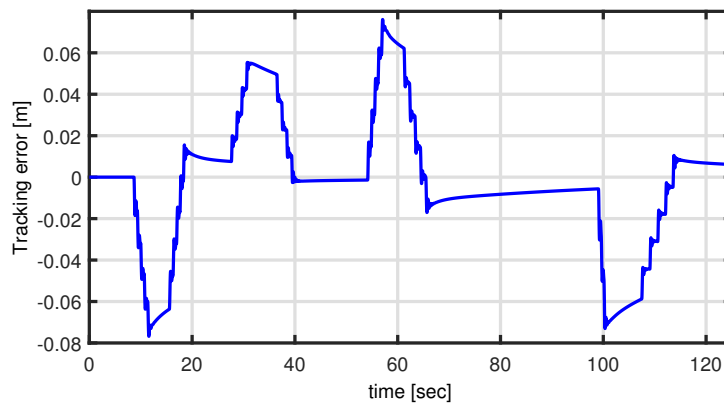


Figure 5.21: Tracking error for $v_{0.5}$.

5.3 Cooperative Adaptive Cruise Control on Curved Roads

An important ITS application for increasing the traffic throughput is tight vehicle following that can be realized using the recent technology of cooperative adaptive cruise control (CACC) [18, 19, 20, 21, 22, 23]. CACC is based on distance measurements and communicated state information among vehicles.

When designing CACC, it has to be ensured that oscillations are avoided and signal levels are not amplified along a vehicle string in order to maintain driving safety and comfort. In the literature, this requirement is addressed by the condition of string stability [68, 69, 21] and there are various controller design methods in order to achieve string stability.

The string stability research in the existing literature is conducted for the case of straight roads, where it is sufficient to model the longitudinal motion using linear models. However, on curved roads, the lateral dynamics affect the longitudinal motion of vehicles such that string stability as discussed in Section 5.3.1 can no longer be ensured. Accordingly, the main focus of this section is to preserve string stability when turning.

5.3.1 CACC

In this thesis, we consider the case where multiple vehicles follow each other in the form of a *vehicle string* at a small inter-vehicle spacing. The basic scenario is depicted in Fig. 5.22.

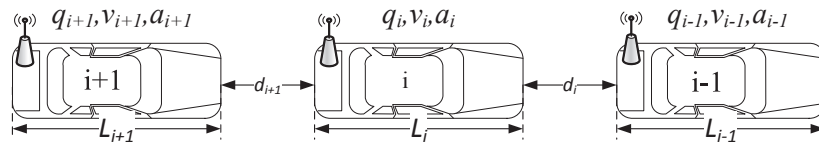


Figure 5.22: Vehicle following scenario.

Each vehicle i is characterized by its rear-bumper position q_i , its velocity v_i , its acceleration a_i and its length L_i . Moreover, the distance between vehicle i and

$i - 1$ is written as d_i and evaluates to

$$d_i(t) = q_{i-1}(t) - q_i(t) - L_i. \quad (5.23)$$

The literature suggests different methods for safe vehicle following [70]. This thesis employs the recent technology of cooperative adaptive cruise control (CACC) [68, 20, 23] that is an extension to the established technology of adaptive cruise control (ACC). CACC employs both distance measurements using Radar or LIDAR and state information that is exchanged between vehicles using vehicle to vehicle (V2V) communication.

The most common realization of CACC in the recent literature is based on the idea of *predecessor following* (PF). Using PF, only vehicle $i - 1$ provides state information to vehicle i via V2V communication [20, 22, 23]. The corresponding control architecture is displayed in Fig. 5.23.

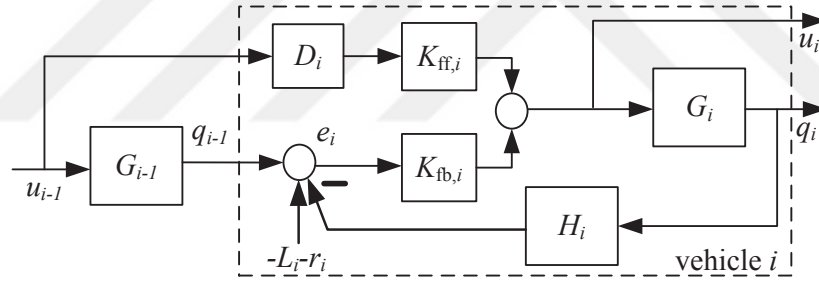


Figure 5.23: CACC realization for a generic vehicle i .

Here, G_i represents the transfer function of the vehicle plant. $K_{fb,i}$ is a feedback controller using the spacing error e_i and $K_{ff,i}$ is a feedforward controller that receives the input signal u_{i-1} from the predecessor vehicle $i - 1$ with a potential delay $D_i = e^{-\Psi_i s}$. The transfer function H_i represents the *spacing policy* employed for tight vehicle following. The most commonly used spacing policy in the recent literature is the *constant headway time* policy [22, 21, 23]. It defines the desired vehicle spacing as

$$d_{i,r} = r_i + h_i v_i. \quad (5.24)$$

Here, r_i is the distance at standstill (for $v_i = 0$) and h_i denotes the desired headway time. Accordingly, $H_i(s) = 1 + h_i s$ and the spacing error $e_i(t)$ is computed as

$$e_i(t) = d_i(t) - d_{i,r}(t). \quad (5.25)$$

Signals such as velocity, acceleration and spacing error of each vehicle depend on the maneuvers of its predecessor vehicles. In order to keep the signal levels of follower vehicles bounded, it is required that fluctuations that of predecessor vehicles (due to maneuvers of the leader vehicle or disturbances within the string) are attenuated along the string. Specifically, small signal variations of predecessor vehicles should not cause increased signal levels in the follower vehicles in order to maintain driving safety, comfort and scalability of the string length. Furthermore, oscillations in a vehicle string are undesired.

This requirement is addressed by the property of *string stability* [68, 69, 20]. In this thesis, we employ a sufficient condition for strict L_∞ string stability as defined by [21].

Consider Fig. 5.23. Let y_i be a relevant output signal (such as acceleration) and write u_1 for the input signal of the leader vehicle. We further define the transfer functions $P_1(s) = Y_1(s)/U_1(s)$ and $\Gamma_i(s) = Y_i(s)/Y_{i-1}(s)$ with the respective impulse responses $p_1(t)$ and $\gamma_i(t)$. Then, a vehicle string is strictly L_∞ string stable if [69, 21]

$$\|p_1(t)\|_{L_1} \leq \infty, \|\Gamma_i(s)\|_{H_\infty} \leq 1 \text{ and } \gamma_i(t) \geq 0. \quad (5.26)$$

Hereby, $\|\bullet\|_{L_1}$ and $\|\bullet\|_{H_\infty}$ represent the L_1 and H_∞ norm, respectively. (5.26) ensures that the level of the output signal y_i decreases along the string.

The literature employs different vehicle models for the study of string stability. In this thesis, we use a model with acceleration input $u_i = a_i$ for each vehicle i as in [71, 72] with the transfer function

$$G_i(s) = \frac{Q_i(s)}{U_i(s)} = \frac{1}{s^2}. \quad (5.27)$$

Then, it is possible to apply controller transfer functions in the form

$$K_{fb,i}(s) = \omega_i(s + \omega_i) \text{ and } K_{ff,i}(s) = \frac{1}{1 + s h_i} \quad (5.28)$$

as suggested by [19] to achieve string stability.

5.3.2 Decoupling and Practical Implications

Our study is based on the nonlinear model in Section 2.1.3. On a straight road, it holds that $\dot{\psi} = \dot{y} = \delta = 0$. That is, the vehicle model in (2.7) to (2.9) reduces to the linear plant model in (5.27) when using a traction force of $F_{lf} = m \cdot u$. Nevertheless, this is no longer true on a curved road such that string stability according to Section 5.3.1 cannot be guaranteed on curved roads. However, using the decoupling proposed in Section 3.2, it already holds that the longitudinal motion is decoupled from the lateral motion such that the linear plant model in (5.27) is also valid on curved roads. Hence, L_∞ string stability according to Section 5.3.1 holds for the longitudinal motion along curved roads when applying (3.3). We note that (3.3) reduces to $F_{lf} = m a_r$ on straight roads, where $\delta = \beta = 0$.

We next discuss several requirements when realizing the traction force according to (3.3). First, we note that measurements or estimates of the signals δ , β and F_{cf} are available in advanced vehicle applications. The steering angle δ can be directly measured. Furthermore, the sideslip angle $\beta = \tan^{-1}(\dot{y}/\dot{x})$ can either be estimated directly using recent methods such as [53, 54] or computed using estimations or measurements of the velocities \dot{x} and \dot{y} from inertial measurement units and differential GPS [55, 56]. Similar, existing estimation methods such as [57, 58] can be used for estimating the lateral tire forces F_{cf} and F_{cr} .

Second, we consider that the computed traction force F_{lf} in (3.3) has to be realized by applying torque to the actuated wheels of the vehicle. This task is achieved by recent methods for traction force tracking [56].

Finally, we note that the proposed CACC extension controls the longitudinal vehicle motion, compensating the effect of the lateral vehicle dynamics. The steering angle for the lateral motion can be supplied manually by a human driver

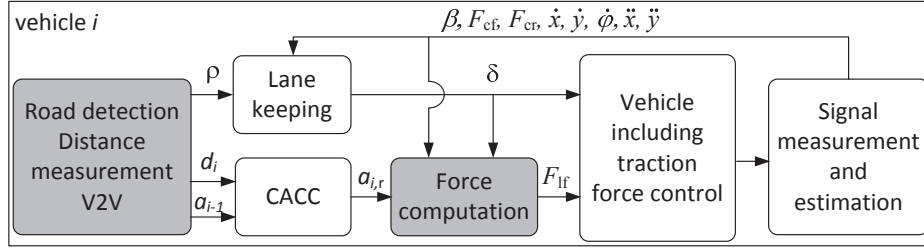


Figure 5.24: Control architecture for a generic vehicle i .

or automated by a lane-keeping system.

5.3.3 Vehicle Architecture

We employ the vehicle architecture in Fig. 5.24 for a simulation study of the proposed CACC for curved roads. The nonlinear vehicle model with decoupling traction force in Section 3.2 is extended by a traction force control module according to [56] for obtaining realistic results. The vehicle signals β , \dot{x} , \dot{y} , $\dot{\psi}$, \ddot{x} , \ddot{y} are measured and the lateral forces F_{cf} , F_{cr} are estimated using the method by [57]. In order to follow a given road, the steering angle is adjusted using a lane keeping method from the existing literature [63]. Finally, vehicle following is realized by CACC as described in Section 5.3.1 extended with the proposed traction force computation in (3.3). The required road curvature ρ for lane keeping and the distance d_i and predecessor acceleration a_{i-1} are obtained from measurements and V2V communication. We note that the vehicle architecture is created in order to evaluate the proposed decoupling method under realistic conditions. The selected methods for traction force control, lane keeping, signal estimation and the CACC controller design can be substituted by other methods. The relevant parameter values of the vehicle model and the CACC controller are summarized in Table 5.2. We use the same parameter values for each vehicle.

In the following sections, we compare the proposed method (denoted as "with decoupling") with the common CACC implementation for straight roads ("without decoupling") that uses $F_{lf} = m \cdot a_r$ instead of the decoupling force in (3.3).

Table 5.2: Vehicle and CACC controller parameters.

m	I_{zz}	B	C	D	E
1480	1950	8.22	1.65	$-1.7 \cdot 10^4$	-10
a	b	h_i	ω_i	Ψ_i	
1.421	1.029	0.8	0.6	0.1	

5.3.4 Evaluation

Vehicle Following in Curves

The first experiment evaluates the case of keeping a constant velocity while traveling on a curved road. To this end, a road profile based on clothoid arcs is created, respecting that clothoid arcs are to be used according to road standards [63]. That is, the road profile consists of segments, whose curvature changes linearly with the arc-length of the road as is shown in Fig. 5.25. The created road profile is chosen to contain segments with increasing/decreasing as well as constant curvature. Noting that the curve radius is given by $1/\rho$, a minimum radius of 80 m is obtained.

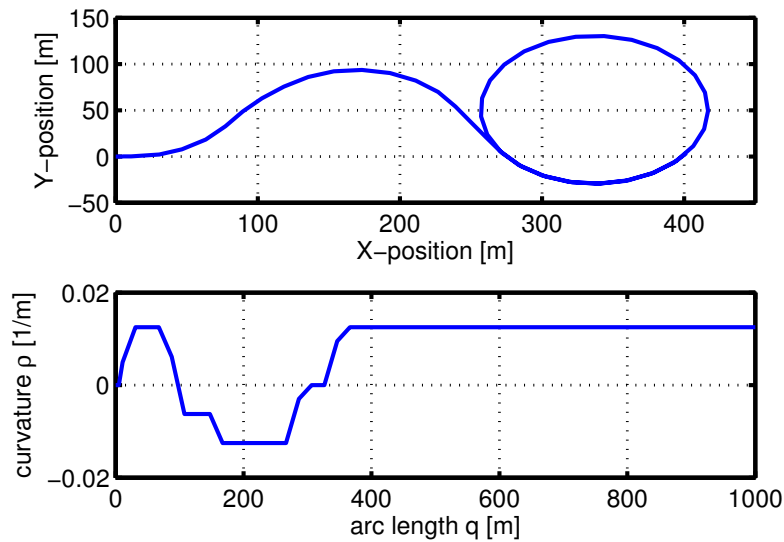


Figure 5.25: Created road profile (upper); road curvature ρ (lower).

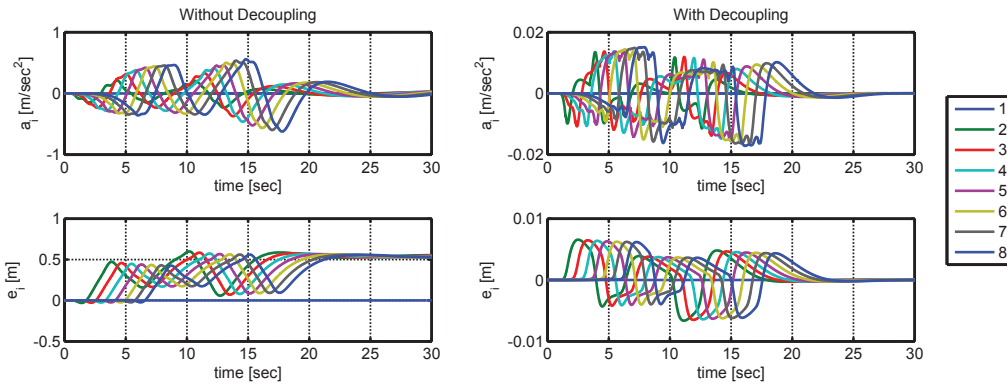


Figure 5.26: Simulation results for a curved road with zero acceleration.

Using this road profile, we next simulate a vehicle string with 8 vehicles that implement the architecture in Fig. 5.24 with the parameters in Table 2.1. In this experiment, each vehicle has an initial velocity of 30 m/sec and the initial distance error is $e_i(0) = 0$ for each vehicle $i = 2, \dots, 8$. The leader vehicle 1 travels along the road with zero acceleration.

Fig. 5.26 shows a comparison of the case without decoupling (left) and with decoupling (right). It can be seen that the acceleration deviates from the reference acceleration up to around 0.5 m/sec^2 in the case without decoupling, whereas the acceleration deviations are negligible when using decoupling. In addition, much larger distance error signals are observed in the case without decoupling.

Vehicle Following with Acceleration Changes

In the next experiment, we consider the same road profile in Fig. 5.25. Nevertheless, we simultaneously adjust the acceleration of the leader vehicle with successive speed-up and slow-down maneuvers as can be seen in Fig. 5.27. The initial velocities and distance errors are chosen as in Section 5.3.4. In comparison, it is observed that the acceleration signals show oscillations and overshoot in the case without decoupling, which indicates a violation of the string stability condition in (5.26). It can further be seen that larger error signal levels are encountered if decoupling is not used.

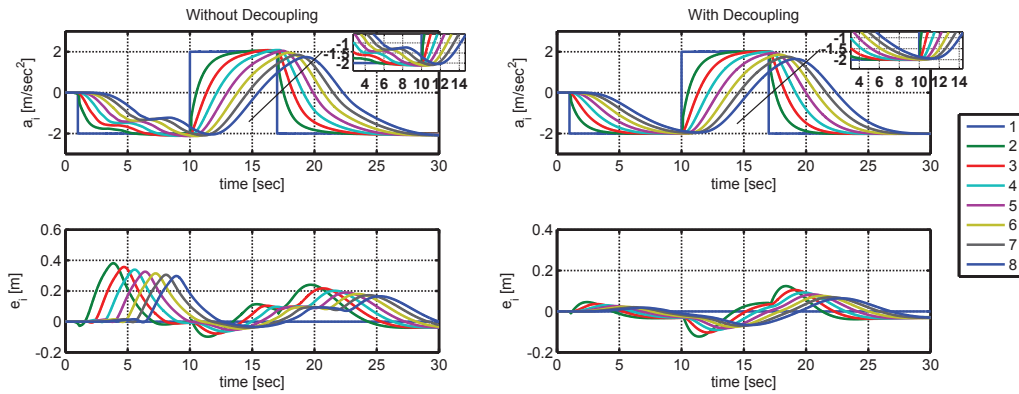


Figure 5.27: Simulation results for a curved road with a given acceleration profile.

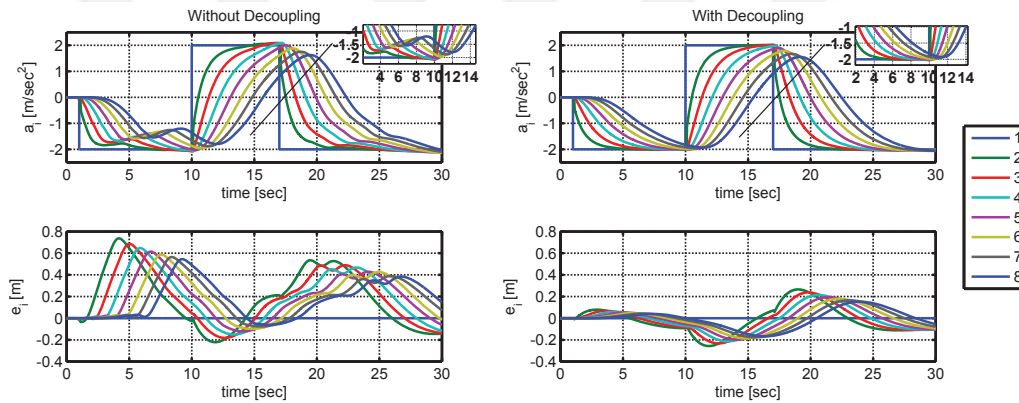


Figure 5.28: Simulation results for a curved road with two lane changes.

Lane Change of a Vehicle String

In the last experiment, we perform two lane changes of the vehicle string on the curved road in Fig. 5.25. The lane change trajectories are realized in the form of concatenated clothoids as proposed by [60] and are initiated by the leader vehicle at the times 6.8 and 18.0.

It can be seen in Fig. 5.28 that the decoupling strategy is again effective. The acceleration signals of each vehicle follow the respective signal of the predecessor vehicle without overshoot in the case with decoupling. Conversely, overshoot and oscillations are observed in the case without decoupling, indicating a violation

of string stability. Here, the oscillations starting around time 2 are due to the curvature change of the road which is superposed on the lane change starting from time 6.8. The oscillations starting around time 20 are caused by the lane change at time 18. No such effect is seen in the case with decoupling. In addition, our decoupling method again leads to smaller spacing errors.



CHAPTER 6

Conclusions and Future Work

The development of self-driving vehicles is an emerging subject both in industry and in the recent academic literature. Performing autonomous lane changes is one of the important tasks when realizing self-driving vehicles. Hereby, it is required to determine vehicle trajectories for lane changes that comply with the vehicle dynamics as well as the driving situation and can hence be safely followed by vehicles. In practice, it is necessary to choose a trajectory representation that can be used for further calculations and to compute such trajectories in real-time. The subject of this thesis is the computation of lane change trajectories for self-driving vehicles, the approximation of such trajectories by clothoid-type curves and the evaluation of the trajectory parameters in real-time.

The first main subject of this thesis is the computation of trajectories for lane changes of self-driving vehicles using optimal control. Two optimal control methods are developed for nonlinear vehicle models that capture the longitudinal and lateral motion during lane changes. As the first thesis contribution, these models are extended by a feedback of the traction force in order to decouple the longitudinal motion from the lateral motion. Hence, these models are different from existing models in the literature. Based on the models, a collocation method and a gradient-based method for solving the optimal control problem are developed as the second thesis contribution. The collocation method uses third-order polynomials for the trajectory approximation and can be solved using nonlinear programming. The gradient-based method is based on a finite difference approximation of the nonlinear vehicle model and a direction finding algorithm. It offers an easier computation since it only requires the solution of quadratic programming prob-

lems. The experimental evaluation of these methods shows that the collocation method does not find correct optimal control solutions for large vehicle velocities. In contrast, the gradient-based method is able to compute suitable optimal control trajectories.

It is observed during the thesis study that the optimal control solutions cannot be determined in real-time due to the different optimization steps. That is, they are not suitable for a direct implementation in practical applications. In order to address this problem, the second main subject of the thesis is the approximation of the optimal control trajectories by curves that can be parametrized analytically and that can be computed in real-time. To this end, the thesis suggests to use bi-elementary paths that are based on clothoid curves and their analytical approximation by bi-elementary arc-splines. As the third thesis contribution, it is shown that bi-elementary arc-splines provide a tight approximation of the optimal control trajectories for lane changes. The thesis further proposes a control architecture such that vehicles can follow the computed lane change trajectories at a desired velocity.

Respecting the fact that bi-elementary paths can be used for representing lane change trajectories for self-driving vehicles, the remaining question is how to determine the trajectory parameters without using the optimal control solutions. The fourth thesis contribution is the fast computation of vehicle trajectories for lane changes depending on the driving situation. To this end, the thesis first develops an efficient method for computing the parameters of bi-elementary paths based on a Newton iteration. Then, the thesis determines an analytical bound on the path curvature depending on the maximum velocity profile of a vehicle during a lane change. Using this bound, the thesis proposes a computational procedure for selecting the parameters of bi-elementary paths that are suitable for lane change trajectories. This parameter selection can be efficiently carried out in real-time based on the current vehicle velocity and a bound on the admissible acceleration. Simulation experiments with the nonlinear vehicle model show that the proposed method determines suitable lane change trajectories.

Finally, the thesis considers two applications of the developed methods. First,

it is shown that the clothoid-based curves can be used to represent roads. Hence, the proposed control architecture with clothoid-based reference trajectories enables road following. Second, the application of the developed methods to the technology of cooperative adaptive cruise control (CACC) is discussed. CACC is used to ensure tight vehicle following in vehicle strings. In the existing literature, CACC is always used on straight roads. Nevertheless, the desirable properties of CACC such as string stability are no longer valid on curved roads. Using the proposed control architecture that decouples the longitudinal from the lateral vehicle motion, our method ensures string stability on curved roads.

There are several directions for future work in order to extend the contributions of the thesis. First, it is possible to refine the developed collocation method by changing the parametrization from polynomials to arc-splines. The thesis focuses on the case of straight roads. In future work, it is intended to extend the obtained results to the case of curved roads. In addition, the joint computation of an optimal velocity profile and the desired lane change trajectory parameters will be investigated. Finally, it is envisaged to apply the developed methods to more detailed vehicle models such as four-wheel models instead of a single track model.

Bibliography

- [1] **P. Varaiya (1993)**, “Smart cars on smart roads: problems of control,” *Automatic Control, IEEE Transactions on*, vol. 38, pp. 195–207.
- [2] **J. S. Sussman (2005)**, *Perspectives on Intelligent Transportation Systems (ITS)*. Springer US, 1 ed.
- [3] **T. S. L. Sumit Ghosh(2010)**, *Intelligent Transportation Systems: Smart and Green Infrastructure Design*. CRC Press.
- [4] **G. Rafiq, B. Talha, M. Patzold, J. Gato Luis, G. Ripa, I. Carreras, C. Coviello, S. Marzorati, G. Perez Rodriguez, G. Herrero, and M. Desaegeer,(2013)** “What’s new in intelligent transportation systems?: An overview of european projects and initiatives,” *Vehicular Technology Magazine, IEEE*, vol. 8, pp. 45–69, Dec.
- [5] **Z. Cong, B. D. Schutter, and R. Babuška,(2013)** “Ant colony routing algorithm for freeway networks,” *Transportation Research Part C*, vol. 37, pp. 1–19.
- [6] **Z. He, W. Guan, and S. Mab,(2013)** “A traffic-condition-based route guidance strategy for a single destination road network,” *Transportation Research Part C*, vol. 32, pp. 89–102.
- [7] **J. Dallmeyer, R. Schumann, A. D. Lattner, and I. J. Timm,(2015)** “Don’t go with the ant flow: Ant-inspired traffic routing in urban environments,” *Journal of Intelligent Transportation Systems*, vol. 19, no. 1, pp. 78–88.
- [8] **W. J. Schakel, V. L. Knoop, and B. van Arem,(2012)** “Integrated lane change model with relaxation and synchronization,” *Transportation Research Record: Journal of the Transportation Research Board*, vol. 2316, pp. 47–57.
- [9] **M. Rahman, M. Chowdhury, Y. Xie, and Y. He,(2013)** “Review of microscopic lane-changing models and future research opportunities,” *Intelligent Transportation Systems, IEEE Transactions on*, vol. 14, pp. 1942–1956, Dec.

- [10] **S. Moridpour, M. Sarvi, , and G. Rose,(2010)** “Lane changing models: A critical review,” *transportation Letters International Journal on Transportation Research*, vol. 2, pp. 157–173, July .
- [11] **A. Rucco, G. Notarstefano, and J. Hauser,(2014)** “Optimal control based dynamics exploration of a rigid car with longitudinal load transfer,” *Control Systems Technology, IEEE Transactions on*, vol. 22, pp. 1070–1077, May 2014.
- [12] **R. Pepy, A. Lambert, and H. Mounier,(2006)** “Path planning using a dynamic vehicle model,” in *Information and Communication Technologies, 2006. ICTTA '06. 2nd*, vol. 1, pp. 781–786.
- [13] **P. Falcone, M. Tufo, F. Borrelli, J. Asgari, and H. Tsengz,(2007)** “A linear time varying model predictive control approach to the integrated vehicle dynamics control problem in autonomous systems,” in *Decision and Control, 2007 46th IEEE Conference on*, pp. 2980–2985, Dec 2007.
- [14] **M. Werling, S. Kammel, J. Ziegler, and L. Grll,(2012)** “Optimal trajectories for time-critical street scenarios using discretized terminal manifolds,” *The International Journal of Robotics Research*, vol. 31, no. 3, pp. 346–359, 2012.
- [15] **Autonomous cars (2013)**, “ self-driving the new auto industry paradigm,” tech. rep., Morgan Stanley Blue Paper, November 2013.
- [16] **IEEE news release(2012)**, “http://www.ieee.org/about/news/2012/5september_2_2012.html“, 2. September 2012.
- [17] **D. P. Bertsekas,(2000)**, *Dynamic Programming and Optimal Control*. Athena Scientific, 2nd ed.
- [18] **R. Rjamani and S. E. Shladover,(2001)**, “An experimental comparative study of autonomous and cooperative control systems for automated vehicles,” *Journal of Transportation Research, Part C: Emerging Technologies*, vol. 9, pp. 15–31, February 2001.
- [19] **G. J. L. Naus, R. P. A. Vugts, J. Ploeg, M. J. G. Van de Molengraft, and M. Steinbuch,(2010)** ,“String-stable cacc design and experimental validation: A frequency-domain approach,” *Vehicular Technology, IEEE Transactions on*, vol. 59, pp. 4268–4279, Nov 2010.
- [20] **J. Ploeg, D. Shukla, N. Van De Wouw, and H. Nijmeijer,(2014)** “Controller synthesis for string stability of vehicle platoons,” *Intelligent Transportation Systems, IEEE Transactions on*, vol. 15, pp. 854–865, April 2014.

- [21] **J. Ploeg, N. van de Wouw, and H. Nijmeijer,(2014)**, “ L_p string stability of cascaded systems: Application to vehicle platooning,” *Control Systems Technology, IEEE Transactions on*, vol. 22, pp. 786–793, March 2014.
- [22] **S. E. Shladover, C. Nowakowski, X.-Y. Lu, and R. Ferlis,(2015)**, “Cooperative adaptive cruise control: Definitions and operating concepts,” *Transportation Research Record*, vol. 2489, pp. 145–152, 2015.
- [23] **K. C. Dey, L. Yan, X. Wang, Y. Wang, H. Shen, M. Chowdhury, L. Yu, C. Qiu, and V. Soundararaj, (2016)**, “A review of communication, driver characteristics, and controls aspects of cooperative adaptive cruise control (CACC),” *IEEE Transactions on Intelligent Transportation Systems*, vol. 17, pp. 491–509, Feb 2016.
- [24] **D. R. Rajamani, “Vehicle dynamics and control(2011),”** in *Springer New York Dordrecht Heidelberg London (SNYDHL), 2011*, pp. 1–493, June 2011.
- [25] **H. B. Pacejka(2002)**, *Tire and Vehicle Dynamics*. Oxford: Butterworth-Heinemann, 2002.
- [26] **R. Attia, R. Orjuela, and M. Basset,(2012)** “Coupled longitudinal and lateral control strategy improving lateral stability for autonomous vehicle,” in *American Control Conference (ACC), 2012*, pp. 6509–6514, June 2012.
- [27] **M. P. Gianpiero Mastinu, ed.(2014)**, *Road and Off-Road Vehicle System Dynamics Handbook*. CRC Press, 2014.
- [28] **M. E. Khatir and E. J. Davison,(2006)**, “A decentralized lateral-longitudinal controller for a platoon of vehicles operating on a plane,” in *2006 American Control Conference*, pp. 6 pp.–, June 2006.
- [29] **H. B. Pacejka and I. J. M. Besselink,(1997)**, “Magic formula tyre model with transient properties,” *Vehicle System Dynamics*, vol. 27, no. sup001, pp. 234–249, 1997.
- [30] **A. Rucco, G. Notarstefano, and J. Hauser,(2014)**, “Optimal control based dynamics exploration of a rigid car with longitudinal load transfer,” *Control Systems Technology, IEEE Transactions on*, vol. 22, pp. 1070–1077, May 2014.
- [31] **K. G. Baass,(1984)**, “The use of clothoid templates in highway design,” *Transportation Forum*, vol. 1, pp. 47–52, 1984.
- [32] **F. E. P. E. Jahnke,(1945)**, *Tables of Functions with Formulae and Curves*. Dover Publications, New York, 4th ed., 1945.

- [33] **P. J. Davis**,(1993), *Spirals: from Theodorus to Chaos*. A. K. Peters, Wellesley, Maine, 1993.
- [34] **D. S. Meek and D. J. Walton**,(2004), “An arc spline approximation to a clothoid,” *J. Comput. Appl. Math.*, vol. 170, pp. 59–77, Sept. 2004.
- [35] **D. Meek and D. Walton**,(2004), “A note on finding clothoids,” *Journal of Computational and Applied Mathematics*, vol. 170, no. 2, pp. 433–453, 2004.
- [36] **Z. Li and D. Meek**,(2005), “Smoothing an arc spline,” *Computers & Graphics*, vol. 29, no. 4, pp. 576–587, 2005.
- [37] **A. Schindler, G. Maier, and S. Pangerl**,(2011), “Exploiting arc splines for digital maps,” in *2011 14th International IEEE Conference on Intelligent Transportation Systems (ITSC)*, pp. 1–6, Oct 2011.
- [38] **S. Brummer, F. Janda, G. Maier, and A. Schindler**,(2013), “Evaluation of a mapping strategy based on smooth arc splines for different road types,” in *16th International IEEE Conference on Intelligent Transportation Systems (ITSC 2013)*, pp. 160–165, Oct 2013.
- [39] **J. A. Laval and C. F. Daganzo**,(2006), “Lane-changing in traffic streams,” *Transportation Research Part B: Methodological*, vol. 40, no. 3, pp. 251–264, 2006.
- [40] **M. Cassidy and R. Bertini**,(1999) ,“Some traffic features at freeway bottlenecks,” *Transportation Research Part B*, vol. 33, pp. 25–42, February 1999.
- [41] **H. Jula, E. B. Kosmatopoulos, and P. A. Ioannou**,(2000), “Collision avoidance analysis for lane changing and merging,” *IEEE transactions on Vehicular Technology*, vol. 49, pp. 2295–2308, November 2000.
- [42] **C. Schlenoff, R. Madhavan, and Z. Kootbally**,(2006), “Pride: A hierarchical, integrated prediction framework for autonomous on-road driving,” in *Proceedings of the 2006 IEEE International Conference on Robotics and Automation*, (Orlando, Florida), 2006.
- [43] **N. A. Webster, T. Suzuki, E. Chung, and M. Kuwahara**, (2007), “Tactical driver lane change model using forward search,” in *Proceeding of the 86th Transportation Research Board Annual Meeting*, (Washington, DC), 2007.
- [44] **P. G. Gipps**,(1986), “A model for the structure of lane-changing decisions,” *Transportation Research B*, vol. 20, no. 5, pp. 403–414, 1986.

- [45] **R. Wiedemann and U. Reiter,(1992)**, “Microscopic traffic simulation: the simulation system mission, background and actual state,” in *CEC Project ICARUS (VI052), Final Report*, vol. 2, Appendix A, 1992.
- [46] **P. Hidas,(2002)**, “Modelling lane changing and merging in microscopic traffic simulation,” *Transportation Research Part C*, vol. 10, no. 5-6, pp. 351–371, 2002.
- [47] **P. Hidas,(2005)**, “Modelling vehicle interactions in microscopic simulation of merging and weaving,” *Transportation Research Part C*, vol. 13, no. 1, pp. 37–62, 2005.
- [48] **W. Xiaorui and Y. Hongxu,(2013)**, “A lane change model with the consideration of car following behavior,” *Procedia - Social and Behavioral Sciences*, vol. 96, no. 0, pp. 2354–2361, 2013. Intelligent and Integrated Sustainable Multimodal Transportation Systems Proceedings from the 13th {COTA} International Conference of Transportation Professionals (CICTP2013).
- [49] **J. Chen, P. Zhao, T. Mei, and H. Liang,(2013)**, “Lane change path planning based on piecewise bezier curve for autonomous vehicle,” in *2013 IEEE International Conference on Vehicular Electronics and Safety (ICVES)*, pp. 17–22, 2013.
- [50] **H. Yoshida, S. Shinohara, and M. Nagai,(2008)**, “Lane change steering manoeuvre using model predictive control theory,” *Vehicle System Dynamics*, vol. 46, no. sup1, pp. 669–681, 2008.
- [51] **P. Dingle and L. Guzzella,(2010)**, “Optimal emergency maneuvers on highways for passenger vehicles with two- and four-wheel active steering,” in *American Control Conference (ACC), 2010*, pp. 5374–5381, June 2010.
- [52] **B. Mashadi and M. Majidi,(2014)**, “Two-phase optimal path planning of autonomous ground vehicles using pseudo-spectral method,” *Proceedings of the Institution of Mechanical Engineers, Part K: Journal of Multi-body Dynamics*, 2014.
- [53] **S.-H. You, J.-O. Hahn, and H. Lee,(2009)**, “New adaptive approaches to realtime estimation of vehicle sideslip angle,” *Control Eng. Practice*, vol. 17, pp. 1367–1379, Dec. 2009.
- [54] **M. Doumiati, A. Victorino, A. Charara, and D. Lechner,(2010)**, “A method to estimate the lateral tire force and the sideslip angle of a vehicle: Experimental validation,” in *Proceedings of the 2010 American Control Conference*, pp. 6936–6942, June 2010.

- [55] **J. J. Oh and S. B. Choi,(2012)**, “Vehicle velocity observer design using 6-d imu and multiple-observer approach,” *IEEE Transactions on Intelligent Transportation Systems*, vol. 13, pp. 1865–1879, Dec 2012.
- [56] **T. Hsiao,(2015)**, “Robust wheel torque control for traction/braking force tracking under combined longitudinal and lateral motion,” *IEEE Transactions on Intelligent Transportation Systems*, vol. 16, pp. 1335–1347, June 2015.
- [57] **H. Hamann, J. K. Hedrick, S. Rhode, and F. Gauterin,(2014)**, “Tire force estimation for a passenger vehicle with the unscented kalman filter,” in *2014 IEEE Intelligent Vehicles Symposium Proceedings*, pp. 814–819, June 2014.
- [58] **A. Rezaeian, R. Zarringhalam, S. Fallah, W. Melek, A. Khajepour, S. K. Chen, N. Moshchuck, and B. Litkouhi,(2015)**, “Novel tire force estimation strategy for real-time implementation on vehicle applications,” *IEEE Transactions on Vehicular Technology*, vol. 64, pp. 2231–2241, June 2015.
- [59] “Users guide for tomlab/snopt,” (2008).
- [60] **J. Funke and J. C. Gerdes,(2015)**, “Simple clothoid lane change trajectories for automated vehicles incorporating friction constraints,” *ASME. J. Dyn. Sys., Meas., Control*, vol. 138, no. 2, pp. 021002–021002–9, 2015.
- [61] **R. Pytlak,(1999)**, *Numerical Methods for Optimal Control Problems with State Constraints*. Lecture Notes in Mathematics, Springer, 1999.
- [62] **J. L. Buchanan and P. R. Turner,(1992)**, *Numerical Methods and Analysis*. McGraw-Hill, Inc., New York, 1992.
- [63] **R. Marino, S. Scalzi, and M. Netto,(2011)**, “Nested {PID} steering control for lane keeping in autonomous vehicles,” *Control Engineering Practice*, vol. 19, no. 12, pp. 1459–1467, 2011.
- [64] **Z. Wu, Y. Liu, and G. Pan,(2009)**, “Smart car control model for brake comfort based on car following,” *IEEE Transactions on Intelligent Transportation Systems*, vol. 10, no. 1, pp. 42–46, 2009.
- [65] **E. Dovgan, T. Tušar, M. Javorski, and B. Filipič,(2012)**, “Discovering comfortable driving strategies using simulation-based multiobjective optimization,” *Informatica*, vol. 36, no. 3, pp. 319–326, 2012.
- [66] **A. K. Nandi, D. Chakraborty, and W. Vaz,(2015)**, “Design of a comfortable optimal driving strategy for electric vehicles using multi-objective optimization,” *Journal of Power Sources*, vol. 283, pp. 1–18, 2015.

- [67] **H. B. Pacejka,(2012)**, *Tire and Vehicle Dynamics*. Oxford: Butterworth-Heinemann, 3rd ed., 2012.
- [68] **D. Swaroop and J. Hedrick,(1996)**, “String stability of interconnected systems,” *Automatic Control, IEEE Transactions on*, vol. 41, pp. 349–357, Mar 1996.
- [69] **J. Eyre, D. Yanakiev, and I. Kanellakopoulos,(1998)**, “A simplified framework for string stability analysis of automated vehicles?,” *Vehicle System Dynamics*, vol. 30, no. 5, pp. 375–405, 1998.
- [70] **V. Milanés and S. E. Shladover,(2014)**, “Modeling cooperative and autonomous adaptive cruise control dynamic responses using experimental data,” *Transportation Research Part C: Emerging Technologies*, vol. 48, no. 0, pp. 285–300, 2014.
- [71] **M. di Bernardo, P. Falcone, A. Salvi, and S. Santini,(2016)**, “Design, analysis, and experimental validation of a distributed protocol for platooning in the presence of time-varying heterogeneous delays,” *IEEE Transactions on Control Systems Technology*, vol. 24, pp. 413–427, March 2016.
- [72] **L. Zhang and G. Orosz,(2016)**, “Motif-based design for connected vehicle systems in presence of heterogeneous connectivity structures and time delays,” *IEEE Transactions on Intelligent Transportation Systems*, vol. 17, pp. 1638–1651, June 2016.

CURRICULUM VITAE

PERSONAL INFORMATION

Surname, Name: MOHAMMED ALI, ARDM HASSEB
Nationality: Iraqi (IRAQ)
Date and Place of Birth: 01/january / 1973 ,kirkuk
Marital Status: Married
Phone: +905342945003, +9647701317846
Email: ardamkahi73@yahoo.com

EDUCATION

Degree	Institution	Year
MS	Cankaya Univ. Electronic and Communication Eng.	2012
B.Sc.	Northern Technical University College of Technical Kirkuk	2003
I.Sc.	Northern Technical University Institutes of Technical Kirkuk	1996
High School	Kirkuk High School	1993

FOREIGN LANGUAGES

Arabic, English, Turkish

PUBLICATIONS

Arđm Haseeb and Klaus Werner Schmidt, Clothoid-based Lane Change Trajectory Computation for Self-Driving Vehicles, Cankaya University Journal of Science and Engineering (accepted), 2017.

HOBBIES

Sport, Reading, Policy